Petrogenesis of Early Miocene plutonism in the Western Cordillera of Colombia, and its relation with the Neogene subduction re-organization

Gladys Eliana Botello Díaz

National University of Colombia

Faculty of Mines, Minerals and Materials Department

Medellín, Colombia

2024

Petrogenesis of Early Miocene plutonism in the Western Cordillera of Colombia, and its relation with the Neogene subduction re-organization

Gladys Eliana Botello Díaz

Thesis submitted as a partial requirement to qualify for the degree of:
Master's in engineering - Mineral Resources

Thesis advisor:

(Ph.D) Astrid Siachoque Velandia

Co-advisor:

(Ph.D) Agustín Cardona Molina

Research area: Magmatism and Tectonic

Research group: "Grupo de Estudios en Geología y Geogísica (EGEO)"

National University of Colombia

Faculty of Mines, Minerals and Materials Department

Medellín, Colombia

2024

Declaration of Original Work

I declare the following:

I have read the Agreement 035 of 2003 the National University Academic Council, "Regulation on intellectual property" and the National Norms related to the respect for copyright. This dissertation represents my original work, except where I have acknowledged the ideas, words, or materials of other authors.

When ideas or words from other authors have been presented in this dissertation, I have properly acknowledged them by applying the appropriate citation and bibliographic reference schemes in the required style.

I have obtained permission from the author or editor to include any copyrighted material (e.g., tables, figures, survey instruments, or substantial portions of text). Lastly, I have submitted this dissertation to the academic integrity tool, as defined by the university.

_____

Gladys Eliana Botello Díaz

Date: 30/01/2024

Acknowledgments

Abstract

Lower Miocene plutons exposed in the Western Cordillera of Colombia record the reinitiation of continental arc magmatism in the Northern Andes after a period of magmatic quiescence between the Late Eocene and Early Miocene. Petrography, U-Pb zircon geochronology, whole-rock geochemistry, mineral chemistry, and zircon Hf isotope data from these plutons are used to reconstruct the Miocene magmatic evolution in the Colombian Andes and understand its relation with the major plate-tectonic reorganization experienced by the NW South American continental margin during the Lower Miocene. We examined a suite of gabbros, granodiorites and tonalites from Danubio, Pance and Tatamá plutons, formed between 21 Ma and 15 Ma. Gabbros present highly positive εHf values (+13.5 and +11.5) with low Th/La and La/Yb ratios, whereas granodiorites and tonalites present lower εHf values (+14.3 to +6.4) and high Th/La, and La/Yb ratios.

The results of this contribution suggest a major asthenospheric source metasomatized by oxidized aqueous fluids derived from the subducted components. The compositional diversification of these magmas was controlled by fractional crystallization and possibly by minor assimilation of continental crust at lower crustal levels of the upper plate and by magma mixing processes. Subsequently, these magmas were emplaced in the Cretaceous to Paleogene volcanic and sedimentary rocks in the uppermost crust.

The renewed magmatic activity recorded by these plutons can be related to the early stages of the Neogene plate reorganization, which was characterized by the normal to steep subduction of the Farallon Plate remnants.

Keywords: Lower Miocene magmatism, Neogene subduction, geochemistry, Zircon Hf isotopy, mineral chemistry.

Resumen

Petrogénesis del plutonismo Mioceno Inferior expuesto en la Cordillera Occidental de Colombia, y su relación con la reorganización de la subducción Neógena

Los plutones del Mioceno inferior expuestos en la Cordillera Occidental de Colombia registran el reinicio del magmatismo del arco continental en los Andes del Norte después de un período de inactividad magmática entre el Eoceno Tardío y el Mioceno Temprano. La petrografía, la geocronología U-Pb en circón, la geoquímica de roca total, la química mineral y los datos de isótopos de Hf en circón de estos plutones se utilizan para reconstruir la evolución magmática del Mioceno en los Andes colombianos y comprender su relación con la reorganización de placas tectónicas experimentada por el margen continental noroeste de América del Sur durante el Mioceno Inferior. Examinamos un conjunto de gabros, granodioritas y tonalitas de los plutones El Danubio, Pance y Tatamá, formados entre 21 Ma y 15 Ma. Los gabros presentan valores de εHf muy positivos (+13,5 y +11,5) con relaciones Th/La y La/Yb bajas, mientras que las granodioritas y tonalitas presentan valores de εHf más bajos (+14,3 a +6,4) y relaciones Th/La y La/Yb altas.

Los resultados de este trabajo sugieren una fuente astenosférica metasomatizada por fluidos acuosos oxidados derivados de los componentes subducidos. La diversificación composicional de estos magmas estuvo controlada por procesos de cristalización fraccionada, así como posiblemente por una asimilación limitada de corteza continental en el nivel inferior de la placa superior y por procesos de mezcla de magma. Posteriormente, estos magmas se emplazaron en rocas volcánicas y sedimentarias del Cretácico al Paleógeno presentes en niveles superiores de la corteza.

La renovada actividad magmática registrada por estos plutones puede estar relacionada con las primeras etapas de la reorganización de la placa Neógena, que se caracterizó por la subducción normal a pronunciada de los remanentes de la Placa Farallón.

Palabras clave: Magmatismo Mioceno Inferior, subducción Neógena, geoquímica, isotopía Lu-Hf en circón, química mineral

Content

Introduction 1

Obectives 3

1.   Theoretical Bases.. 4

    1.1   Magmatic evolution of continental arcs... 4
        1.1.1   Magma formation in subduction zones 5
        1.1.2   Magmatic processes 8
        1.1.3   Subduction configuration and its role in magmatism's geochemistry 9
    1.2   Tools for the analyses of plutonic rocks.. 10

2.   Geological Framework.. 13

    2.1   Cenozoic tectonomagmatic evolution of the Colombian Andes 13
    2.2   Early Miocene magmatism in the Western Cordillera of Colombia.................... 17

3.   Methods 19

    3.1   Fieldwork and petrography 19
    3.2   Zircon U-Pb geochronology 20
    3.3   Whole rock geochemistry 22
    3.4   Trace element and Lu-Hf Isotopes in zircon 23
    3.5   Mineral Chemistry 23
    3.6   Estimation of the crystallization conditions 25

4.   Results 27

    4.1   Field relations and petrography 27
        4.1.1   El Danubio Pluton 28
        4.1.2   Pance Pluton.. 31
        4.1.3   Tatamá Pluton.. 34
    4.2   Zircon U-Pb Geochronology 36
    4.3   Whole-rock geochemistry 39
    4.4   Zircon chemistry and Hf isotopes 45
    4.5   Mineral chemistry 48
        4.5.1   Feldspars 48

List of figures

List of tables

Introduction

The composition of granitoids in continental magmatic arcs is a result of complex interactions between the upper and lower plates during subduction (Ducea et al., 2015; Gill, 2022; Whattam & Stern, 2015). The basic model of a subduction zone argues that the mantle wedge is metasomatized by aqueous fluids or silicate melts released from the subducted oceanic lithosphere to produce arc magmas (e.g., Elliott et al., 1997; Grove et al., 2002; Turner & Lagmuir, 2022). Compositional diversification of arc magmas can occur within the lower crust of upper plate through processes such as magma mixing, assimilation, storage, and homogenization until their final emplacement (MASH zone, Annen et al., 2015, 2006; Hildreth & Moorbath, 1988).

During the Early Miocene, major plate tectonics reorganization characterized the NW South American margin (Gónzález et al., 2023; Montes et al., 2019). The break-up of the Farallon Plate and the associated development of spreading ridges formed the Nazca and Cocos plates (Lonsdale, 2005). These major changes in the plate tectonic circuit lead to fast and more frontal subduction of the oceanic Nazca plate under the South American margin (Lonsdale, 2005; González et al., 2023; Meschede & Barckhausen, 2001; McGirr et al., 2021).

Although some studies have explored potential causal relations between these major kinematic changes and the evolution of arc magmatism in different segments of the Andean orogen (Fernandez-Paz et al., 2019; Schütte et al., 2010), there remains a limited understanding of the magmatic processes that formed the Early Miocene magmatism in the Colombian Andes (Leal-Mejía et al., 2019). Lower Miocene magmatism is recorded by several plutonic bodies exposed along the Western Cordillera of Colombia as well as in detrital zircons from various hinterland basins (Aspden et al., 1987; Nivia, 2001; Echeverri et al., 2015; Leal-Mejia et al., 2019; Zapata et al., 2023) (Figure 1A-B). The Miocene plutons are emplaced in accreted oceanic crust, which constitutes the upper crust segment of the

Western Cordillera of Colombia (Hincapie-Gómez et al., 2019; Kerr et al., 1996; Villagómez & Spiking, 2013). This distinctive crustal architecture offers a unique opportunity to understand the role and character of the lower crust of the upper plate, within an accretionary orogen, in the magmatic evolution during the Miocene period.

This contribution integrates petrography analyses, U-Pb zircon geochronology, whole-rock geochemistry, mineral chemistry, and zircon Hf isotopic data of three Lower Miocene plutons named: Danubio, Pance, and Tatamá. Our results, which are also integrated with published constraints from other contemporaneous plutonic bodies in southwestern Colombia (Leal-Mejía et al., 2019), provide insights into magma sources and the petrogenetic evolution of these plutons. Results indicate a strong mantle-derived input for the source of the parental magmas. The differentiation history likely includes polybaric fractional crystallization, apparently limited low crustal assimilation and magma mixing processes. The renewed magmatic activity recorded by the studied plutons suggest a normal to step subduction of the elder Farallon Plate during the Neogene subduction re-organization in the Colombian Andes, as well as the possible existence of continental crust fragments in the lower crust of the Western Cordillera of Colombia.

Obectives

General objective

To. understand the magmatic and tectonic processes involved in the genesis of the Lower Miocene plutons outcropping between 3°N and 5°N in the Western Cordillera of Colombia and relate them to the Neogene subduction re-organization experienced by the continental margin and the Pacific oceanic plates.

Specific objectives

- Establish the crystallization ages of the El Danubio, Pance, and Tatamá plutons in the Western Cordillera using U-Pb geochronological analyses in zircon in order to constrain the temporal distribution of Early Miocene's magmatic activity.

- Unravel the magma source, melting conditions, and processes of magmatic differentiation, such us fractional crystallization, assimilation and magma mixing in the Early Miocene plutonic record, by means of petrography, whole-rock geochemistry, mineral chemistry, and trace elements and Lu-Hf isotope in zircon, with the purpose of identifying the elements involved in the subduction zone.

- Establish the crystallization history of the El Danubio, Pance, and Tatamá plutons, employing thermobarometry calculations in order to infer the emplacement depth of these plutons.

- Evaluate the relations between the temporal and compositional signatures of the El Danubio, Pance, and Tatamá plutons and other correlatable plutonic bodies within the Western Cordillera and tectonic configuration of the northwestern South American continental margin during the initial stage of Neogene tectonic reorganization.

1. Theoretical Bases

1.1 Magmatic evolution of continental arcs

Subduction zone magmatism results from the dehydration and/or melting of subducted oceanic crust and sediments that transfer fluids to the overlying mantle wedge, where partial melting occurs (Ducea et al., 2015; Gill, 2012; Pearce & Peate, 1995; Whattam & Stern, 2015). The primitive magma generated rises toward the upper lithospheric plate, where it is emplaced and crystallized adding continental crust either as a volcanic cover on the surface or as plutonic bodies at depth (Ducea et al., 2015; Hildreth & Moorbath, 1988; Ruprecht et al., 2012).

Active magmatic arcs are characterized by prominent volcanic edifices with their associated deposits built over several million years (<0.5 or >1Ma; Paterson et al., 2011). However, the volcanic deposits only represent a portion of the magmatic record, and it can be erased from geological history due to high erosion rates (Ducea et al., 2015; Paterson et al., 2011). The ratio of volcanic versus plutonic material volume is highly variable in magmatic arcs, ranging between 1:2 and 1:20 (Paterson et al., 2011), suggesting that the largest volume of magma crystallizes at depth and only a small volume erupts. Therefore, plutonic bodies play a crucial role as tracers of ancient continental arcs in regions where the volcanic record has been lost (Ducea et al., 2015).

Magmatism generated in subduction zones exhibits diagnostic compositional characteristics, including abundant felsic rocks, elevated abundances of large ion lithophile elements (LILEs) relative to the light rare earth elements (LREEs), and depletion of high field strength elements (HFSEs), especially Nb, Ti and Zr (Arculus 1994; Whatman & Stern, 2015). These characteristics are directly linked to the nature of the fluids involved during partial melting (aqueous fluids and/or hydrated melt; Turner & Langmuir, 2022; Zheng, 2019). However, the upper lithospheric plate involved in the subduction configuration tends

to modify the geochemical and isotopic signature of primary magmas derived from the mantle (Annen et al., 2015; Whatman & Stern, 2015).

The upper lithospheric plate in a continental magmatic arc is typically represented by a crust of intermediate to felsic composition that include igneous and metamorphic rocks formed during older tectonic phases (Rudnick & Gao, 2003; Whatman & Stern, 2015). Within this crust the magma undergoes compositional evolution through melting, assimilation, storage, and homogenization processes mainly in the lower crust, as part of what is known as the MASH zone (Annen et al., 2015; Hildreth & Moorbath, 1988). However, in a continental margin constructed by the accretion of oceanic crust (island arc or plateau remnants), the contribution of the crust may be more limited (Whatman & Stern, 2015).

On the other hand, compositional variations in this magmatism may be also influenced by the changes in the subduction configuration, such as the subduction angle, the convergence rate, the thermal structure of the slab, among others (Stern, 2011, 2002, Zheng, 2019). For instance, studies have shown that the depth reached by the subducting slab determines the formation of depleted tholeiites in shallow subduction zones, while deep subduction zones give rise to enriched alkaline basalts (Whatman & Stern, 2015).

In the next chapters, we describe how the compositional characteristics of the magmatism in subduction zones are controlled by the nature of the elements involved during magma melting, the processes of magmatic evolution through the upper plate and by the changes in the subduction configuration.

1.1.1 Magma formation in subduction zones

The classical model proposes that magma formation takes place in the mantle wedge above the subducting slab (Gill, 2012; Stern, 2002), where the mantle is metasomatized by fluids or melts released from the subducted oceanic lithosphere (Elliott et al., 1997; Sisson & Grove,1993; Grove et al., 2002). However, other studies have suggested that arc magmas can be generated by melting the subducted mélange (e.g., Castro et al., 2010; Nielsen & Marschall, 2017; Sun et al., 2021). This mélange is a physical mixing of the oceanic crust, subducted sediments, and mantle peridotite along the slab-mantle interface

that can ascend from the surface of the slab to the hot sub-arc mantle wedge where occur its partial melting (e.g., Castro et al., 2010; Sun et al., 2021). The key distinction between the two models lies in the reversed sequence of mixing and trace-element fractionation, which will produce distinctive isotopic signatures, as highlighted by Nielsen and Marschall (2017).

The subducted oceanic crust is primarily composed of basaltic and gabbroic rocks covered by a thin layer of oceanic sediments (Stern, 2002; White & Klein, 2014). The unaltered basaltic-gabbroic rocks are usually dehydrated and depleted in incompatible elements, particularly in K_2O, TiO_2, FeO, and K (Klein & Langmuir, 1987; Langmuir et al., 1992; White & Klein, 2014). Hydrothermal alteration of these rocks significantly increases the abundances of H_2O, CO_2, and incompatible trace elements, particularly K and U (Stern, 2002). In a subduction zone, most of the water transported to depth is sequestered in hydrated minerals in the metamorphosed and altered crust. However, even the presence of small amounts of serpentinite in the oceanic crust is significant for the water input through the subduction zone (Evans & Frost, 2021; Stern, 2002). Serpentinite carries more water (H2O) than hydrated mafic crust (13% in serpentine versus 1-2% in hydrated mafic crust) and is stable at higher pressures (70 kbar or more, in contrast to 30 kbar in hydrated mafic crust; Stern, 2002; Ulmer & Trommsdorf, 1995). The breakdown of oxidized serpentinites in the subduction zone can generate highly oxidizing fluids, which can also influence the oxygen fugacity of arc magmatism (Brounce et al., 2015; Evans, 2012; Zhang et al., 2021).

The age of the oceanic crust involved in subduction can influence the subduction angle, which in turn affects the input of asthenospheric material into the mantle wedge (Stern, 2002). Subducting old and dense oceanic crust facilitates asthenospheric flow within the mantle wedge due to the steep subduction angle. Conversely, when a young and buoyant oceanic crust is subducted, it results in strong interplate coupling due to the shallow subduction angle, which limits the asthenospheric input (Stern, 2002, 2011).

Subducted sediments are a major reservoir for atypical enrichments in incompatible elements such as K, Sr, Ba, and Th within magmatic rocks (Plank & Langmuir, 1988). The diverse compositions found in subducting sedimentary columns of the oceanic plate offer potentially distinctive contributions to subduction zones, unlike the restricted compositional range observed in the basaltic-gabbroic rocks (Stern, 2002). These sediments can be

primarily carbonate, terrigenous, siliceous, or a combination of these components. The Global Subducted Sediment (GLOSS) is a useful approximation for the average composition of subducted sediments, closely resembling the composition of the upper plate (Plank & Langmuir, 1988; Plank, 2014; Turner & Langmuir, 2022).

In general, subduction zone fluids derived from the oceanic crust and subducted sediments can be present in the form of aqueous solutions (>85% wt. H_2O) or hydrated melts (<35%wt H_2O). The former are produced by metamorphic dehydration reactions at temperatures below the wet solidus of crustal rocks, while the latter result from peritectic reactions at temperatures above the wet solidus of crustal rock (Turner & Langmuir, 2022). Aqueous fluids and hydrated melts can act as metasomatic agents that react with peridotite in the mantle wedge, transferring crustal signatures from the subducting slab to the sub-arc mantle (Turner & Langmuir, 2022; Zheng, 2019).

The enrichment in LILEs (such us Cs, Rb, Ba, and Sr), Pb and U in a continental magmatic arc results from the high mobility of these elements in aqueous fluids, which are derived from dehydration of the subducted sediments and the oceanic crust (Kessel et al., 2005; Zheng, 2019). On the other hand, the depletion in HFSE such as Th, Nb, Ta, Ti, Zr, and Hf but also HREE, is related to the low mobility of these elements in aqueous fluids into subduction zones (Turner & Langmuir, 2022; Zheng, 2019). The high concentration of Th in magmatic arcs are characteristic of the melting of subducted sediments because Th is highly soluble in hydrated melt, despite being relatively insoluble in aqueous solutions (Plank and Langmuir, 1988; Zheng, 2019).

This is well demonstrated by the systematics of thorium-niobium in magmatic arcs, as they have much higher Th/Nb ratios than MORBs, requiring efficient transfer of Th from the subducting plate (Plank & Langmuir, 1998; Zheng, 2019). The low concentrations of Nb, Ta, Ti and Zr, observed in continental magmatic arcs are diagnostic of a subduction setting and are associated with the presence of stable minerals such as rutile and zircon, which usually don't melt in the presence of water, retaining these elements in their mineral structure (Zheng, 2019; Zheng et al., 2011).

1.1.2 Magmatic processes

The conventional model for the genesis of continental arc magmas suggests that felsic to intermediate arc magmas are produced either by fractionation from mafic parental magma or by partial melting of pre-existing crustal rocks, previously extracted from the mantle an emplaced at the base of the crust (Annen et al., 2015; Castro et al., 2021; Moyen et al., 2021). Most of the compositional differentiation of magmas occurs in melt reservoirs and magma chambers in the middle and lower crust (MASH zone), rather than in shallow reservoirs in the upper crust (Annen et al., 2015; Hildreth & Moorbath, 1988). The parent magma within the MASH zone can undergo compositional differentiation through processes such as fractional crystallization, magma mixing, and assimilation of the upper plate (Annen et al., 2015, 2006).

Fractional crystallization differentiation involves separating crystals from the residual melt, which becomes more felsic as crystallization progresses. Efficient extraction of the liquid can generate magmas with considerable composition diversity, ranging from gabbroic to granitic compositions (Annen et al., 2015; Sisson & Grove, 1993; Sisson et al., 2005). Experiments under crustal pressure at 7 kbar indicate that a primitive basaltic magma, equilibrated in the mantle, needs to fractionate over 50% of its crystals before residual melt enters the andesite field (Annen et al., 2015; Sisson & Grove, 1993). If differentiation occurs in the colder upper crust, granites and granodiorites would be limited to no more than 20-30% of the igneous rocks in this crustal section, with the majority comprising mafic accumulations. Therefore, it is presumed that a significant number of felsic magmas originate mainly in the lower and middle crust (Annen et al., 2015, 2006).

The argument that the most significant differentiation of a primitive mafic magma occurs in the lower and middle crust does not preclude the possibility of some additional differentiation at shallower levels during episodes of elevated magma flow rates that allow magma to remain molten in the upper crust. In any shallow magmatic chamber where crystals and liquids can be physically separated, differentiation is possible (Annen et al., 2015).

Simultaneously, repeated mixing of different magma batches is possible within the MASH zone. Magma mixing typically occurs between basaltic melts and fractionation-derived

residual magmas (Annen et al., 2006). The process of magma mixing can be difficult to distinguish in a plutonic system due to re-equilibration between magmas at temperatures above the solidus, resulting in a wide range of melt compositions extracted from the MASH zone (Annen et al., 2015, 2006). An alternative mechanism for magma differentiation involves partial melting and assimilation of the walls or roof of the magma chamber. Isotopic signatures from the upper plate are often detected in igneous rocks of continental arcs, providing evidence of the assimilation process due to the contrast in isotopic composition between the mantle and the evolved crust (Annen et al., 2015; Manduca et al., 1992).

1.1.3 Subduction configuration and its role in magmatism's geochemistry

The compositional characteristics of magmatism generated in subduction zones are significantly influenced by the subduction configuration. The subduction configuration can regulate the volume of the subducted crust and sediments, as well as the influx of the asthenospheric mantle into the subduction zone (Stern, 2020, 2011, 2002).

Subducted sediments and crust removed from the overriding forearc wedge through subduction erosion may remain in the crust by being underplated below the wedge or can be carried into the mantle wedge (Stern, 2011). Once in the mantle wedge, these components can be incorporated into arc magmas through processes of dehydration and/or melting, transferring their geochemical signature to the melt (Annen et al., 2015; Stern, 2011). High rates of subduction erosion in the forearc wedge coincide with relatively high convergence rates (>60 mm/yr) and low rates of sediment supply to the trench (<40 km2/yr) (Stern, 2011).

Shallow subduction angles promote subduction erosion by enhancing coupling between plates, facilitating increased interaction of subducted sediments and crust within the subduction zone (Noda, 2016). In contrast, a steep subduction angle diminishes subduction erosion and favors the influx of asthenospheric material into the mantle wedge, a phenomenon typically reflected in the isotopic signature of the magmas (Stern, 2011, 2002).

The thermal structure within a subduction zone dictates whether the subducted oceanic crust and subducted sediments can yield enough liquid phases to alter the mantle wedge

above depths ranging from the sub-arc (80-160 km) to post-arc (>200 km) regions (Hacker, 2008; Zheng et al., 2019). In colder subduction zones, the subducted oceanic crust undergoes minimal dehydration at forearc depths, allowing it to release ample aqueous solutions at sub-arc depths (Peacock & Wang, 1999; Hacker, 2008, Zheng, 2019). Conversely, in warmer to hotter subduction zones, the subducted oceanic crust may undergo significant dehydration at forearc depths (Zheng, 2019).

Temperature and pressure constitute the primary variables at the interface between the slab and mantle within subduction channels, and understanding their fluctuations is crucial for comprehending mass transfer and geochemical cycling within subduction zones (Manning, 2004; Zheng et al., 2011, Zheng, 2019). However, the thermal structure of subduction zones is temporally variable, and its equilibrium state depends on numerous factors (Kelemen et al., 2003; Peacock, 2003; Zheng, 2019). Thermal structure is correlate with the rate of plate convergence, the age of descending slabs, subduction angle, mantle wedge properties, efficiency of shear heating at the slab-mantle interface, upper plate thickness, and depth of decoupling between the subducting slab and mantle wedge (Zheng, 2019). Therefore, assessing the influence of thermal structure on magmatic genesis is highly complex.

1.2 Tools for the analyses of plutonic rocks

As mentioned above, magma can change its composition as it migrates from the mantle to the crust, mixing with melts from different sources and/or through crystallization and wall - rock reaction processes, producing a wide range of plutonic rocks. To identify the chemical effects of the different processes that formed the plutonic rocks is required the integration of field work and petrography with a full range of geochemical tools that include the major and trace element geochemistry, the chemical mineral of primary mineral phases, and the radiogenic isotopes (Rollinson & Pease, 2021). Radiogenic isotopes are utilized in plutonic rocks for two primary purposes: determining the age of rocks and minerals and identifying geological processes and sources. The former application is known as geochronology, while the latter as isotope geochemistry (Reiners et al., 2018; Rollinson & Pease, 2021).

The study of plutonic rocks starts with fieldwork to characterize the composition, magmatic structures, and post-magmatic alterations of the rocks (Gill, 2022). Field observations may

show the first signs of magmatic processes such as magma mixing and host rock assimilation. Petrographic analysis of the plutonic rocks provides a quantitative measure of rock composition, also allows to identify textural features, and determine paragenetic relationships (Chayes, 1956; Le Maitre et al., 2005). Major and trace element geochemistry is commonly used to characterize rock composition, identify petrological processes, and determine the original tectonic setting of igneous rocks. However, trace elements are more sensitive to geochemical processes than major elements, therefore, they are better at discriminating between petrological processes (Rollinson & Pease, 2021). The mineral chemistry of zircon, plagioclase, clinopyroxene, and amphibole, is used in plutonic rocks to identify the processes of compositional diversification during mineral crystallization and to constrain the intensive crystallization conditions of each rock (Turekian & Holland, 2013). These conditions include temperature, pressure, oxygen fugacity ($logfO_2$), and water content in the melt (H_2Omelt).

Isotopic geochemistry and selected trace element ratios, which are not modified during partial melting and subsequent magma chamber processes, can be used to characterize the chemical composition of a source region, and understand the processes that occur in this region (Rollinson & Pease, 2021). The use of isotopic geochemistry as tracers of petrogenetic processes has provided important geochemical constraints on the nature of the continental crust and the Earth's mantle (Rollison & Pease, 2021). The difference in mass between any pair of radiogenic isotopes is so small that they cannot be fractionated by crystal-liquid processes. Therefore, when partial melting occurs, a magma will maintain the isotopic composition of its source region, and the isotope ratios will remain unchanged during subsequent fractionation processes (Rollinson & Pease, 2021). Specifically, the Hf isotope allows us to recognize magmas generated in primitive conditions, where the mantle is the main contributor to the magmatic melt with values of $^{176}Hf/^{177}Hf$ greater than 0.282785 (Hf>0) (Bouvier et al., 2008), or magmas in which their formation is mainly controlled by the melting of continental crust with values of Hf < 0 (Dickin, 2018; Guo & Korenaga, 2023; Iizuka et al., 2017).

Geochronology in igneous rocks is used for obtaining the age of crystallization of a mineral that usually records the magmatic age of the rock. Geochronology is based on quantifying the isotopic products (parent and daughter isotopes) present within a mineral once it has cooled below the closure temperature of the specific isotopic system (Reiners et al., 2018).

Consequently, for each isotope pair it is possible to determine the time since the mineral cooled below the closure temperature (Reiners et al., 2018). For instance, the closure temperature of the U-Pb system in zircon (900°C - 1100°C, Reiners et al., 2018) is close to the crystallization temperature of the igneous rocks (700°C - 1200°C, Gill , 2022), therefore, the U-Pb geochronology in zircon is widely used for determining the crystallization or cooling age of the plutonic bodies (Miller et al., 2007).

2. Geological Framework

2.1 Cenozoic tectonomagmatic evolution of the Colombian Andes

The Meso-Cenozoic tectonic evolution of the northwestern margin of South America has been controlled by the subduction of several Pacific oceanic plates, and the collision of allochthonous oceanic blocks (Bayona et al., 2020; Bustamante & Bustamante, 2019; Cardona et al., 2018; George et al., 2021; González et al., 2023; León et al., 2018; Montes et al., 2019, 2015; Restrepo et al; 2021; Rodríguez et al., 2019). Specifically, the Western, Central, and Eastern cordilleras of the Colombian Andes (Fig. 1A) are the result of compressional tectonics and magmatism associated to the Cretaceous to Cenozoic subduction of the Caribbean, Farallon, and Nazca oceanic plates (Aspden et al., 1987; Barbosa-Espitia et al., 2019; Cardona et al, 2018; González et al., 2023; Leal-Mejía et al., 2019; Montes et al; 2019), and the accretion of the frontal edge of allochthonous Caribbean oceanic plate block during the late Cretaceous (Cardona et al., 2020; George et al., 2021; Zapata et al., 2019), and its trailing edge represented by the Panamá-Chocó block since the Miocene (León et al., 2018; Montes et al., 2019; 2015).

During the late Cretaceous, the accretion of the Caribbean Plate block to the continental margin incorporated fragments of oceanic plateau and interoceanic arc that currently form the basement of the Western Cordillera (Cardona et al., 2020; George et al., 2021; Geldmacher et al., 2003; Kerr et al., 1997; Villagómez & Spiking, 2013, Zapata et al., 2019). After this collisional event, a Paleocene to early Eocene continental arc magmatism was formed cutting the different Cretaceous and pre-Cretaceous basements of the Central and Western cordilleras (Fig, 1A; Barbosa-Espitia et al., 2019; Bayona et al., 2012; Bustamante et al., 2017; Cardona et al., 2018).

Paleocene to early Eocene arc magmatism preserved in the Central Cordillera (Fig. 1A) has been attributed to the oblique convergence and normal subduction of the Caribbean Plate beneath the South American margin (Bayona et al., 2012; Bustamante et al., 2017; Cardona et al., 2018). This magmatic record is represented by batholith and stock-sized plutonic bodies expose between 3°N and 11°N. The plutonic rocks have U-Pb zircon crystallization ages ranging from 60 Ma to 45 Ma (Bayona et al., 2012; Bustamante et al., 2017; Cardona et al., 2018; Jaramillo et al., 2022) and are characterized by intermediate to felsic compositions with calc-alkaline and adakite-like geochemical signatures, formed by a mantle source modified by assimilation of an older continental crust (Bustamante et al., 2017; Cardona et al., 2018).

Another Paleocene to early Eocene arc related record has been also documented in the southwestern segment of the Western Cordillera (Fig. 1A, 1B). Despite its controversial character, it has been attributed to the slow (~50 mm/yr) and oblique convergence of the Farallon Plate below the accreted allochthonous oceanic block (Barbosa-Espitia et al., 2019). This magmatism is represented by batholith-sized plutons and volcanic-sedimentary rocks exposed around the 2°20'N (Fig. 1B), with U-Pb zircon crystallization and K-Ar groundmass ages ranging from 65 Ma to 32 Ma (Barbosa-Espitia et al., 2019; McCourt et al., 1990). They are characterized by intermediate to felsic compositions with tholeiitic, calc-alkaline and adakite-like geochemical signature, formed from a mantle derived source that assimilated mafic basement crust and continental sediments (Barbosa-Espitia et al., 2019). Other Paleogene plutons have been documented in northwest Colombia, within the Panamá Chocó Block (Fig. 1A), but their petrological features differ with the previously described arcs. Previous studies have proposed that these Paleogene plutons were formed in an intra-oceanic arc environment before the accretion of the Panama-Chocó Block to the continental margin (Barbosa-Espitia et al., 2019; Cardona et al., 2018).

Between 45 Ma and 32 Ma, the magmatic activity ceased until the Early Miocene at ~23 Ma (Bayona et al., 2012; Bustamante et al., 2017; Cardona et al., 2018; Barbosa-Espitia et al., 2019; Jaramillo et al; 2022). This magmatic hiatus has been related to the extremely oblique interaction between the Caribbean, Farallon and the South American plate (Bayona et al., 2012; Montes et al., 2019), or to the overlapping of the Farallon and Caribbean plates that prevent the ascent of magmatic fluids towards the South American plate (González et al., 2023). The N-NE migration of Caribbean plate place the allochthonous Panama-Chocó

block, which was part of the trailing edge of the Caribbean Plate, against the Colombian continental margin (Bourgois et al., 1982; Buchs et al., 2011; León et al., 2018; Wegner et al., 2011). The collision of this block has been proposed to occur from the Eocene-Oligocene (~40-25 Ma; Buchs et al., 2019; Farris et al., 2011; Montes et al., 2019) to the Middle Miocene (~15 -12 Ma; Duque-Caro et al., 1990; León et al., 2018; Montes et al., 2015).

Contemporaneously, at the beginning of the Miocene (~23 Ma), the Farallon Plate broke up forming spreading centers that created the Cocos and Nazca oceanic plates (Lonsdale, 2005; Barckhausen et al., 2008). The formation of new oceanic crust also triggered a fast (~120 mm/yr) and orthogonal subduction of the Nazca Plate under the western margin of the South American Plate (González et al., 2023; Montes et al., 2019; Somoza & Ghidella, 2005).

This renewed subduction configuration of the Nazca Plate, reestablished the magmatic activity in the Colombian Andes, as evidenced by the presence of Lower Miocene (~23-15 Ma) plutons exposed along the Western Cordillera (Fig. 1A-B; Aspden et al., 1987; Barbosa-Espitia, 2020; González, 2002; Leal-Mejía et al., 2019). After the Early Miocene, the Nazca Plate underwent major changes in its subduction angle (Wagner et al., 2017), triggering the migration of magmatism towards the Cauca Valley during the Late Miocene (~9-5 Ma; Bissig et al., 2017; Borrero et al., 2016; Jaramillo et al., 2019) and to the Central Cordillera from the Pliocene to the present (~3-0 Ma; Borrero et al., 2009, 2008; Toro Toro et al., 2010; Wagner et al., 2017).

The modern tectonic configuration of the Colombian Andes is characterized by two subduction segments to the north and south of the Caldas tear (5.5° N), which were related to flat and normal subduction of Nazca Plate, respectively (Wagner et al., 2017). The recent magmatism (<2 Ma) along the Central Cordillera is due to the slow (~53 mm/yr) and oblique convergence with normal subduction of the Nazca Plate (Fig. 1A; Mora-Páez et al., 2019; Somoza et al., 2005; Trenkamp et al., 2002). The Caribbean Plate is converging slowly (~19 mm/yr) and obliquely with shallow subduction on the N and NW edges of Colombia, without record active magmatism. The Panamá-Chocó Block (Fig. 1A), which was previously accreted to the Colombian continental margin, separates these two oceanic plates that interact in the Northern Andes (Mora-Páez et al., 2019).
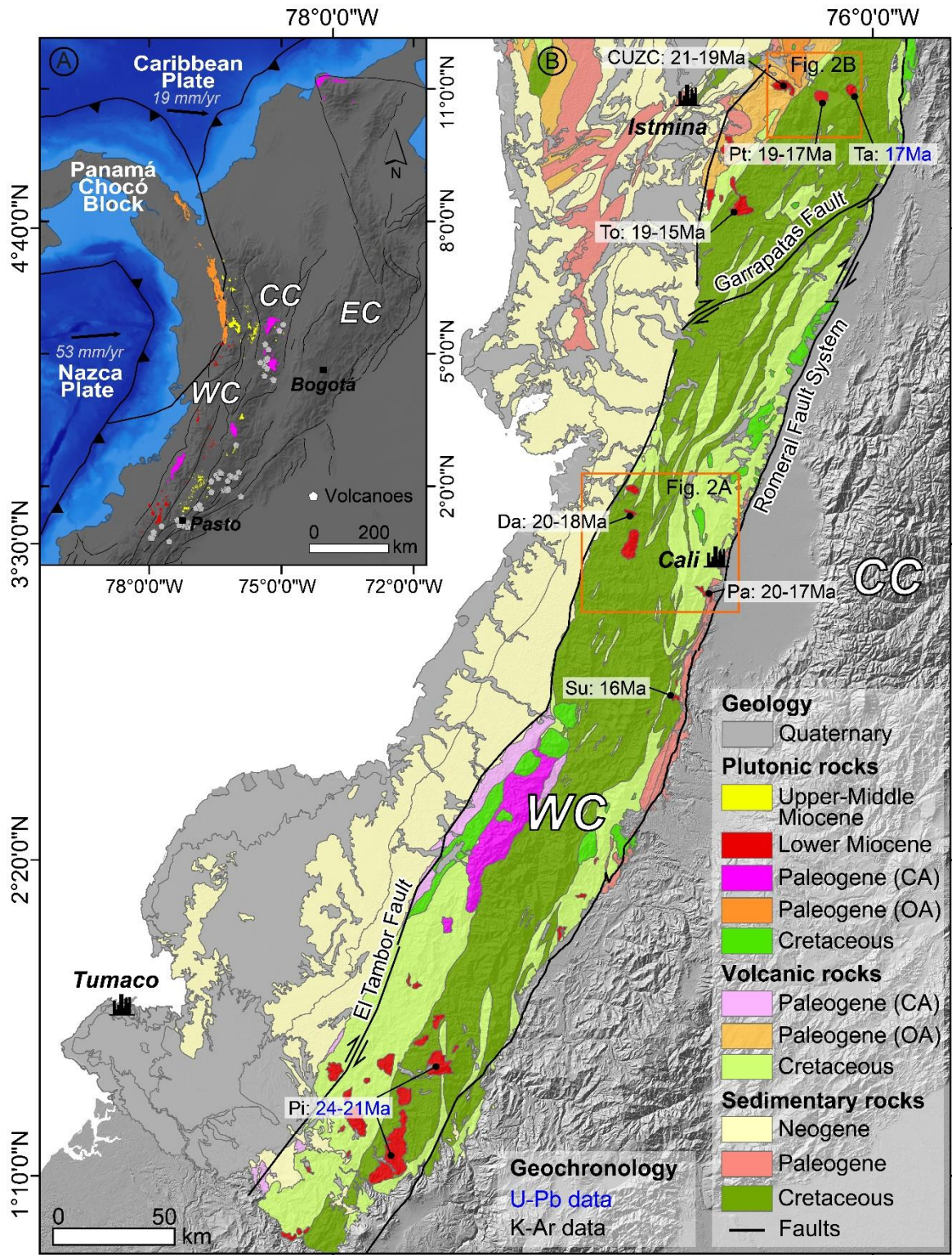
Figure 1. A. Regional map of the Colombian Andes showing the current tectonic configuration and the distribution of the magmatism from Paleocene to Upper Miocene Abbreviations: EC: Eastern Cordillera; WC: Western Cordillera; CC:

Central Cordillera. **B.** Geological map of the Western Cordillera (WC) showing the distribution of the plutonic bodies of the Miocene: Pi: Piedrancha; Su: Suárez; Pa: Pance; Da: El Danubio; To: Torrá; Ta: Tatamá; Pt: Pital; CUZC: Condoto Zoned Ultramafic Complex; CA: Continental Arc, OA: Oceanic Arc. Published ages of Barbosa-Espitia, 2020: Echeverri et al., (2015), Leal-Mejía et al., (2019) and González (2002).

2.2 Early Miocene magmatism in the Western Cordillera of Colombia

Early Miocene magmatism is represented by several plutonic bodies that are discontinuously exposed along the Western Cordillera of Colombia (Fig.1B). From south (~1°N) to north (~5°N), they are known as the Piedrancha, Suárez, El Danubio, Pance, Torrrá, Pital and Tatamá plutons. Each of these magmatic bodies has a stock size, typically not exceeding 100 km2, except for the Piedrancha Pluton, characterized by a batholith size (González, 2002; Leal-Mejía et al., 2019; Zapata, 2001).

These plutonic bodies are mainly characterized by granodiorites and tonalites, with subordinate diorites and gabbros (Nivia, 2001; Zapata, 2001). U-Pb in zircons and K-Ar in hornblende and biotite suggest that these rocks have crystallization ages ranging from ~24 Ma to 15 Ma (Fig. 1B; Echeverri et al., 2015; Leal-Mejía et al., 2019; González, 2002). Available geochemistry data show predominant metaluminous, calc-alkaline to high-K calc-alkaline compositions for these rocks (González, 2002; Leal-Mejía et al., 2019; Zapata, 2001). Moreover, several Hf, Sr, Nd and Pb isotopic analysis for some of these plutons indicate that they were generated from a mantle source that interacts with older continental crustal (Barbosa-Espitia, 2020; Leal-Mejía et al., 2019).

The Lower Miocene plutons intruded the Cretaceous volcano-sedimentary basement of the Western Cordillera, and occasionally Paleogene sedimentary cover (Fig. 2A, 2B; Barbosa-Espitia, 2020; González, 2002; Nivia, 2001; Zapata, 2001). The intrusive relationships with the Cretaceous volcano-sedimentary basement are mark by the presence of amphibolitized basalt xenoliths derived from Cretaceous volcanic rocks (Nivia, 2001), and by the presence of hornblende-hornfels to albite-epidote facies within the host sedimentary rocks, forming an aureole of approximately 1 km of wide (González, 2002). Intrusive relationships with

Paleogene clastic rocks are reflected by the formation of anthracite-type coals (Nivia, 2001), and the presence of quartz veins and dykes cross-cutting these rocks (Rodríguez & Zapata, 2006).

Some of the Lower Miocene plutons present hydrothermal alteration. The Piedrancha Pluton has been associated with hydrothermal vein-type deposits containing minerals such as pyrite, hydrothermal quartz, arsenopyrite, sphalerite, chalcopyrite, and galena (Molano & Shimazaki, 2003; Bustos Rodriguez et al., 2011, 2008). Additionally, evidence of disseminated sulfides has been documented in the Pance and El Danubio plutons (Aspen et al., 1984; Verdugo & Aspdend, 1984).
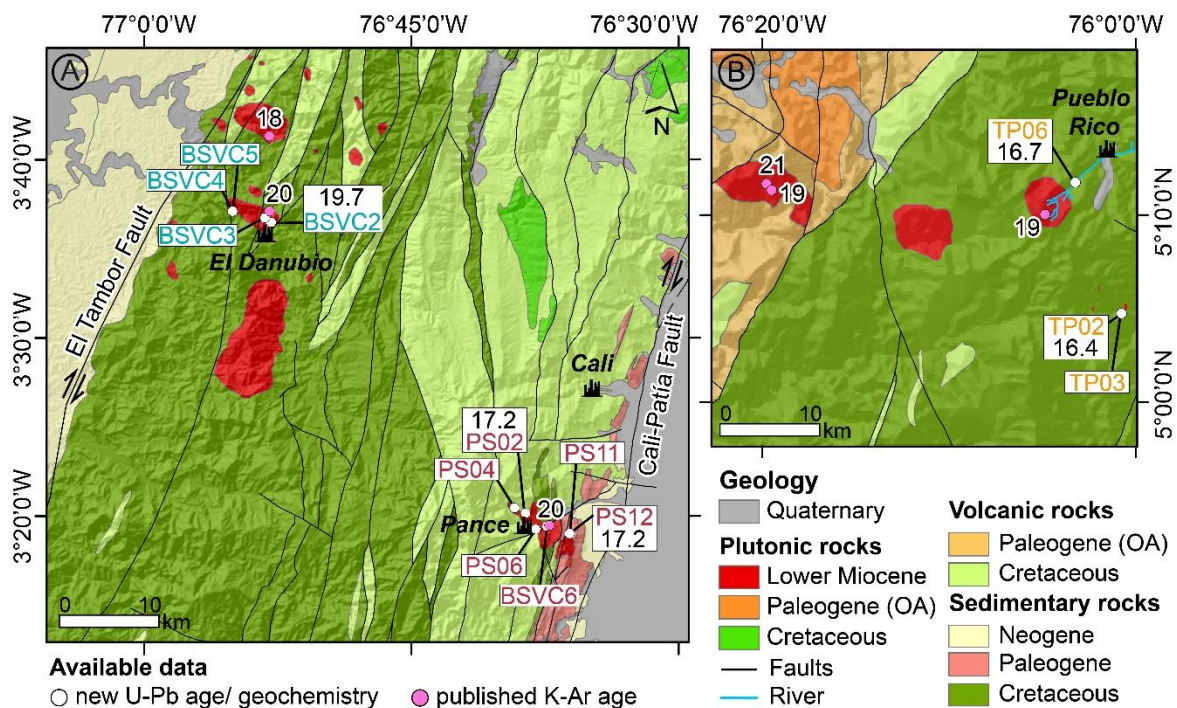
Figure 2. Local geological maps showing the sample location for El Danubio Pluton (blue labels), Pance Pluton (red labels) and Tatamá Pluton (orange labels).

3.Methods

In this study, we followed a multi-technique approach to understand the petrogenesis of the Lower Miocene El Danubio, Pance, and Tatamá plutons, which are exposed between approximately 3°N and 5°N in the Western Cordillera of Colombia (Fig. 1B, 2A, B). This approach integrates fieldwork and petrography to characterize the composition and textures of these plutonic bodies, as well as zircon U-Pb geochronological analyses to determine the crystallization ages of each pluton. Furthermore, whole-rock geochemistry, mineral chemistry, trace elements and Lu-Hf isotope in zircon are employed to unravel the magma source, magma melting conditions, magmatic evolution processes, and crystallization conditions of the plutons.

3.1 Fieldwork and petrography

Fieldwork was carried out at two distinct localities on the Western Cordillera: one in the state of Valle del Cauca, along the western and eastern flank of the Western Cordillera where the El Danubio and Pance plutons are exposed (Fig. 2A). The other is in the state of Risaralda, further to the northeast, approximately 200 km to the north of the El Danubio Pluton, where the Tatama pluton and associated apophysis are exposed (Fig. 2B). The main characteristics of the Tatamá Pluton are described from the blocks exposed at the head of the Negro River (Fig. 2B), which flows toward the municipality of Pueblo Rico. Other Lower Miocene Plutons exist between both locations; however, it was not possible to sample the due to access limitations.

Seventeen field stations were described in order to review the composition, magmatic structures, and post-magmatic alterations of the studied plutons. A total of fourteen samples were collected for analytical techniques as presented in Supplementary Table 1. The collected samples were examined under a petrographic polarized microscope (Olympus CX31-P). Petrographic descriptions include quantitative mineral compositions, textural

features, and paragenetic relationships. Quantitative modal compositions were determined by point-counting of >200 crystals (Chayes, 1976) and are presented in Table 2. The rocks were classified according to Le Maitre et al. (2002) as seen in Fig. 4. Textural and paragenetic relationships were described to establish the crystallization order, petrographic facies, and to identify possible deformation mechanisms during the magmatic and post magmatic history (e.g., Passchier & Trouw, 2005; Vernon, 2018).

Table 1. List of analytical techniques employed for each sample.

Sample	Latitude	Longitude	Pluton	Type of rock	Thin section	Zircon U-Pb	Whole rock geochemistry	Trace element and Lu-Hf Isotopes in zircon	Mineral chemistry
BSVC2	3.6081	-76.8811	El Danubio	Granodiorite	x	x	x	x	x
BSVC3	3.6124	-76.8870		Tonalite	x		x		
BSVC5	3.6184	-76.9172		Tonalite	x		x		
BSVC4	3.6184	-76.9172		Quartz monzodiorite	x				
PS02	3.3360	-76.6433	Pance	Granodiorite	x	x	x	x	
PS06	3.3210	-76.6337		Granodiorite	x		x		
PS04	3.3411	-76.6533		Tonalite	x		x		
PS12	3.3171	-76.6019		Diorite	x	x	x	x	
BSVC6	3.3253	-76.6220		Gabbro	x		x		x
PS11	3.3181	-76.6019		Hornblendite	x				
TP02	5.0852	-76.0118	Tatamá	Granodiorite	x	x	x	x	x
TP03	5.0852	-76.0118		Granodiorite	x				
TP06	5.2055	-76.0640		Granodiorite	x				
TP06-2	5.2055	-76.0640		Granodiorite	x	x	x	x	x

3.2 Zircon U-Pb geochronology

Five representative samples from the El Danubio (1), Pance (2) and Tatamá (2) plutons were selected for zircon U-Pb geochronological analyses. Preparation of the samples was performed at the Zirchron Llc Company, by rough-crushing, pulverizing, and sieving in 330 µm mesh. Zircon concentrates were passed through a water table (Wilfley®) and followed by magnetic separation using a Frantz ® isodynamic magnetic separator. After that, methylene iodide (3.3 g/cm3) was used to concentrate zircon crystals (3.9 to 4.8 g/cm3) from the non-magnetic fraction. Between 45 to 20 zircons were subsequently randomly handpicked under the microscope and mounted in an epoxy puck along with the standard zircons Plešovice and 91,500 (Chang et al., 2006; Sláma et al., 2008), and finally polished to expose crystal faces.

Cathodoluminescence (CL) images were obtained for each mount using the JEOL JSM 5600 scanning electron microscope (SEM) at the Washington State University laboratory in Pullman, USA. CL images were used to identify the internal textures of each grain including zonation patterns, bright patterns, and inclusions (e.g Corfu et al., 2003).

The zircon grains were analyzed by laser ablation inductively coupled plasma mass spectrometry (LA-ICP-MS) using a G2 193 nm excimer laser ablation system coupled with a Thermo-Finnigan™ Element 2 single-collector ICP-MS, in the GeoAnalytical laboratory of the Washington State University in Pullman, USA. Measurements were made on the rims of the grains to avoid zircon xenocrysts. Analytical conditions included a spot size of 30 μm, a repetition rate of 10 Hz, and an energy of ~5.5 J/cm2. Each analysis consisted of 25s gas blank and 25s ablation wait before moving to the next grain. During the laboratory session, the standard zircons were analyzed two to three times every 5–10 unknown zircon analyses. The analytical procedures followed those described by Chang et al. (2006), except for the use of the 193 nm laser system instead of the 213 nm laser.

Plešovice zircon standard (337 Ma; Sláma et al., 2008) was used to calibrate the 206Pb/238U and 207Pb/235U ages, and 91,500 zircon standards (~1063 Ma; Schoene et al., 2006) was used to calibrate the 207Pb/206Pb age, owing to much higher count rates for 207Pb (~2-4 times higher than Plešovice). Common Pb correction was performed using the 207Pb method by Williams (1998).

A cutoff of 1000 Ma was applied to select the best age for each zircon (Gehrels et al., 2008). The 206Pb/207Pb zircon age is reported for all grains older than 1000Ma, while the 206Pb/238U age is reported for younger grains due to the precision of each age, which is given by the relative concentrations of the 238U and 235U parent isotopes in the earth and the half-life of each radiogenic system (Gehrels et al., 2012, 2008). The errors reported for all ages are 2 sigma. Detailed zircon U-Pb data are presented in the Supplementary Table 2.

For all the samples, a discordance filter of 20% (discordance = 100 - 100x [206Pb/238U age / 206Pb/207Pb age]) was applied for zircon's older ages (>500 Ma; Gehrels et al., 2012). This filter was not applied for younger ages (<500 Ma) due to difficulty of determining

reliable 206Pb/207Pb ages (Gehrels et al., 2012). Additionally, an analytical error filter was applied for all ages, eliminating those that exceeded 3% error (Schaltegger et al., 2015). The filtered data are presented in the Tera-Wasserburg U-Pb concordia plot, which shows 207Pb/206Pb against 238U/206Pb (Vermeesch, 2018). Crystallization ages were calculated using the Weighted Average Age method (Vermeesch, 2018). These statistical analyses were performed using IsoplotR (Vermeesch, 2018).

3.3 Whole rock geochemistry

A total of eleven samples from the El Danubio (4), Pance (5), and Tatamá (2) plutons were analyzed in order to determine the whole rock geochemistry. Whole-rock major oxides (SiO_2, Al_2O_3, Fe_2O_3, $Ti2O$, MgO, MnO, CaO, Na_2O, K_2O, and P_2O_5) and trace elements concentrations (REEs, Ba, Nb, Ni, Sr, among others) were obtained by Inductively Coupled Plasma-Atomic Emission Spectroscopy (ICP-AES) and Inductively Coupled Plasma-Mass Spectrometry (ICP-MS), respectively, at the ALS Geochemistry Laboratories in Lima, Perú.

Each sample was crushed using a jaw crusher and pulverized using a tungsten carbide ring mill. The sample powder (0.1 g) was placed into a graphite crucible and mixed with 1.5 g of lithium borate flux (LiBO2). The crucibles were heated in a furnace to 1025°C for 15 minutes.

The resulting melt is then cooled and dissolved in an acid mixture containing nitric, hydrochloric and hydrofluoric acids. Calibration standards and reagent blanks were added to the sequence of analyzed samples. Detection limits for the major elements vary between 0.01% and 0.002%, whereas for trace elements vary around ± 0.1 ppm - 0.01 ppm.

Loss on Ignition was calculated by Thermal Decomposition Furnace. A sample (1g) is weighed, placed in an oven at 1000°C for one hour, cooled and then weighed again. The percent loss on ignition is calculated from the difference in weight before and after ignition. The results of geochemical analyses were processed and plotted using the software GCDKit 5.0 (Janousek et al., 2022). All data are available in Supplementary Table 3.

3.4 Trace element and Lu-Hf Isotopes in zircon

Samples with U-Pb data from the El Danubio (BSVC2) and Pance (PS02 and PS12) plutons were selected for the trace element and Lu-Hf isotopic analyses in zircon. The trace element analysis (Ti, Y, Nb, Hf, Pb, Th, U, P, Ca) including rare earth elements (REE, from La to Lu) were performed using LA-ICP-MS at the Washington State University laboratory. Between 10 and 15 zircons were analyzed for each sample. The analysis consisted of two cleaning pulses, 10s washout, 18s gas blank, 40s ablation, and 15s wait before moving the stage. International reference glass NIST610 and NIST612 and zircon reference 91500 were verified every 15 analyses to correct for instrument drift. Data correction and reduction were performed using the Iolite software. Trace elements and REE zircon data are presented in Supplementary Table 4.

In addition, Lu-Hf isotopic compositions of each sample were analyzed using Analyte G2 193 nm excimer laser ablation system coupled with a ThermoFinnigan™ Neptune multi-collector mass spectrometer (MC-ICPMS) at the Washington State University laboratory. Operating parameters included a laser fluence of ~5.5 J/cm2 and a repetition rate of 10 Hz, following the method discussed by Fisher et al. (2014), except that U-Pb dates were not simultaneously determined. The output from the ablation cell was mixed with N2 gas and delivered directly to the Neptune MC-ICPMS. The Plešovice zircon standard ($^{176}Hf/^{177}Hf$ = 0.282482 ± 13) was regularly analyzed between samples to correct the measured $^{176}Hf/^{177}Hf$ of unknowns and reduce inter-laboratory bias. Correction for the isobaric interference of ^{176}Yb and ^{176}Lu on ^{176}Hf was assessed using quality control zircons (Fisher et al., 2014). Internal 2-sigma precision was ~1.1 εHf. Analyses with less than 25 ratios or internal 2-sigma uncertainty over 2 εHf units were discarded.

Present-day εHf values were calculated using the CHUR parameters reported by Bouvier et al. (2008), where $^{176}Hf/^{177}Hf$ DM(0) = 0.282785±11 (2σm) and $^{176}Lu/^{177}Hf$ DM(0) = 0.0336 ± 1. Trace element and Lu-Hf isotopic data are reported in Supplementary Table 4.

3.5 Mineral Chemistry

Four representative samples from the three studied plutons were selected for mineral chemistry analysis of feldspars, pyroxene, amphibole, and biotite group-minerals. Two analytical seasons were performed using an Electron Probe Micro-Analyzer (EPMA) in the

Department of Lunar and Planetary Sciences at the University of Arizona (USA) and in the GeoAnalitica laboratory of the Institute of Geosciences at the University of Sao Paulo (Brazil).

Analysis of the El Danubio and Pance samples at the University of Arizona were done over polished 30-μm thick sections using a CAMECA SX-50 equipment with quantitative spot analysis done by wavelength-dispersive spectrometry (WDS). The analytical conditions for the WDS analysis were done with a beam current of 20.0 nA, an accelerating voltage of 15 kV, and a total counting time of 20 s, equally distributed for peak and background. The standards used for element calibrations included "albite-Cr" for Na, "ol-fo92" for Mg and Si, "anor-hk" for Al and Ca, "kspar-OR1" for K, "rutile1" for Ti, "fayalite" for Fe, "rhod-791" for Mn and "chrom-s" for Cr. Microprobe analytical error ranges ± 0.01–0.21 wt% (1σ) with detection limits varying ± 0.01–0.11 wt%.

Within the University of Sao Paulo, the analysis of the Tatamá samples was using a field emission JEOL JXA-FE-8530 microprobe. WDS analyses were performed with 15 kV, 20 nA, and 5 μm for the column acceleration voltage and beam current and beam diameter, respectively. Total counting times, equally distributed for peak and background readings, varied from 10 s to 40 s; matrix effects were corrected with the PROZA PRZ/Armstrong software. The standards used for element calibrations included natural and synthetic standards from both the Smithsonian and the GellerTM collections: hornblende (Si and 222 Al in amphiboles), diopside (Mg), fayalite (Fe and Mn), anorthoclase (Al), wollastonite (Ca), orthoclase (K), rutile (Ti), albite (Na), zircon (Zr), willemite (Zn), benitoite (Ba), glass_synthetic (Ni) sodalite (Cl), and fluorapatite (F). Microprobe analytical error ranges ± 0.1-1.4 wt% (1σ) with detection limits varying ± 0.01–0.10 wt%.

Mineral formulae for the analyzed feldspars, pyroxene, amphibole, and biotite were determined based on 8, 6, 24 and 11 (or 22) atoms per formula unit (apfu), respectively. The structural formulae of feldspars and pyroxene minerals were calculated following Deer et al. (2013). Amphibole-group classification was computed according to the nomenclature scheme of Hawthorne et al. (2012) by using the Excel spreadsheet of Locock (2014). Normalization of the Fe^{3+}/Fe^{2+} ratios in the amphiboles were determined assuming 13 cations exclusive of Ca, Na, and K. The structural formula of biotite crystals was calculated assuming all Fe as $Fe^{2+.}$ Additionally, we include the stereochemistry estimation of the Li

contents [$Li_2O=2.1/(0.356+MgO)-0.088$] according to Tischendorf et al. (2004). The complete compositions and structural formulae for all rock-forming minerals are given in Supplementary Tables 5.

3.6 Estimation of the crystallization conditions

Whole-rock compositions of the studied rocks and mineral chemistry data of zircon, plagioclase, clinopyroxene, and amphibole were used to constrain the intensive crystallization conditions for each pluton, including depth of magmatic diversification (crustal thickness), temperature (T), pressure (P), oxygen fugacity ($logfO_2$) and water content in the melt (H2Omelt).

Apatite saturation temperatures were determined using the SiO_2 and P_2O_5 values from the whole-rock compositions according to the method proposed by Harrison and Watson (1984). This thermometry model was applied to the metaluminous samples with SiO2 ranging from 45 to 75 %wt and H_2O content varying between 0 and 10 %wt. The temperatures were calculated using the GCDKit software.

Zircon crystallization temperatures were estimated in the samples BSVC2 (El Danubio Pluton), PS02 and PS12 (Pance Pluton), following the method of Ferry & Watson (2007). This approach takes into account the Ti content in zircon, along with the activation energy values for TiO_2 ($aTiO_2$) and SiO_2 ($aSiO_2$ in each rock. Due to the absence of rutile in all samples, $aTiO_2$ is less than unity (Hayden & Watson, 2007). A value of a $TiO_2=0.6$ was assumed for the thermometry calculations, given the mineral paragenesis of titanite + hornblende ± biotite in the samples (e.g. Ferry & Watson, 2007; Hayden & Watson, 2007). For the samples BSVC2 and PS02 that present quartz, aSiO2 is equal to the unity, whereas in sample PS12 with lacked quartz, $aSiO_2$ is reduced (~0.9, Schiller and Finger, 2019). It's important to note that temperatures may be overestimated by up to 45°C due to the absence of rutile, introducing an error in zircon crystallization temperatures by the same margin.

The chemistry of clinopyroxene and the whole-rock compositions of the sample BSVC6 were used to determine the magma temperatures and pressures conditions applying the thermobarometer method of Putirka et al. (1996), which relies on clinopyroxene-liquid

equilibria. Putirka's equations exhibit a standard error of ± 246.2°C for temperature and ± 1.4 kbar for pressure. Additionally, we employed the clinopyroxene-only thermometer developed by Wang et al. (2021a), assuming a water content of 2 wt.% for the calculations. This thermometer has an error of ± 36.6°C.

The compositions of plagioclase and amphiboles were utilized to determine the crystallization temperatures and pressures conditions of the studied rocks. Thermometric calibrations include the Holland & Blundy (1994) Expression B (error of ± 40); Putirka (2016) Equations 5 and 6 (errors of ±30 and ±30, respectively); the Liao et al. (2021) model (error of ±35); and the Ridolfi (2021) model (error of ±22 °C). Selected barometric models follow the proposed calibrations of Molina et al. (2015), Mutch et al. (2016), and Ridolfi (2021), which have errors of ±1.5, ±0.5 and ±0.5 kbar, respectively.

Additionally, physicochemical magma conditions were calculated according to the amphibole and zircon compositions of the studied plutons. Oxygen fugacity (fO_2) and water contents (H_2Omelt) were calculated using the amphibole chemistry and the equations of Ridolfi (2021). These equations have a standard error of ±0.3 log units in fO_2 and ±14% in H_2Omelt. Zircon oxygen fugacity was established using the equations of Loucks et al. (2020). This method relies on the ratios of Ce, U, and Ti in zircon and does not require information about the crystallization temperature, pressure, or parental melt composition. The reported results have an associated error of ±0.6 log units in fO_2.

Finally, moho depths or crustal thickness was estimated using the empirical equations calibrated by Profeta et al. (2015) and Tang et al. (2020). Profeta et al. (2015)'s equation is based on the $(La/Yb)_N$ ratio measured in whole-rock geochemistry. Samples with compositions of 55-68%wt SiO2, 0-4%wt MgO and 0.05-0.2% Rb/Sr are excluded to avoid mantle-generated mafic rocks, high-silica felsic rocks, and rocks formed from melting of metasedimentary rocks (Profeta et al., 2015). Results obtained by this method have an error of ± 6-7 km. Tang et al (2020) also proposed that within zircons the Eu anomaly (Eu/Eu* ratio) is sensitive to fractionation under varying pressure. However, crustal thickness values derived from zircon geochemistry are approximations and need to be interpreted carefully because Eu/Eu* ratios may be affected by variations in the redox state of the melts, magmatic evolution processes and the crystallization sequence in granitic rocks (Yakymchuk et al., 2023). Results obtained by this method have an error of ± 8-12 km.

4. Results

4.1 Field relations and petrography

Field observations and petrographic descriptions from the collected samples show significant compositional and textural heterogeneities within the studied plutonic bodies. The modal proportions of the plutonic rocks can be found in the Supplementary Table 1. We grouped eight petrographic facies: (i) quartz monzodiorite and (ii) tonalite-granodiorite facies in the El Danubio Pluton; (iii) clinopyroxene hornblendite, (iv) clinopyroxene hornblende gabbro, (v) foliated hornblende gabbro, and (vi) tonalite-granodiorite facies within the Pance Pluton; (vii) foliated granodiorite facies in Tatama Pluton and (viii) seriate granodiorite facies related in the small apophyses that are also associated to the Tatama Pluton (Fig. 3). The sequence of crystallization defined according the mineral textural features in each facies is presented in the Figure 6.
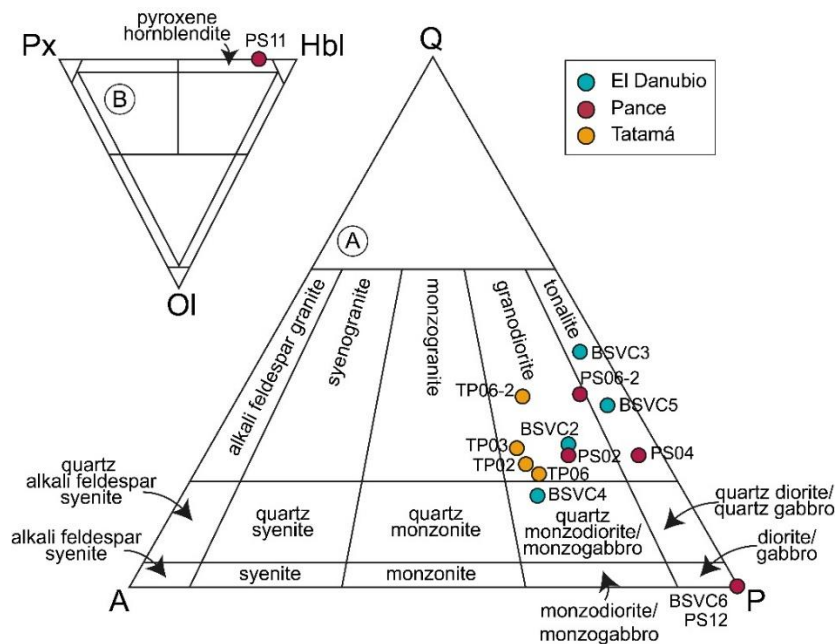
Figure 3. Modal classification diagrams from samples of the El Danubio, Pance and Tatamá plutons. A. Quartz - Alkali feldspar - Plagioclase (QAP) plot (Streckeisen, 1976), B.

Plagioclase-Pyroxene-Hornblende diagram with the IUGS nomenclature for ultramafic rock (Le Maitre, 2002).

4.1.1 El Danubio Pluton

This plutonic body is exposed near to the town of El Danubio showing an elongated NW direction and an exposure area of ~9 km2 (Fig. 2A). It is relatively homogeneous and composed mainly of massive phaneritic rocks of tonalitic and granodioritic composition, with rounded mesocratic enclaves of small-sized and irregular shapes (10 to 20 cm) of dioritic to quartz monzodioritic compositions (Fig. 4A-B). Some of these enclaves show euhedral plagioclase crystals of coarse-grained size (Fig 3A). The tonalites are also characterized by hydrothermal alteration represented by pervasive pyrite and chalcopyrite along with quartz-filled veins.
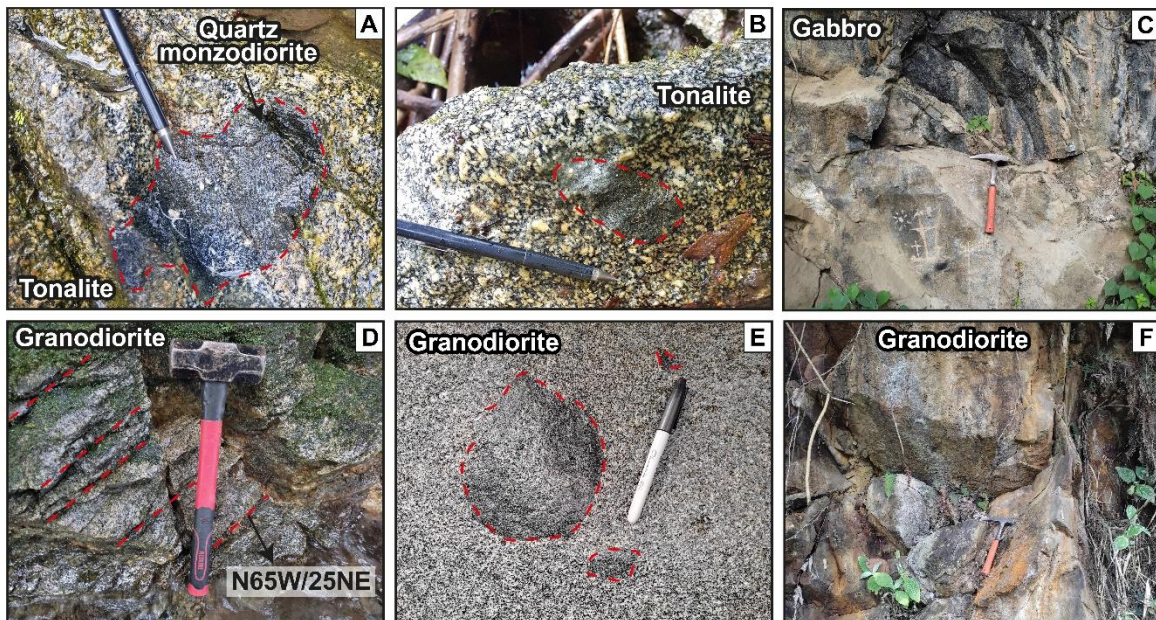
Figure 4. Macroscopic features of the El Danubio (A-B), Pance (C-D), and Tatamá (D-E) plutons. **A-B.** tonalite showing mesocratic enclaves (e.g. quartz monzodiorite). **C.** massive structure in gabbro. **D.** granodiorite with a magmatic foliation. **E.** granodioritic blocks related to Tatamá Pluton, which are exposed at the head of the Negro River. Granodiorite presents mafic mineral clusters. **F.** Hydrothermal alteration is evident in the variation of colors observed in the rock outcrops of the Tatamá apophysis.

(i) Tonalite-granodiorite facies: this is characterized by rocks with medium to fine-grained inequigranular textures (Fig. 5A-C). The rocks are mainly composed of plagioclase and hornblende occurring as euhedral to subhedral crystals, which crystallized during the early stage (Fig. 6). Plagioclase usually shows oscillatory zoning and growth twins, with some crystals displaying corroded cores with deformation lamellae stepped and ending in tips. Hornblende occurs as prismatic crystals with green pleochroism and simple twinning (Figs. 5A). Some crystals show corroded limits and corona-reaction textures, being mantled by biotite laths (Fig. 5A). Biotite is a common late-crystallized mafic phase (Fig. 6) showing subhedral forms, brown pleochroism, and pebbly extinction (Fig. 5A-C). Quartz and K-feldspar occur as interstitial minerals formed during the late-stage of crystallization (Fig. 6). Quartz crystals often show evidence of sub-magmatic and sub-solidus deformation textures with chessboard extinction (Fig. 5B) and grain boundary migration and bulging recrystallization, respectively. K-feldspar crystals are commonly characterized by cross-hatched twinning and exsolution textures (Fig. 5B). Local occurrences of quartz–K-feldspar granophyric intergrowths are also observed. Accessory minerals include apatite, titanite, zircon, and opaque phases, which are present as early inclusions in plagioclase, hornblende, and biotite crystals. Secondary minerals include sericite, epidote, muscovite, and carbonates (Fig. 5C), commonly replace primary minerals, and indicate the percolations of post-magmatic hydrothermal fluids.

(ii) Quartz monzodiorite facies: this facies displays a medium to fine-grained inequigranular texture. The analyzed rock is composed of primary hornblende, plagioclase, K- feldspar, biotite, and quartz, with accessory minerals such as, allanite, zircon, apatite, and opaque phases. Secondary minerals found include epidote, zoisite-clinozoisite, muscovite and sericite. Hornblende forms individual or grouped euhedral to anhedral crystals (Fig. 5D-F), some of them are altered to epidote and clinozoisite. Plagioclase crystals are euhedral to subhedral and show corroded cores, growth and deformation twins, and stepped lamellae textures. Biotite is a late-magmatic phase that commonly occurs replacing the hornblende crystals. K-feldspar appears as subhedral to anhedral crystals, exhibiting granophyric textures with quartz intergrowths (Fig. 5F). Quartz crystals commonly show undulatory extinction and occur interstitial to hornblende and feldspars. Allanite and opaques appear as inclusions in hornblende whereas zircon and apatite are commonly included in plagioclase and hornblende.
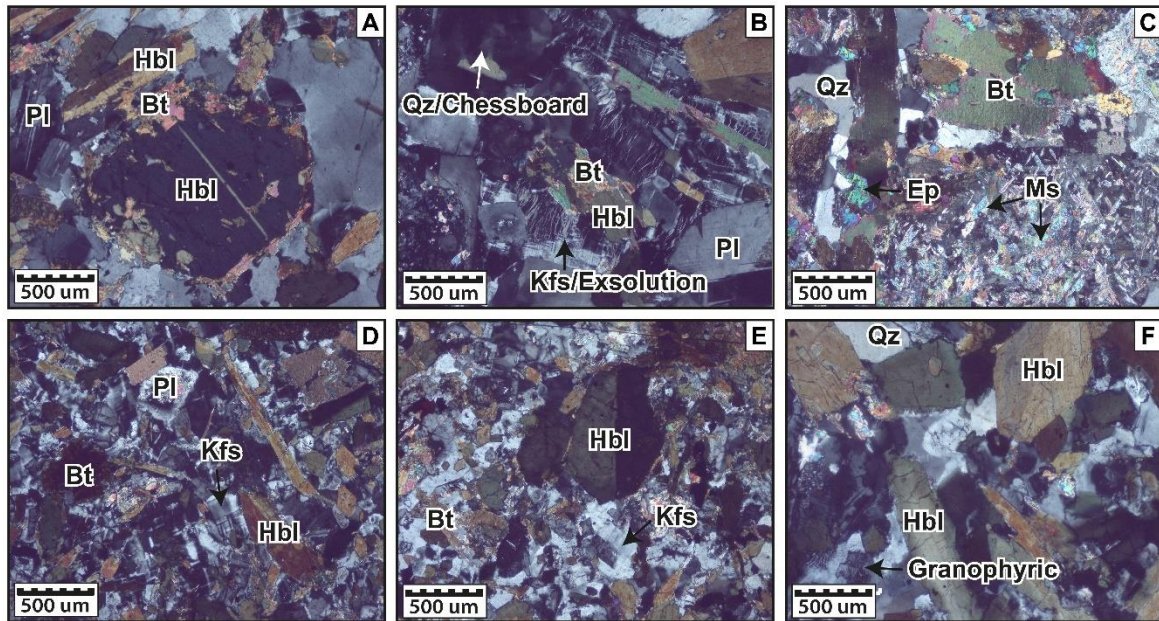
Figure 5. Microscopic features of the El Danubio Pluton. **A-C.** tonalite-granodiorite facies (samples BSVC2, BSVC3, BSVC5). **D-F**. quartz monzodiorite facies (sample BSVC4).
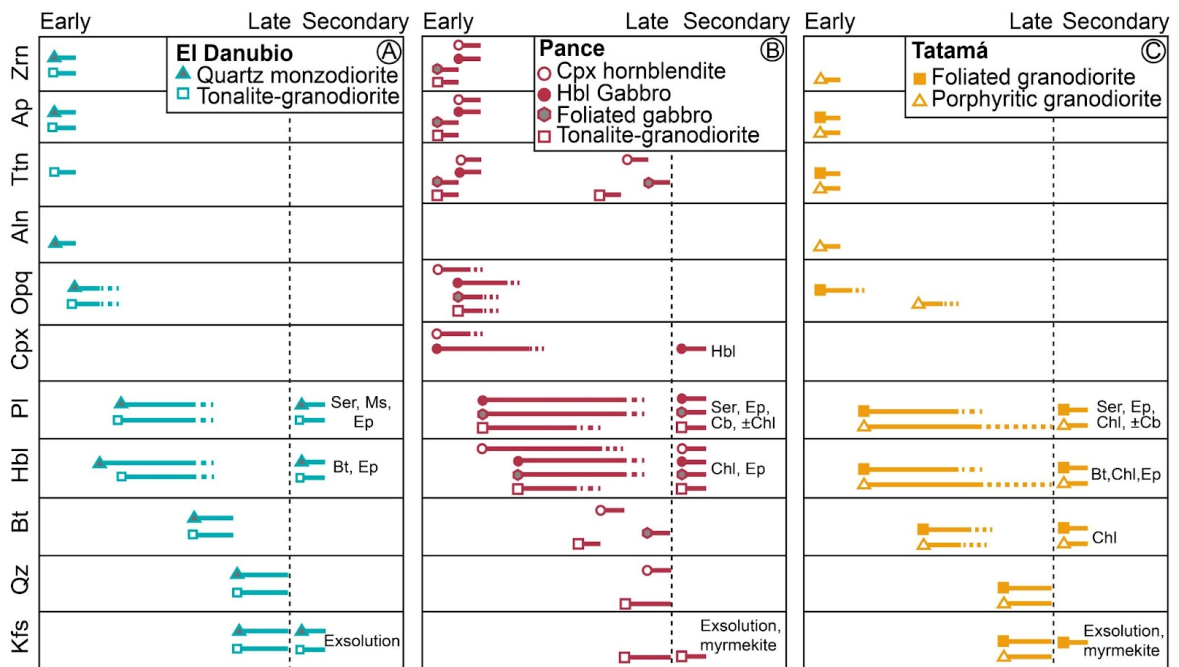
Figure 6. Crystallization sequence for the studied rocks from the El Danubio (**A**), Pance (**B**) and Tatamá (**C**) plutons showing the mineral occurrence at early-, late-, and post-magmatic stages. The mineral abbreviations are taken from Whitney & Evans (2010).

4.1.2 Pance Pluton

Pance Pluton shows an irregular shape, covering an area of approximately 13 km². It crops out near the town of Pance and intrudes Cretaceous volcanic-sedimentary sequences and Paleogene sedimentary rocks (Fig. 2A). The intrusive body is characterized by massive to foliated phaneritic textures (Fig. 3C-D) and includes clinopyroxene hornblendite, clinopyroxene hornblende gabbro, foliated hornblende gabbro, tonalite and granodiorite. The foliated hornblende gabbro and granodiorite show magmatic foliation oriented N27°E/80°NW and N65°W/25°NE. Mesocratic enclaves with small-sized (<3 cm) and irregular shapes are also common. Additionally, brittle deformation is evident within the plutonic rocks, exhibiting several fractures-oriented NE-SW and NW-SE.

(iii) Clinopyroxene hornblendite facies: this shows a coarse- to fine-grained inequigranular texture and it is mainly composed of primary hornblende and clinopyroxene. Clinopyroxene forms subhedral to anhedral crystals of light green color to colorless and is usually found within the cores of the hornblende suggesting an early stage of crystallization (Fig. 6, 7A). Hornblende is the main mafic phase occurring as dark brown-green colored subhedral to anhedral crystals (Fig. 7B), commonly altered to chlorite and epidote along their rims (Fig. 7C). Accessory minerals include opaque minerals, zircon, titanite, biotite and quartz. Zircon and opaque minerals are usually found as inclusions in hornblende (Fig. 7A). Titanite exhibits two distinct textural varieties, the first is characterized by early formed rhombohedral euhedral to subhedral crystals, while the other consists of anhedral crystals associated with aggregates of hornblende, opaques, and biotite, which suggests a late-magmatic stage of crystallization (Fig. 7B). Biotite and quartz are late-magmatic phases occurring as interstitial crystals between hornblende (Fig. 7B). Some of the quartz crystals show undulatory extinction and microfractures.
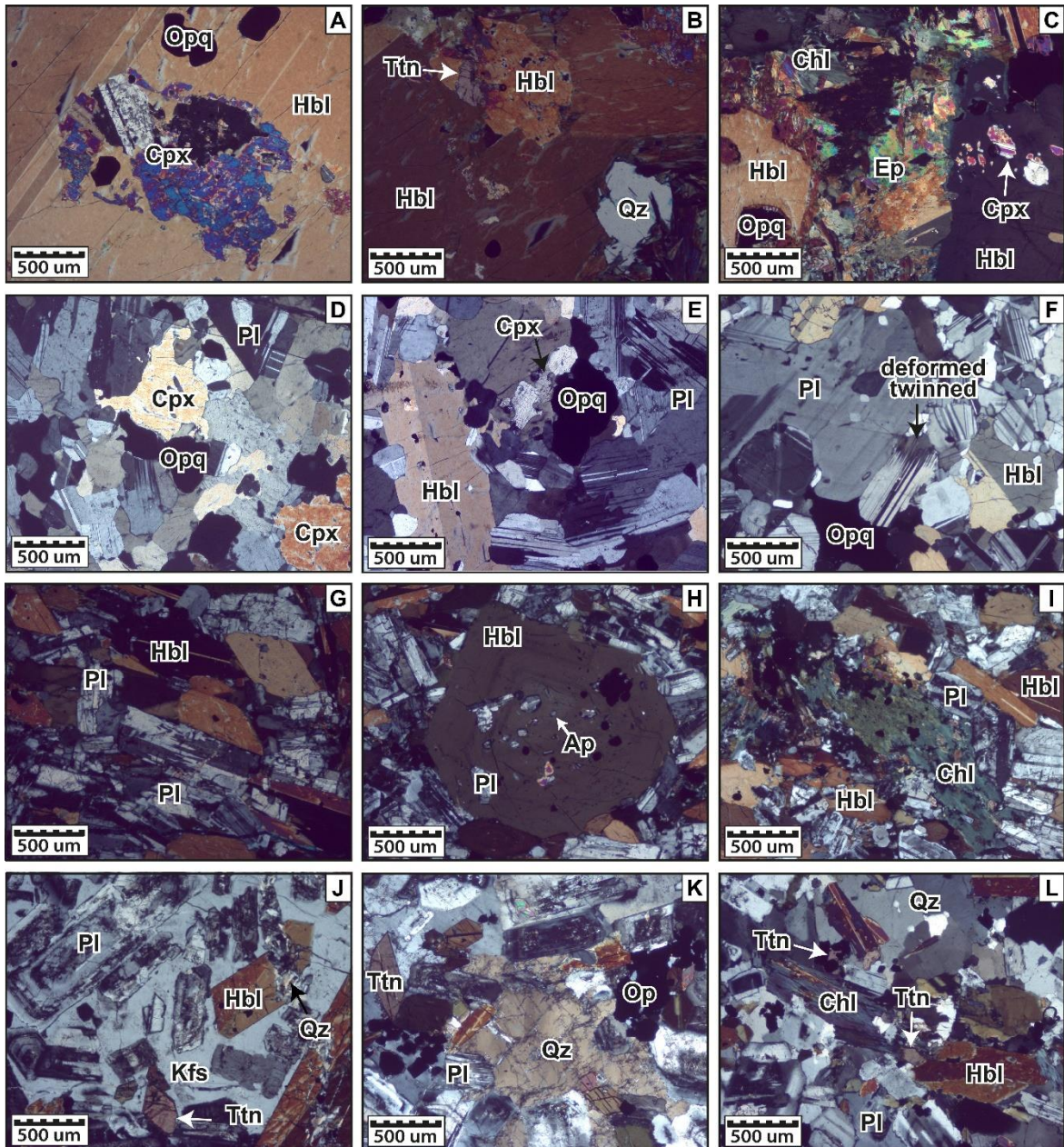
Figure 7. Microscopic features of the Pance Pluton. **A-C**. pyroxene hornblendite facies (sample PS11). D-F. gabbro facies (sample BSVC6). **G-I.** foliated hornblende gabbro facies (sample PS12). **J-L.** tonalite-granodiorite facies (samples PS04, PS02, PS06-2).

(iv) Clinopyroxene hornblende gabbro facies: this consists of rocks with medium to fine-grained inequigranular textures. The rocks are composed of plagioclase, clinopyroxene, hornblende, opaque minerals, and accessories such as apatite, zircon and titanite.

Clinopyroxene forms subhedral to anhedral crystals (Fig. 7D) with a colorless or pale green pleochroism, and occasionally with simple twinning. Some of them appear either as relics within hornblende crystals or altering the hornblende edges (Fig. 7E), indicating crystallization during the early stage. Hornblende occurs as subhedral crystals with a pale green pleochroism, tabular habits and poikilitic textures including tiny inclusions of plagioclase and apatite. Plagioclase crystals exhibit euhedral forms, oscillatory zoning, and multiple twinning; sometimes, they display deformation twinning with lamellae ending in tip and stepped microstructures (Fig. 7F). Secondary phases include sericite, epidote, and zoisite-clinozoisite. These rocks also show textural evidence of solid-state deformation with microfractures and post-magmatic veins-filled with quartz and K-feldspar.

(v) Foliated hornblende gabbro facies: this is restricted to the easternmost segment of the Pance Pluton. They are characterized by medium to fine-grained inequigranular foliated textures defined by the hornblende and plagioclase crystals (Fig. 7G). Hornblende forms tabular euhedral to subhedral brown to green colored crystals, often showing zoning and poikilitic textures with inclusions of plagioclase, opaques, and apatite (Fig. 7H). Also, some of them are strongly altered by biotite and chlorite (Fig. 7I). Plagioclase usually appears as subhedral crystals with oscillatory zoning, simple or multiple twinned, while some crystals show deformation twins with lamellae ending in tips and steps and are altered by carbonate and sericite. Biotite is late-magmatic and occurs as a replacement of hornblende. The accessories include, opaque minerals, titanite, apatite, zircon, and biotite. Like in the clinopyroxene hornblendite facies, titanite occurs in two textural types: early and late-crystallized generations, while apatite, zircon and opaques are present as inclusions in plagioclase and hornblende.

(vi) Tonalite and granodiorite facies: this is the most prominent facies in Pance Pluton. The rocks are characterized by coarse to fine-grained inequigranular textures and are mainly composed of plagioclase and hornblende. Plagioclase shows euhedral to subhedral and tabular crystals with oscillatory zoning and multiple twinned textures (Figure 7J). Some crystals show corroded cores and deformation twins. Hornblende occurs as euhedral to anhedral greenish crystals with strong pleochroism. They show simple and multiple twins and are commonly altered by chlorite and epidote. Locally, these rocks exhibit a magmatic foliation, which is mainly defined by the hornblende crystals. Plagioclase and hornblende were crystallized during the early stage. Biotite, K-feldspar, and quartz commonly occur as

interstitial crystals between plagioclase and hornblende (Fig.6, 7J-K), suggesting crystallization during the late-magmatic stage. Biotite crystallized as individual subhedral to anhedral brownish crystals. K-feldspar forms anhedral crystals exhibiting poikilitic textures with inclusions of plagioclase, hornblende, titanite, and biotite (Fig. 7J). Myrmekite intergrowths are also observed within the K-feldspar and plagioclase crystals. Quartz crystals are characterized by sub-magmatic and solid-state deformation microstructures showing undulose extinction, bulging and grain boundary migration, and microfractures. Primary accessories are opaque minerals, titanite, zircon and apatite. Titanite crystallized either as an individual early (Fig. 7J-K) or as late-magmatic crystals (Fig. 7L). In contrast, apatite, zircon, and opaque minerals are usually included in plagioclase, hornblende, and biotite. Secondary minerals are sericite, chlorite, epidote, and carbonate. Most of these crystals display microfractures, and irregular forms. Hydrothermal veins-filled of quartz are also observed (Fig. 7J).

4.1.3 Tatamá Pluton

Tatamá Pluton is a sub-circular intrusive body covering an area of ~16 km^2 and situated along the central axis of the Western Cordillera (Fig. 2B). Three small apophysis, (< 1 km^2) are exposed in the southern segment of the pluton (Fig. 2B). The Tatamá pluton and the associated apophyses intrude into Cretaceous volcano-sedimentary rocks and are mainly composed of granodiorites with inequigranular foliated phaneritic and porphyritic textures. The granodiorites included melanocratic diorite rounded enclaves of small size (1 to 10 cm), and mafic mineral clusters with irregular forms and sizes of up to 15 cm (Fig. 4E). In addition, the plutonic rocks from the apophyses also display hydrothermal alteration (Fig. 4F) characterized by vein-filled and disseminated pyrite and chalcopyrite mineralization.

(vii) Foliated granodiorite facies: this is the predominant petrographic facies exposed at the head of the Negro River (Fig. 2B), which flows through the main body of Tatamá Pluton. The rocks are characterized by medium to fine-grained inequigranular textures and are mainly composed of primary plagioclase, hornblende, and biotite (Fig. 6). Plagioclase forms subhedral tabular crystals with oscillatory zoning patterns, and often showing multiple twinned and deformation twins (Fig. 8A-C). Hornblende occurs as individual euhedral to subhedral crystals or as irregular crystals forming clusters with titanite and opaque minerals (Fig. 8B). Some of these crystals show slight alteration by chlorite and epidote. Of note,

magmatic foliations characteristic of these rocks are defined by elongated hornblende and plagioclase crystals, which were formed during the early stage of crystallization (Fig. 8A). Biotite forms subhedral crystals with green to brownish pleochroism and several inclusions of opaque minerals. Quartz and K-feldspar occur as interstitial minerals formed during the late stage of crystallization (Fig. 6). Quartz crystals usually show evidence of sub-solidus deformation with undulose extinction, bulging and grain boundary migration recrystallization textures. K-feldspar crystallized as subhedral to anhedral crystals with simple twinned and myrmekite exsolutions (Fig. 8C). Early crystallized accessories include apatite, zircon, titanite, and opaque minerals, while secondary minerals correspond with sericite, epidote, and chlorite.
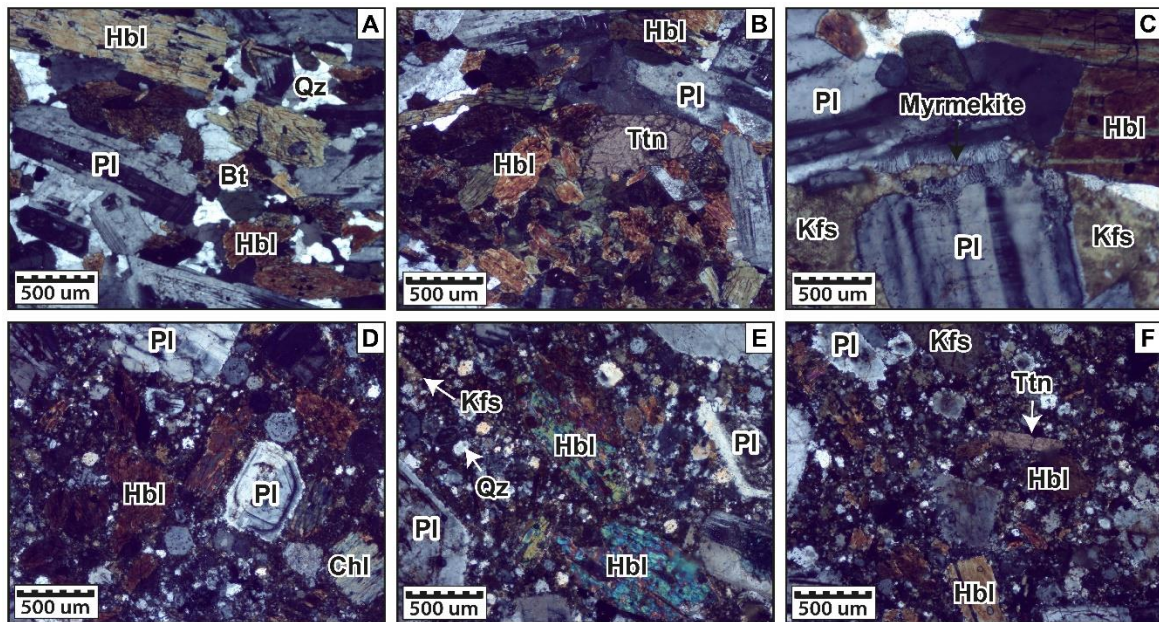
Figure 8. Microscopic features of the Tatamá Pluton. **A-C.** foliated granodiorite facies (samples TP06, TP06-2). **D-F.** porphyritic granodiorite facies (samples TP02, TP03).

(viii) Porphyritic granodiorite facies: this facies is characteristic of the apophysis. The rocks present porphyritic texture with primary coarse to fine-grained phenocrysts of plagioclase and hornblende embedded into a quartz-feldspathic microcrystalline matrix (Figs. 6 and 8D-F). Plagioclase crystallized as euhedral to subhedral tabular crystals with oscillatory zoning (Fig. 8D). Some crystals show simple and multiple twinned, and deformation tip lamellae. Hornblende exhibits subhedral and tabular forms, dark brown to

greenish pleochroism and altered limits by the replacement of secondary chlorite and epidote. Quartz, K-feldspar, and biotite occur as interstitial minerals between the primary phases and usually show irregular forms with corroded limits (Fig. 8D-F). Apatite, zircon, allanite, and opaque minerals are present as early magmatic inclusions in plagioclase and hornblende.

4.2 Zircon U-Pb Geochronology

U-Pb zircon crystallization ages were determined for five samples, including a granodiorite (BSVC2) from the El Danubio Pluton; a foliated hornblende gabbro (PS12) and a granodiorite (PS02) from the Pance Pluton; and two granodiorites from the Tatamá Pluton (TP06-2) and the associated apophyses (TP02). U-Pb analytical data is presented in the Supplementary Table 2.

Zircons from the El Danubio and Pance plutons exhibit mainly euhedral shapes, with sizes ranging between 30 and 500 μm, and length:width (l:w) ratios between 2:1 and 6:1 (Table. 2). Cathodoluminescence (CL) images show weak and well-developed oscillatory zoning (Fig. 9A-C), which is common feature of magmatic zircons (Corfu et al., 2003). The weakly oscillatory zoning is a distinctive feature found in zircons from the Pance Pluton (samples PS12 and PS02), and it is associated with minor differences in composition from the core to the rims of the crystals (Olierook et al., 2020).

In addition, some zircons show xenocrystic cores (Fig. 9A) and dark patterns in the El Danubio Pluton (sample BSVC2), and bright patterns in the Pance Pluton (sample PS02). Dark patterns (Fig. 9A) indicate zircons with high trace element contents, especially high U and Th concentrations, that limit CL response (Corfu et al., 2003; Olierook et al., 2020). In contrast, bright patterns (Fig. 9C) correspond to the relatively low content of trace elements (Corfu et al., 2003).

Eighteen zircons from El Danubio Pluton (sample BSVC2) show ages from 19.2 to 21.6 Ma and Th/U ratios between 0.1 and 0.8 in crystals with oscillatory zoning pattern, indicating a clear magmatic origin as autocrysts and/or antecrysts. The oldest magmatic ages could be associated with antecrystic zircons as also suggested by the presence of corroded edges (Fig. 9A). Xenocrystal or inherited zircons have U-Pb age of 151 Ma and 1517 Ma and Th/U

ratio of 0.33 and 0.49, respectively. A crystallization weight average age of 19.7 ± 0.1 Ma was calculated using six zircons, corresponding to the youngest magmatic zircon group (Fig. 10B).
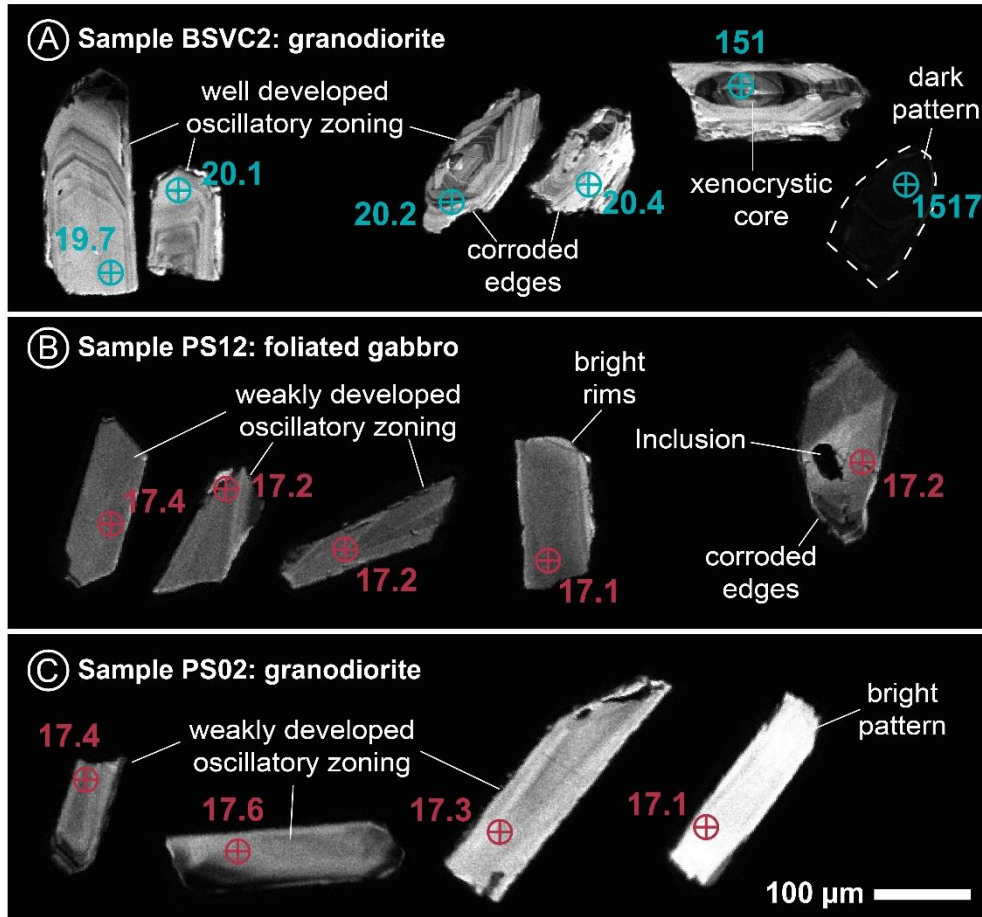
Figure 9. Cathodoluminescence images (CL) of representative zircons from the El Danubio Pluton (sample BSVC2) and the Pance Pluton (sample PS12 and PS02). All images have the same scale. Circles represent the laser ablation spot, and the adjacent numbers show the zircon age in Ma.
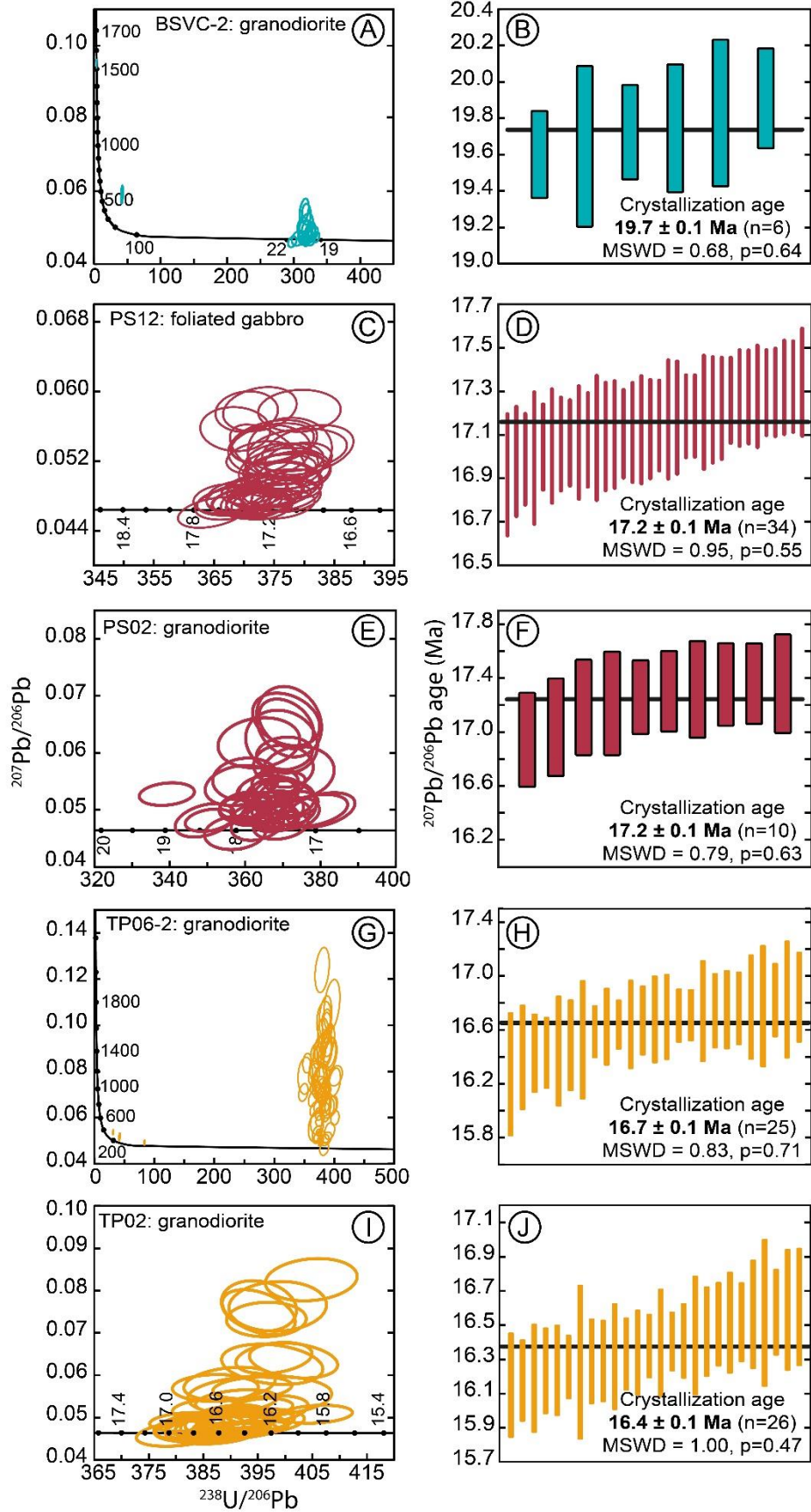
Figure 10. Tera-Wasserburg U-Pb concordia and Weighted Average Age plot for the samples from the El Danubio Pluton (**A-B**), the Pance Pluton (**C-F**), and the Tatamá Pluton (**G-J**).

Forty-five zircons from the foliated hornblende gabbro (sample PS12) sample of the Pance Pluton show magmatic ages ranging from 16.9 to 17.9 Ma and Th/U ratios between 0.4 and 2.1. A crystallization age of 17.2 ± 0.1 Ma was obtained with thirty-four crystals (Fig. 10D). A granodiorite for this pluton (sample PS02) also presents ages between 16.7 and 18.9 Ma with Th/U ratios between 0.1 and 0.9. A similar crystallization age of 17.2 ± 0.1 Ma was obtained with ten crystals (Fig. 10F). The decrease in the zircon Th/U values between the gabbro and the granodiorite (Table 1) is characteristic of compositional differentiation of the magmatic rocks (Claiborne et al., 2010; Kirkland et al., 2015).

Sixty-five zircons from granodiorite (sample TP06-2) representative of the Tatamá Pluton yield ages between 16.0 and 18.5 Ma, with Th/U ratios from 0.2 to 1.3, which are typical magmatic crystallization ages. Three zircons yield older ages of f 77, 152 and 204 Ma with Th/U ratios of 0.9, 0.3 and 0.2, respectively, that can be related to inherited or xenocrystal zircons. This sample yields a crystallization age of 16.7 ± 0.1 Ma using twenty-five zircons (Fig. 10H). Thirty-seven zircons from granodiorite sample (sample TP02) related to the apophysis of the Tatamá Pluton show ages between 15.8 and 16.9 Ma and Th/U ratios varying from 0.3 to 0.8, which are related to the magmatic crystallization history. Twenty-six crystals yield a crystallization age of 16.4 ± 0.1 Ma (Fig. 10J).

4.3 Whole-rock geochemistry

Geochemical results are presented in the Supplementary Table 3. Major elements were recalculated on an anhydrous basis using the loss-on-ignition values.

The studied plutons are characterized by SiO_2 values range from 39.5 to 68.6 wt.% and total alkalis ($Na_2O + K_2O$) between 1.6 to 8.2 wt.% (Fig. 11A). All rocks are metaluminous in compositions (Fig. 11B), with A/CNK [Al_2O_3/($CaO+Na_2O+K_2O$) wt.%] values ranging between 0.7 and 0.9, and A/NK [Al_2O_3/(Na_2O+K_2O] values between 1.5 and 8.5. Geochemical signatures vary between the calc-alkaline and high-K calc-alkaline series, although one sample from the Tatamá plutons also plot in the shoshonite series (Fig. 11C).
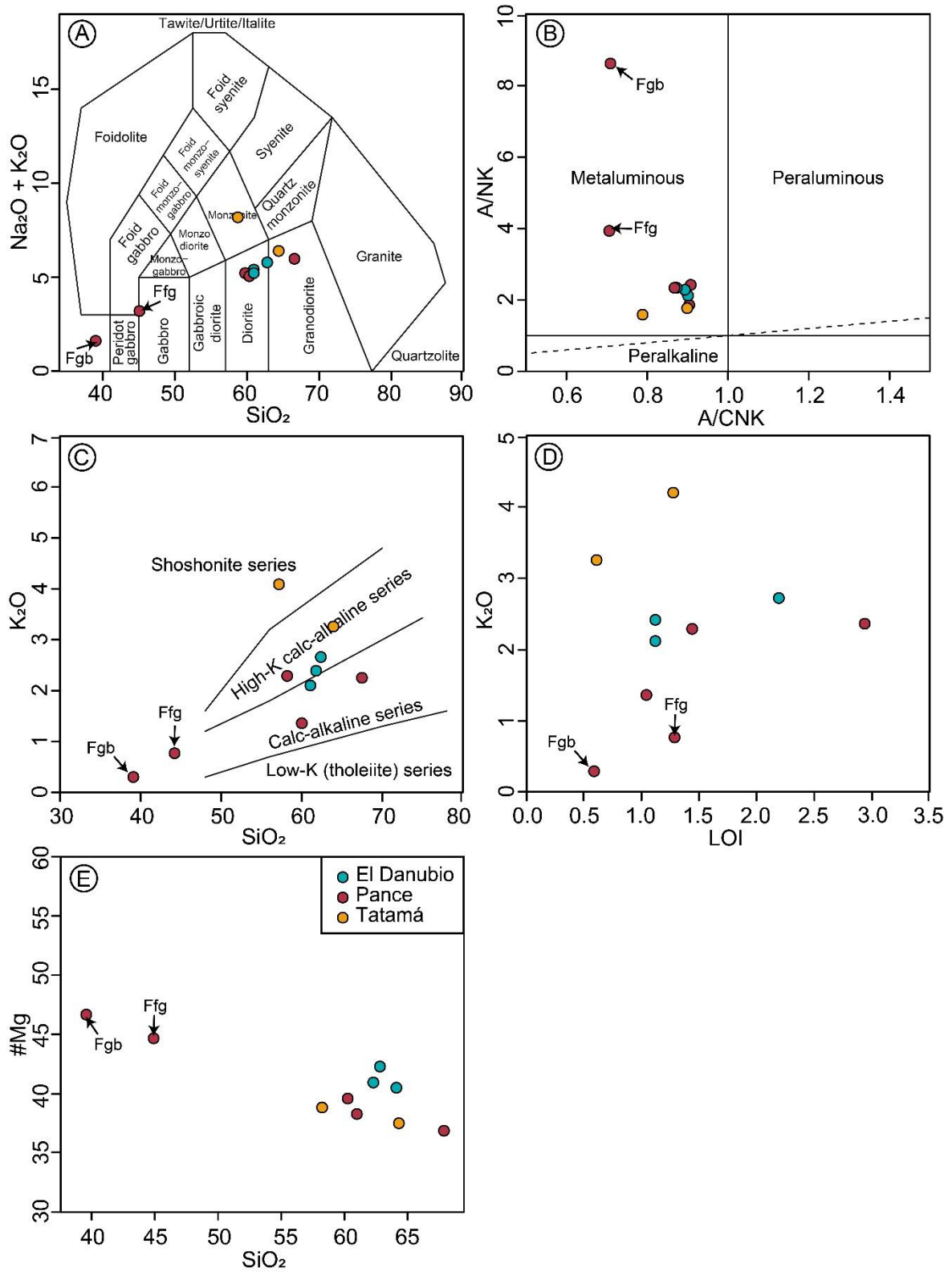
Figure 11. Geochemical diagrams for the studied plutonic rocks from the El Danubio, Pance and Tatamá plutons. A. Classification based on the TAS diagram of Middlemost

(1994), B. A/NK [molar ratio $Al_2O_3/(Na_2O+K_2O)$] versus A/CNK [molar ratio $Al_2O_3/(CaO + Na_2O+K_2O)$] diagram (Shand, 1943), C. K_2O versus SiO_2 diagram (Peccerillo and Taylor, 1976), D. K_2O content versus LOI values, E. SiO2 versus # Mg. Abbreviations: Ffg: foliated hornblende gabbro facies, Fgb: Clinopyroxene hornblende gabbro facies.

Loss-on-ignition (LOI) values range between 0.59 and 2.94 wt% (Fig. 11 D). There is no correlation between LOI values and K_2O content, indicating that the enrichment in K_2O is not due to rock alteration processes. Magnesium number [#Mg= MgO/(FeOt+MgO)*100] ranges from 36.9 to 46.8, and it clearly decreases with the increase in the SiO_2 contents (Fig. 11E).

SiO_2 exhibit a strong negative correlation with Al_2O_3, CaO, MgO, FeOt, TiO_2 and P_2O_5, and positive correlations of SiO_2 with Na_2O and $K2O$ which may be related to magmatic differentiation (Fig. 12). Although, the K_2O contents show a more dispersed trend (Fig. 12C).
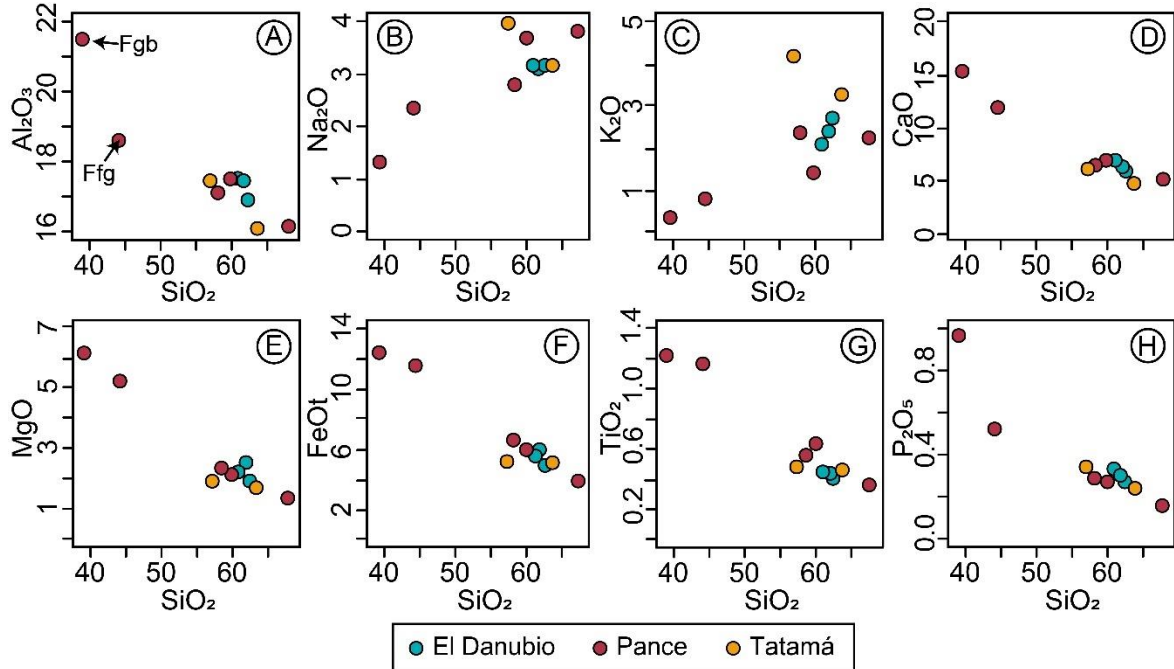
Figure 12. Harker bivariate diagrams showing the relation of major oxides for the studied plutonic rocks from the El Danubio, Pance and Tatamá plutons. Abbreviations: Ffg: foliated hornblende gabbro facies, Fgb: Clinopyroxene hornblende gabbro facies.
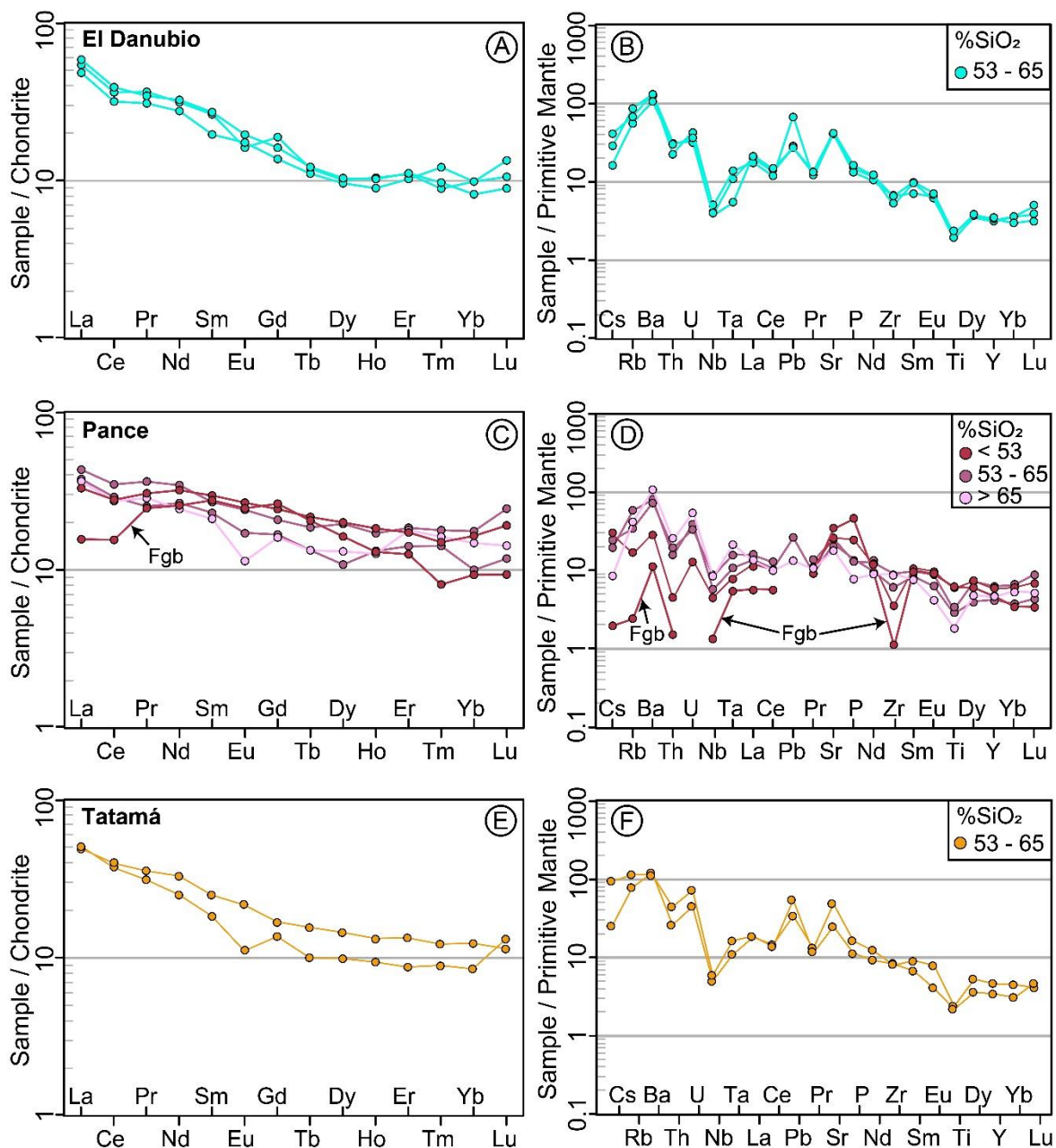
Figure 13. Chondrite-normalized REE variation diagrams (**A, C, D**), and primitive mantle-normalized trace element diagrams (**B, D, F**) for the studied plutonic rocks. Normalization values are according to McDonough & Sun, (1995). The color varies according to the SiO2 content within the samples in each pluton. Abbreviation: Fgb: Clinopyroxene hornblende gabbro facies.

The samples show steep rare earth-element (REEs) patterns with [La/Yb]$_N$ ratio ranging between 4.9-7.1, 1.6-3.7 and 3.9-5.9 for the El Danubio, Pance and Tatamá plutons,

respectively (Fig. 13A,C,E). They show enriched in the light rare earth (LREE) patterns with [La/Sm]$_N$ ratios between 1.1 and 2.7, as well as a depleted and slightly concave-upward Middle-Heavy REEs patterns with [Sm/Yb]$_N$ ratio between 1.4 and 3.3. Complex pattern is evident in the Clinopyroxene hornblende gabbro facies (Fgb) from the Pance pluton, which are characterized by a depleted LREE patterns ([La/Sm]$_N$ = 0.5).

Primitive mantle-normalized trace element diagrams reveal that most the plutonic rocks are enriched in Cs, Rb, Ba, U, Pb, and Sr, and depleted in HFSEs, showing negative anomalies of Nb, Zr and Ti (Fig. 13B, D, and F). Additionally, the clinopyroxene hornblende gabbroic facies exhibit depletion in Cs, Rb, Ba and Zr contents (Fig. 13D). The values of Nb, Y, and Rb in the studied plutons are characteristic of subduction-related volcanic arc granites, as proposed in the tectonic discrimination diagrams of Pearce et al. (1984) (Fig. 14).
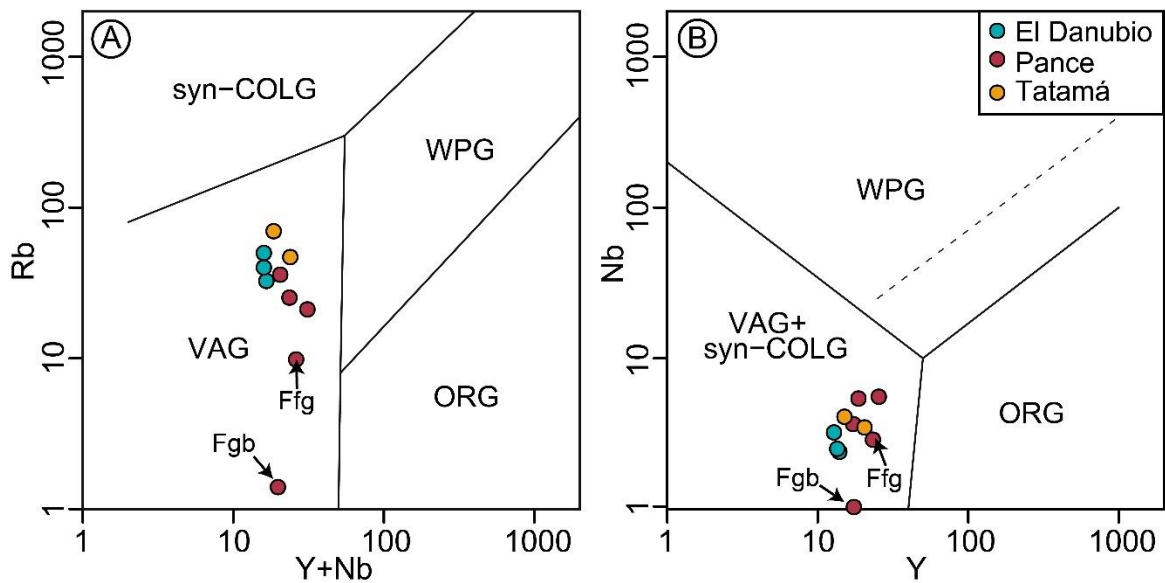
Figure 14. Granitoid tectonic discrimination diagram according to Pearce et al. (1984). Abbreviations: Fqm: quartz-monzodiorite facies, Fgb: clinopyroxene hornblende gabbro facies; VAG: volcanic arc granites, ORG: oceanic ridge granites, WPG: within plate granites, syn-COLG: syn-collisional granites.

The Sm/Yb ratios range between 1.2 and 3.1 for the three studied plutons, indicating a magmatic source formed under relatively low-pressure conditions, in the pyroxene stability field (Fig. 15A). The mafic and intermediate rocks of the analyzed plutons exhibit notable differences in the Th/Nb, Th/La, and La/Yb ratios (Fig. 15B-C). The foliated hornblende

gabbro (sample PS12) and clinopyroxene-hornblende gabbro (sample BSVC6) from the Pance Pluton have low Th/Nb (~0.1), Th/La (<0.1), and La/Yb (2.4-2.9) ratios. In contrast, the intermediate tonalitic and granodioritic rocks from all plutons show higher Th/Nb (0.2-0.9), Th/La (0.1-0.3) and La/Yb (3.6-10.4) ratios (Fig. 15B-C).
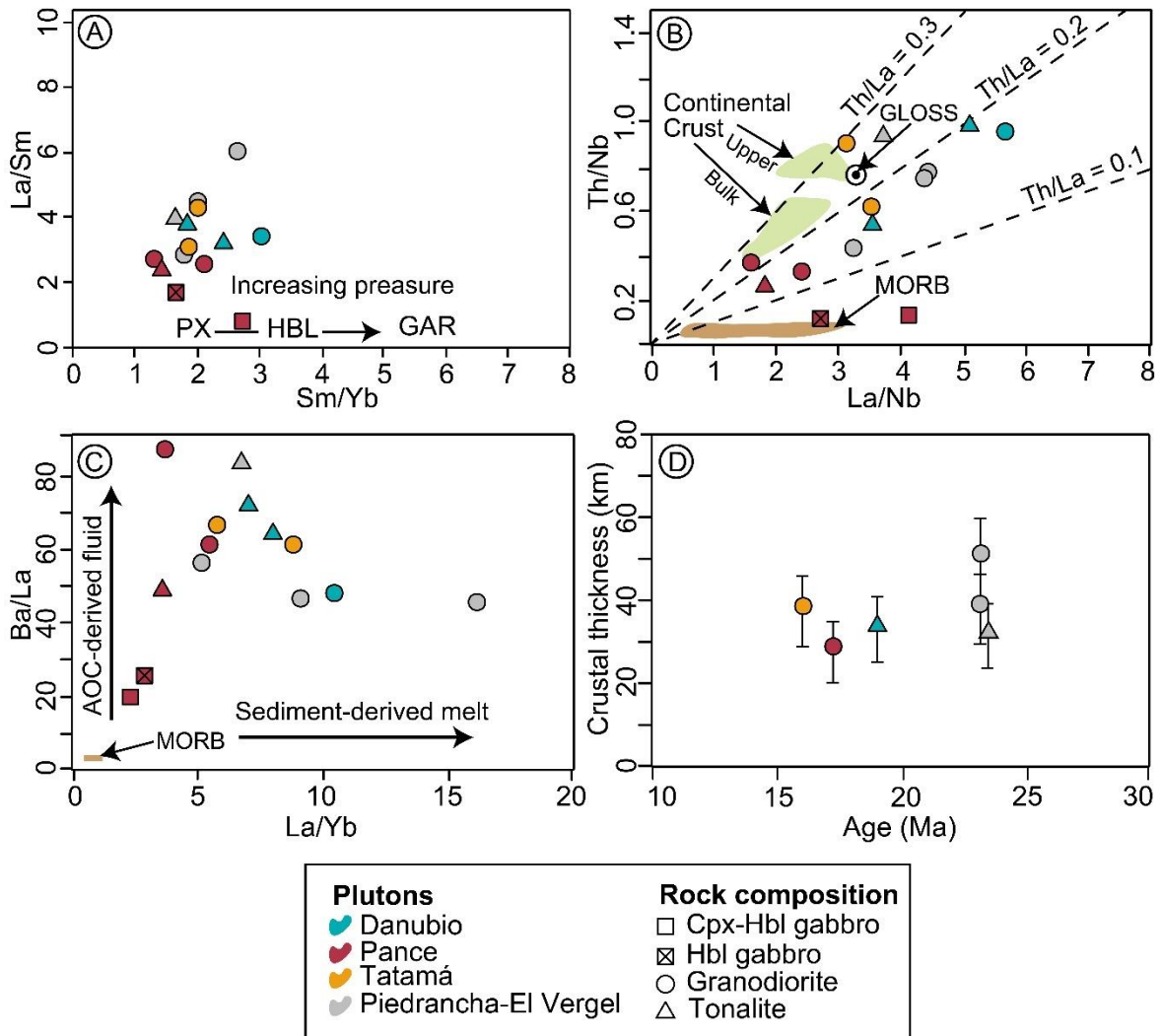
Figure 15. A. Sm/Yb vs. La/Sm ratios; Sm/Yb reflects pressure conditions in magma melting source according to Kay et al., (1991). B. Th/Nb vs La/Nb ratios. Continental crust, Mid-ocenan ridge basalts (MORB) and global subducting sediments (GLOSS) fields are taken from Plank (2005). C. Ba/La vs. La/Yb ratios. Ba/La indicating altered oceanic crust (AOC)-derived fluid contribution and La/Yb suggesting subducted sediment-derived melt (Liu et al., 2024). D. Moho depths or crustal thickness calculated using (La/Yb)$_N$ ratios according Profeta et al (2015).

The $(La/Yb)_N$ ratios were used to estimate the Moho depths or crustal thickness below which mantle derived magma are initially fractionated, according to the empirical equation calibrated by Profeta et al (2015). These values approximate the seismically inferred Moho depth providing a robust proxy of crustal thickness (e.g. Lieu & Stern, 2019). The $(La/Yb)_N$ ratios indicate a Moho depth of 34.1 ± 6.7 km, 28.5 ± 6.2 km, 38.5 ± 7.1 km for the Danubio (sample BSVC2), Pance (sample PS02) and Tatamá (sample TP06) plutons, respectively (Fig. 15D).

In Figure 15, we have also plotted the published data for the Piedrancha and El Vergel plutons (Leal-Mejía et al., 2019), which are in the southernmost section of the Western Cordillera (Fig. 1B). The compiled data from tonalites and granodiorites of both plutons exhibit comparable geochemical patterns to those observed in the intermediate rocks from the Danubio, Pance, and Tatamá plutons.

4.4 Zircon chemistry and Hf isotopes

Trace element concentrations and Hf isotopes in zircons for the analyzed samples (BSVC2, PS02, and PS12) are given in the Supplementary Table 4.

Zircon crystals from the El Danubio and Pance plutons display similar chondrite-normalized REE patterns, with a steeply rising slope due to the enrichment of HREE relative to LREE as seen in igneous zircons (e.g. Hoskin & Schaltegger, 2003). They show positive Ce anomaly (Fig. 16A) with Ce/Ce* ratios ranging from 6.1 to 1451.7 (Fig. 16B). The granodiorite facies from the El Danubio Pluton record the highest Ce/Ce* values ranging between 416.3 and 1451.7 (Fig. 16B), associated with the lowest La values (<0.05 ppm) in the zircons of this rock (Fig. 16A). Additionally, all zircons display a weakly negative Eu anomaly (Fig. 16A) with Eu/Eu* ratios vary between 0.6 and 0.9 (Fig. 16B). For the Pance zircons, these ratios show a relative decrease from the dioritic facies (0.9-0.7) to the granodiorite facies (0.7-0.6). Variations in Eu/Eu* ratios can be attributed to the fractionation of plagioclase during the crystallization of this pluton (e.g. Tang et al., 2020).

Analyzed zircons present a narrow range of Ti values varying between 4.8 and 5.7 ppm, and variable Hf concentrations range between 7832. 1 and 19465.2 ppm, in which those

from the Pance pluton present the highest Ti and Hf values (Fig. 16C). Th/U ratios vary between 0.1 and 1.2 (Fig. 16D, E), which agree with the expected values from zircons crystallized in magmatic environments (e.g., Corfu et al., 2003). A generally negative trend is observed between the Th/U ratios and Hf concentrations within El Danubio and Pance samples (Fig. 16D), which is a typical behavior observed during the compositional evolution (Claiborne et al., 2010; Kirkland et al., 2015). Additionally, the zircon crystals display decreases in the Th/U ratios with increasing values of $(Yb/Gd)_N$ (Fig. 16E), that corresponds to progressively differentiation of the magma, probably due to the ubiquity of hornblende and sphene in these plutonic rocks (Bell & Kirkpatrick, 2021; Barth et al., 2013; Claiborne et al., 2010).

Finally, the isotopic compositions of Hf, expressed as εHf, in magmatic zircons from the El Danubio Pluton exhibit values between +10.3 and +13.2 (Fig. 16F), while the Pance Pluton exhibits relatively higher εHf(t) values between +11.5 and + 13.5 for the granodiorite and between +13.2 and +14.2 for the foliated hornblende gabbro, (Fig. 16F). In Tatamá Pluton, the granodiorite from the main body present εHf(t) values between +6.4 and +8.5, meanwhile the granodiorite from the aphophysis exhibit values ranging +11.8 and 14.3 (Fig. 16F).

.
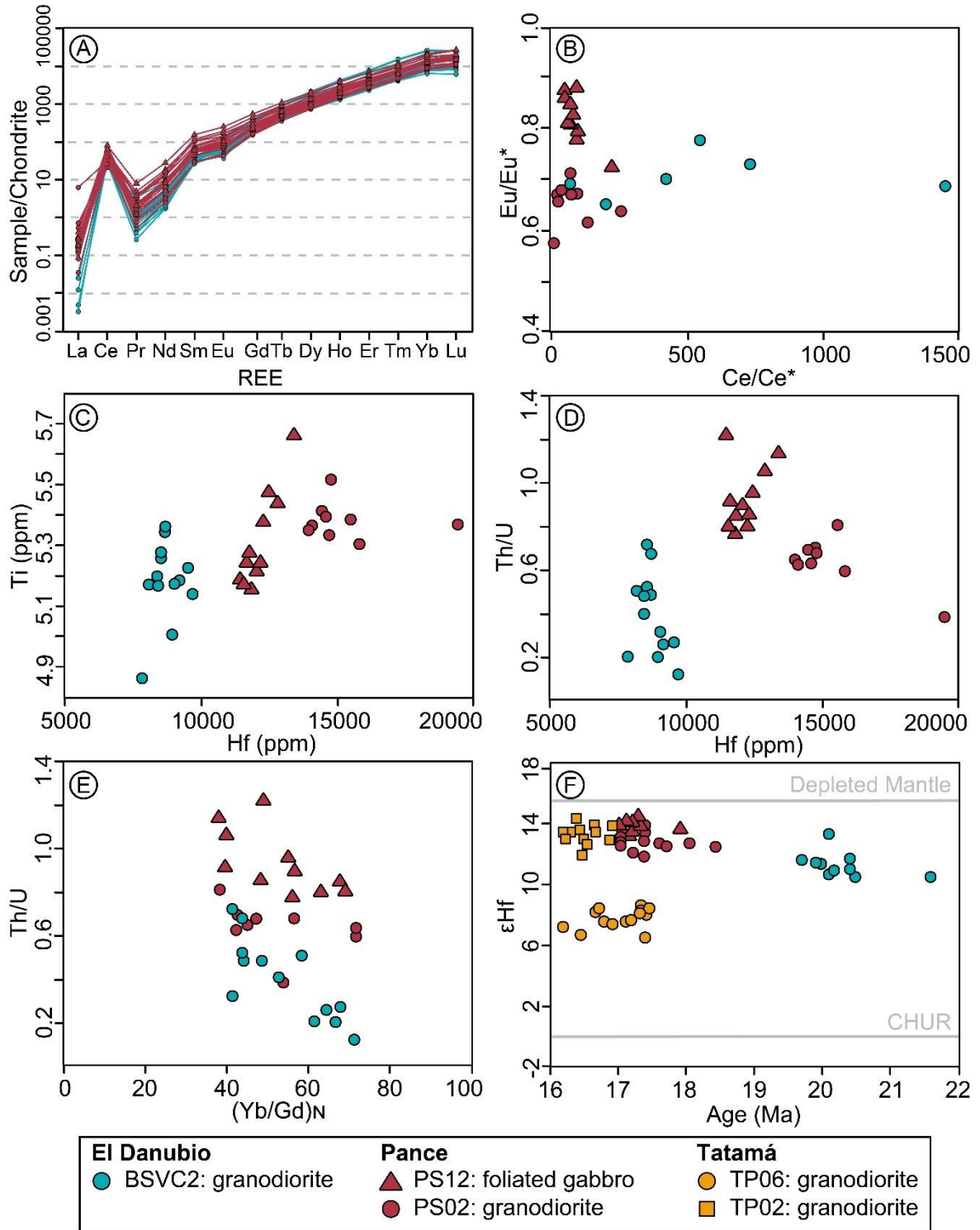
Figure 16. A. Spider plot of REE normalized to chondrite (McDonough and Sun, 1995), **B.** Eu/Eu* vs Ce/Ce* ratios, **C.** Ti vs Hf concentrations, **D.** Th/U ratios vs Hf

concentrations, **E.** Th/U vs. $(Yb/Gd)_N$ ratios, normalized to chondrite (McDonough and Sun, 1995), **F.** Crystallization age vs εHf.

4.5 Mineral chemistry

Four samples were selected for mineral chemistry analyses including the El Danubio granodiorite (BSVC2), the Pance gabbro (BSVC6), the Tatamá foliated granodiorite (PT06-2), and the apophyses of the porphyritic granodiorite (PT02). The EPMA dataset for this work included chemical analysis of plagioclase (87), clinopyroxene (5), amphibole (70), and biotite (26) which are present in Supplementary Table 5. Mineral compositional variations among the studied plutonic rocks are described in the following sections.

4.5.1 Feldspars

Plagioclase crystals from the El Danubio and Tatamá granodiorites exhibit significant compositional variations (Fig. 17A). Core-to-rim profiles in plagioclase crystals (Fig. 18A, E, G) show normal zoning with compositions ranging from labradorite to albite (An_{60-10}) in the El Danubio granodiorite, and from mainly andesine (An_{49-33}, main body) and labradorite to andesine (An_{62-31}, apophyses) in the Tatamá granodiorites. On the other hand, the analyzed plagioclase crystals from the Pance gabbro are represented by an anorthite to bytownite compositional trend (An_{92-88}; Fig. 17A, 18C).

4.5.2 Pyroxenes

In the Pance gabbro, clinopyroxene crystals are mainly classified as diopside with one single crystal classified as augite (Fig. 17B). They present average compositions of $Wo_{45}En_{40}Fe_{12}$ and $Wo_{44}En_{41}Fe_{13}$ with #Mg contents of 77.5 and of 76.9, respectively (Fig. 18C).

4.5.3 Amphiboles

Calcic amphiboles are the main mafic phases in the El Danubio, Pance and Tatamá plutons with cationic variations in the B-site varying $0.87 ≤ {}^B Ca/{}^B(Ca+Na) ≤ 1.0$. The calcic varieties are ferri-tschermakite, ferri-sadanagaite, magnesio-hornblende, and magnesio-hastingsite in the El Danubio granodiorite, ferri-sadanagaite and magnesio-hastingsite in the Pance gabbro, and magnesio-hastingsite in the Tatamá granodiorites (Fig. 17A).

Amphiboles from the El Danubio granodiorite are characterized by #Mg contents between 41 and 47 and total Al contents (Al_T) between 2.0 and 2.2 apfu (Fig. 18B). Amphiboles from the Pance gabbro present #Mg and Al_T values vary between 68 and 70 and from 2.1 to 2.4 apfu, respectively (Fig. 18C, D). For the Tatamá granodiorite rocks, the #Mg values are between 39 to 61, and the Al_T contents slightly vary from cores to rims amphibole crystals (Fig. 18F, H), with values from 1.6 to 2.2 apfu (sample PT06-2, main body) and from 1.2 to 2.6 apfu (sample PT-02, apophyses). Moreover, Ti contents of amphibole crystals are between 0.1 and 0.2 apfu in all studied plutons, and Fe^{+3}/Fe^{+2} ratios range from 1.0 to 1.7 in El Danubio Pluton, 0.3 to 0.6 in Pance Pluton, and 0.1 to 0.5 in the Tatamá Pluton.

4.5.4 Biotites

The ternary diagram TiO_2–FeO*–MgO (FeO* = FeO + MnO) is proposed as a quantitative objective tool for distinguishing between primary magmatic biotites and those that are more or less complete reequilibration within a late-magmatic hydrothermal fluid or a neocrystallization at equilibrium with that fluid, or in another even later one proposed by Nachit et al., (2005). Biotite in the El Danubio granodiorite is classified as re-equilibrated biotite (Fig. 17D). This is consistent with the petrographic features, where some amphibole crystals are replaced by biotite. By contrast, the biotite crystals for the Tatamá granodiorites plot in the transition of primary and re-equilibrated biotite, in agreement with the petrographic descriptions (Fig. 17D). Figure 17E depicts the feal vs. mgli classification diagram proposed by Tischendorf et al. (2007), in which the biotite crystals classify as Al-Mg annite for the El Danubio pluton and Fe-phlogopite for the Tatamá rocks.
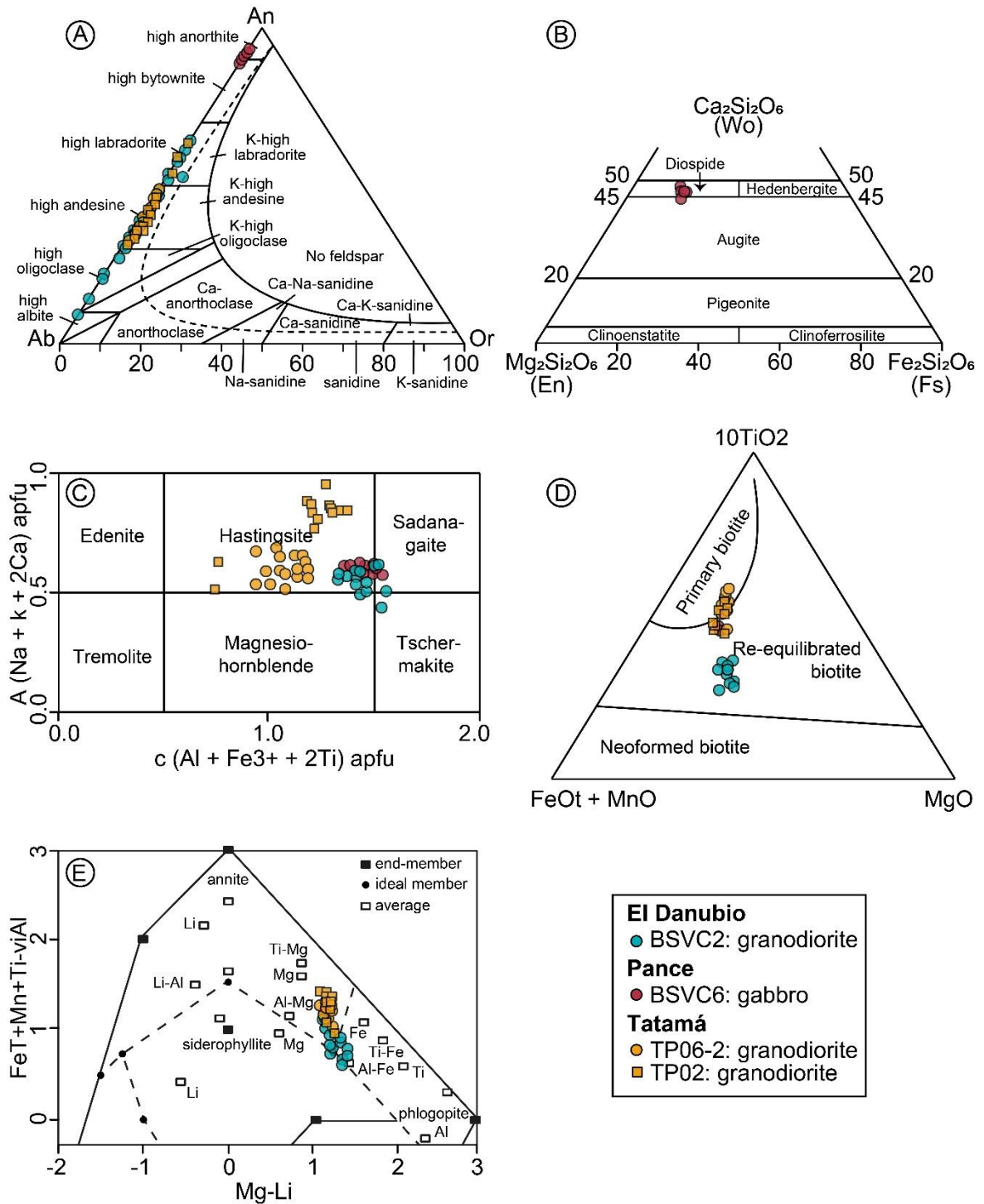
Figure 17. A. Anorthite (An) – Albite (Ab) – Orthoclase (Or) molecular ternary plot (Deer et al., 2013) for feldspar crystals. **B.** Wollastonite (Wo) – Enstatite (En) - Ferrosilite (Fs) molecular ternary plot (Deer et al., 2013) for pyroxene crystals. **C.** Classification diagram according to Hawthorne et al. (2012) for amphibole crystals. **D.** 10*TiO₂ –

FeO – MgO ternary diagram (Nachit et al., 2005). **E.** Classification feal (FeT + Mn + Ti - viAl) vs. mgli (Mg - Li) diagram according to Tischendorf et al. (2007).
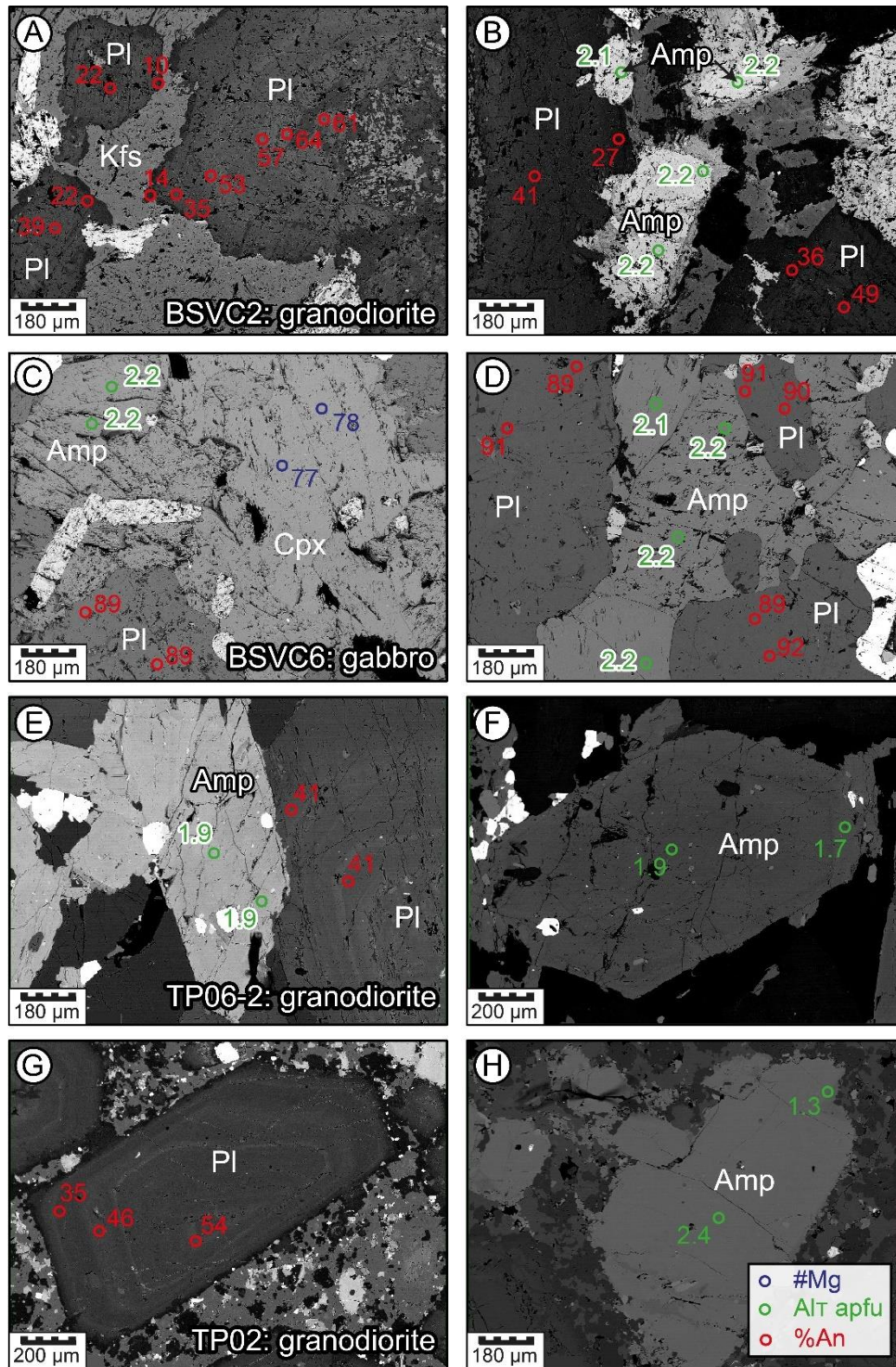
Figure 18. Compositional variation of the percentage of anorthite in feldspar (%An), the amount of magnesium in clinopyroxene (#Mg) and total aluminum (AlT) in atoms

per formula unit (apfu) for amphibole in the analyzed rocks of the plutons: El Danubio (**A-B**), Pance (**C-D**), and Tatamá (**E-H**). Abbreviation: Pl: plagioclase, Kfs: K-feldspar, Cpx: clinopyroxene and Amp: amphibole.

4.6 Intensive crystallization parameters

Depths of the magma diversification, thermobarometry calculations (P-T), oxygen fugacity (logfO$_2$) and water content (H2Omelt) conditions of the studied plutons, based on zircon, plagioclase, clinopyroxene, amphibole and biotite chemistry and whole-rock compositions are presented as follows. Mean values of the calculated intensive crystallization conditions are summarized in Table 2.

4.6.1 Moho depths or crustal thickness

We used (La/Yb)$_N$ ratios to quantify the crustal thickness that reflects the average depth at which magmatic fractionation occurred (Profeta et al., 2015). (La/Yb)$_N$ ratio indicates a average depth of 34.1 ± 6.7 (n=1), 28.5 ± 6.2 (n=1), 38.5 ± 7.1(n=1) for the El Danubio, Pance and Tatamá plutonic rocks, respectively. These results suggest that the differentiation of the Lower Miocene plutons occurred within a normal crust with a thickness of 28-38 km. Additionally, Eu/Eu* ratios in zircon were used to calculate the crustal thickness (Tang et al., 2020), obtaining values between 80.4 ± 9.4 (n= 9) and 93.1 ± 10.8 km (n= 11).

The depths >70 km will not be considered in this work because they don't agree with the low-pressure fractionation conditions obtained for magma within the stability field of pyroxene (Fig. 15C). For a magma formed under a thick crust, fractionation in the presence of garnet would be expected. It is possible that the data calculated do not represent the real values of cortical thickness because Eu/Eu* ratios may be affected by variations in the redox state of the melts, magmatic evolution processes and the crystallization sequence in granitic rocks (Yakymchuk et al., 2023).

4.6.2 Temperature

Clinopyroxene thermometric calculations proposed by Putirka et al. (1996) and Wang et al., (2021a) were employed to determine the crystallization temperatures of this mineral in the

Pance's gabbro. Calculations with the Putirka et al. (1996)'s model, which relies on clinopyroxene-liquid equilibria, yields temperatures between 1160° and 1191°C (mean = 1175 ± 246°C). We obtained lower temperature estimations from the clinopyroxene-only thermometer developed by Wang et al. (2021a), yielding temperatures between 1072°C to 1079°C with an average value of 1076°C ± 36°C (Table 2). For discussion purposes, we opted to select the crystallization temperatures derived from the Wang et al (2021) method, because it does not necessitate information on coexisting silicate melt or other co-crystallized mineral phases, and due to its greater accuracy and precision relative to Putirka et al (1996). According with the petrographic observation, clinopyroxene temperature estimations represent near-liquidus thermal conditions of the gabbroic magma in the Pance Pluton.

Apatite saturation temperatures (TsatAp) were estimated for the quartz-monzodiorite, tonalite, and granodiorite rocks among the three plutons. TsatAp were determined using the SiO_2 and P_2O_5 values from the whole-rock compositions according to the method proposed by Harrison and Watson (1984). Estimated temperatures range between 803°C to 941°C (Table 2). These results are petrologically consistent with the near-liquidus temperatures expected for plutonic systems (Anderson et al. 2008) and by the common occurrence of early crystallized apatite crystals included in amphibole and biotite (Fig. 6). Ti concentrations of the analyzed zircons were used to calculate the related crystallization temperatures by using the Ti-in-zircon thermometer of Ferry and Watson (2007). This takes into account the Ti content in zircon, along with the activation energy values for TiO_2 (aTiO2) and SiO2 ($aSiO_2$ in each rock. We assumed a value of $\alpha TiO_2 = 0.6$ for all plutonic rocks, whereas the αSiO_2 was 1.0 for the granodiorites, except for the foliated hornblende gabbro rock where $\alpha SiO_2 = 0.9$, in agreement with the mineralogy in each rock (e.g. Ferry & Watson, 2007; Hayden & Watson, 2007; Schiller and Finger 2019).

Calculated Ti-in-zircon temperatures (TTi-in-Zr) in the granodiorites are very similar and vary from 726 to 735°C (mean = 732 ± 45°C, El Danubio Pluton) and from 734 to 738°C (mean = 735 ± 45°C, Pance Pluton). In contrast, zircons from the Pance's foliated hornblende gabbro crystallized between 722°C to 731°C (mean = 724 ± 45°C), recording the lowest temperatures among the studied plutonic rocks (Table 2). Notably, the Ti-in-zircon crystallization temperatures are lower than both the apatite saturation temperatures. These results contrast with our prior petrographic findings regarding the early stage of

zircon crystallization within the examined rocks (Fig. 6), because the crystallization temperature obtained for zircon is lower than the crystallization temperature of amphibole as will be described below. It is possible that these temperatures are lower than expected because the $aSiO_2$ and $aTiO_2$ values of each analyzed rock are being overestimated or underestimated. Therefore, we have chosen not to consider these Ti-in-zircon calculations as representative of near-liquidus temperatures for further discussion.

We integrated and compared various thermometric calibrations, including the amphibole-plagioclase thermometric model (Equation B) of Holland and Blundy (1994) and different amphibole-only thermometers (Equations 5 and 6) of Putirka (2016), of Liao et al., (2021), and of Ridolfi (2021), to determine the crystallization (close-to-solidus) temperatures of the Pance gabbro, and the El Danubio and Tatamá granodiorites. For the Pance gabbro, the amphibole yielded average temperatures ranging from 820°C ± 35°C and 959°C ± 30°C (Table 2). For El Danubio granodiorite, the average temperatures range between 722 ± 35°C and 868 ± 22°C. Similarly, for the Tatamá granodiorites, the average temperature varies between 749 ± 40°C and 858 ± 30°C in the main body, and 764 ± 40°C and 897 ± 22°C in the apophyses (Table 2).

The amphibole crystallization temperatures, determined through the Putirka (2016) and Ridolfi (2021) thermometers, are notably higher than the H2O-rich granite solidus (Johannes & Holtz, 1996). Consequently, we interpreted the results obtained from the models of Holland and Blundy (1994) and Liao et al. (2021) as the most reliable estimations for the close-to-solidus crystallization temperature of the Pance's gabbro and the El Danubio and Tatamá granodiorites. However, in this work the Liao et al. (2021) thermometer will be used because it could be applied to gabbroic and granodioritic rocks.

4.6.3 Pressure

We employed the clinopyroxene-liquid barometer of Putirka et., al (1996) to constrain the pressure conditions of the Pance gabbro. The calculated pressures range from 8.1 ± 1.4 kbar to 8.9 ± 1.4 kbar. Considering the petrographic textures, which indicate that clinopyroxene was among the first mineral phases to precipitate in this rock, the mean value suggests a high-pressure crystallization condition for the gabbroic rock at 8.5 ± 1.4 kbar (Table 2).

The pressure and emplacement conditions of the four examined plutonic rocks were determined using a combination of barometric calibrations, including the plagioclase-amphibole model of Molina et al. (2015), and the amphibole-only models of Mutch et al. (2016) and Ridolfi (2021). For the El Danubio granodiorite, the selected barometers give average pressure values between 4.7 ± 0.5 kbar and 6.3 ± 0.5 kbar (Table 2). In contrast, the Tatamá granodiorites registered significantly lower pressures. For the main body, mean pressures range from 2.5 ± 0.5 kbar to 4.8 ± 0.5 kbar (Table 2). Whereas amphiboles in the apophyses exhibit diverse mean pressures, with values of 5.4 ± 0.5 kbar and 6.1 ± 0.5 kbar (Table 2). Using Ridolfi (2021) a low value of 1.27 ± 0.5 kbar was calculated for the amphibole's rims of the Tatamá apophyses (Table 2). Finally, the suitable models of Molina et al. (2015) and Ridolfi (2021) barometry applied for the Pance's gabbro, provided average pressures of 1.8 ± 1.5 kbar and 4.3 ± 0.5 kbar, respectively (Table 2).

Considering the significant differences between the various amphibole barometers (Table 2), we carefully evaluate the thermobarometry results on the P-T diagram (Fig. 19) to identify the most consistent and reliable estimates of pressure conditions for the El Danubio, Pance, and Tatamá rocks. The inferred P-T conditions for the four plutonic rocks fall within the supra-solidus field characteristic of granitoid magmas (Johannes & Holtz, 1996) regardless of the barometer chosen. This suggests that the amphibole pressures obtained likely correspond to a crystallization of this mineral before the final emplacement depth.

In this study, the pressures calculated by Mutch et al. (2016) for the granodioritic rocks of El Danubio and Tatamá will be employed, along with those by Molina et al. (2015) for the Pance gabbro. The barometer proposed by Ridolfi (2021) is dismissed due to limitations in the calibration conditions as pointed out by Erdman et al. (2014), who indicate that the Si-Al ratio used by Ridolfi (2021) does not adequately correlate with pressure. Additionally, the barometer by Molina et al. (2015) presents a dual error in the calculation given that this model requires the input of the amphibole crystallization temperature. Consequently, the barometer proposed by Mutch et al. (2016) is more suitable for estimating crystallization pressure. However, the thermometer by Mutch et al. (2016) was not used for the gabbroic rock due to its limitations in rocks in textural equilibrium with amphibole, plagioclase, biotite, titanite, and apatite.

Accordingly, these crystallization pressures were converted to depths by using an average crustal density of 2.89 g/cm^3, equivalent 1kbar = 3.5 km (Hincapié-Gómez et al; 2018), corresponding to depths of 7 km in the Pance gabbro and between 7 km and 28 km in the El Danubio and Tatamá granodiorites (Fig. 19).
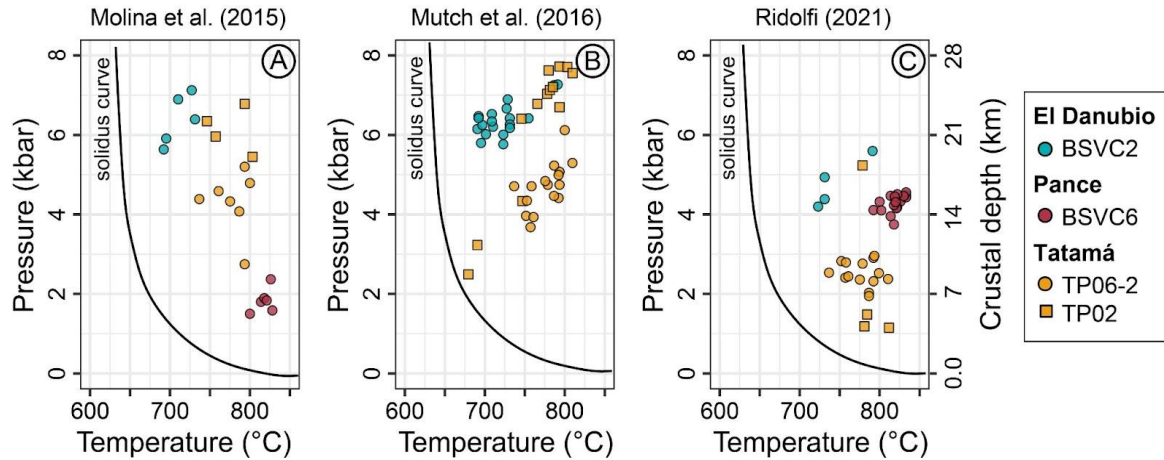
Figure 19. Results of amphibole thermobarometric calculations for the El Danubio, Pance, and Tatamá plutons. Error for Molina et al. (2015), Mutch et al. (2016), and Ridolfi (2021) represent ± 1.5 kbar and ±0.5 kbar uncertainty, respectively. Temperatures calculated according to Liao et al. (2021) with an error of ±35°C. Solidus curve of water saturated granite system according to Johannes & Holtz (1996).

4.6.4 Oxygen fugacity and water content of magmas

Oxygen fugacity (logfO$_2$) and water contents (H$_2$Omelt) in the amphibole were determined following the method proposed by Ridolfi (2021). The results are shown in the logfO$_2$–T diagram (Fig. 20). Estimate redox conditions and logfO$_2$ values, ranging from high to low estimates, are -10.7 ± 0.3 (ΔNNO = 1.6) for the El Danubio granodiorite; -10.4 ± 0.3 (ΔNNO = 2.7) for the Tatamá granodiorite in the main body; -8.5 ± 0.3 (ΔNNO = 3.3) for the Tatamá granodiorite in the apophysis; and -7.9 ± 0.3 (ΔNNO = 3.4) for the Pance gabbro. These results and the Mg-rich compositions of the amphiboles from the studied rocks suggest a primary oxidized crystallization environment for the parental magmas, above the NNO+3 buffer (Fig. 20).

Redox conditions for the studied magmas were also constrained using the trace element compositions of zircons (Fig. 20). The obtained values show lower oxidizing conditions

plotting near or under the NNO buffer, with $logfO_2$ values of -15.4 ± 0.6 (ΔFQM = 1.4) for the El Danubio granodiorite; of -15.4± 0.6 (ΔFQM = 0.8) for the Pance foliated hornblende gabbro; and of -15.5 ± 0.6 (ΔFQM = 0.8) for the Pance granodiorite.

The magnesium number (#Mg) and total aluminum (AlT) for the biotites in the El Danubio and Tatamá plutons, which range between 43.9 and 58.1 for #Mg and 2.6 to 3.1 for AlT, indicate that these biotites crystallized in the stability field of the magnetite series, suggesting an oxidized magmatic source, as indicated by Anderson (2008) and Ishihara (1977).
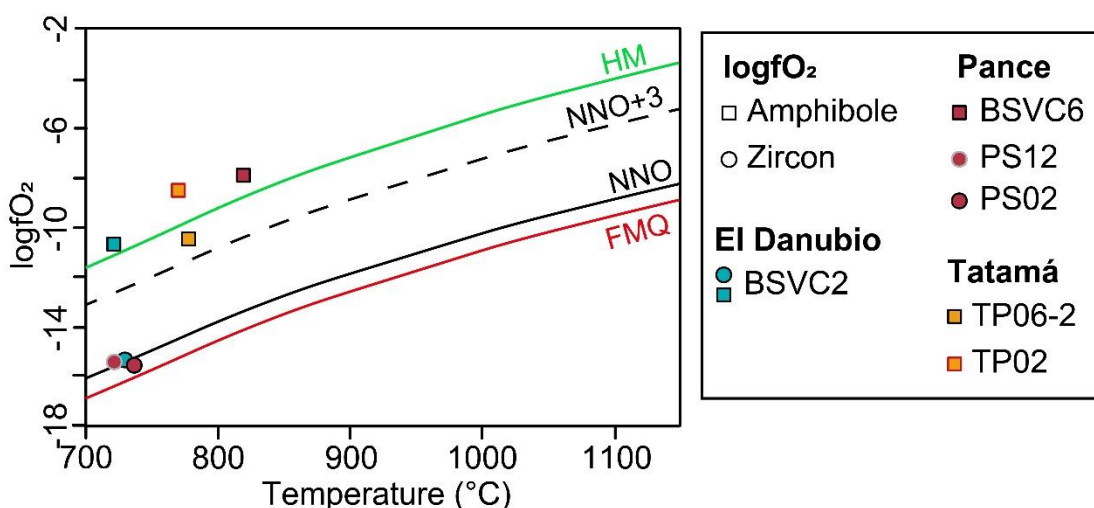
Figure 20. $logfO_2$ versus temperature showing the Fayalite-Magnetite-Quartz (FMQ), Nickel-Nickel Oxide (NNO) and Hematite-Magnetite (HM) buffers. Temperatures calculated according to Liao et al. (2021) with an error of ±35°C.

The estimated water concentrations in the amphibole-precipitation melt range from 8.3 to 8.6 wt.% H_2O in the Danubio granodiorite, from 5.2 to 8.4 wt.% H_2O in the Tatamá granodiorites, and from 6.6 to 7.19 wt.% H_2O in the Pance gabbro (Supplementary Table 5). These findings indicate that the studied magmas were enriched in water, aligning with the typical characteristics of calcic amphiboles crystallized in arc-related systems (e.g., Ridolfi et al., 2010).

Table 2. Summary of the crystallization conditions obtained for apatite, zircon, clinopyroxene and amphibole present in the different rocks of the El Danubio, Pance and Tatamá plutons. Abbreviations: n.a: not applied, n.d: no data.

PLUTON	Error	EL DANUBIO		PANCE			TATAMÁ	
Sample		BSVC2	BSVC3	BSVC6	PS12	PS02	TP06-02	TP02
					Foliated			
Rock Type		Granodiorite	Tonalite	Gabro	gabbro	Granodiorite	Granodiorite	Granodiorite
Depth of magmatic diversification (km)	**Error**							
Profeta et al. (2015) - (La/Yb)N		n.a	34.1 ± 6.7	n.a	n.a	28.6 ± 6.2	38.5 ± 7.1	n.a
Profeta et al. (2015) - Sr/Y		n.a	73.8 ± 3.1	n.a	n.a	35.1 ± 0.3	44.9 ± 0.9	n.a
Tang et al. (2020)		84.0 ± 9.8	n.d	n.d	93.1 ± 10.8	80.4 ± 9.4	n.d	n.d
Temperatures (°C)								
Apatite T_{satAp} (Harrison and Watson, 1984)		945	935	n.a	n.a	891	930	895
Zircon $T_{Ti-in-Zr}$ (Ferry and Watson, 2007)	± 45	732	n.d	n.d	724	735	n.d	n.d
Clinopyroxene $T_{Cpx-Liq}$ (Putirka et al., 1996)	± 246	n.d	n.d	1175	n.d	n.d	n.d	n.d
$T_{Cpx-only}$ (Wang et al., 2021)	± 36	n.d	n.d	1076	n.d	n.d	n.d	n.d
Amphibole $T_{Pl-Hbl\ Eq.B}$ (Holland and Blundy 1994)	± 40	733	n.d	n.a	n.d	n.d	749	764
$T_{Hbl-only\ Eq.5}$ (Putirka, 2016)	± 30	858	n.d	959	n.d	n.d	858	875
$T_{Hbl-only\ Eq.6}$ (Putirka, 2016)	± 28	855	n.d	953	n.d	n.d	856	870
$T_{Ti-in-Hbl}$ (Liao et al., 2021)	± 35	722	n.d	820	n.d	n.d	777	771
$T_{Hbl-only}$ (Ridolfi, 2021)	± 22	868	n.d	930	n.d	n.d	831	897
Pressures (kbar)								
Clinopyroxene $P_{Cpx-Liq}$ (Putirka et al., 1996)	± 1.4		n.d	8.5	n.d	n.d	n.d	n.d
Amphibole P_{Pl-Hbl} (Molina et al., 2015)	± 1.5	6.2	n.d	1.4	n.d	n.d	4.6	6.1
$P_{Hbl-only}$ (Mutch et al., 2015)	± 0.5	6.3	n.d	n.a	n.d	n.d	4.8	5.1
$P_{Hbl-only}$ (Ridolfi, 2021)	± 0.5	4.7	n.d	4.2	n.d	n.d	2.5	core = 5.4 rim = 1.3
Oxygen fugacity (log_{fo2})								
Zircon Trace element-in-Zrn (Loucks et al., 2020)	± 0.6	-15.4	n.d	n.d	-15.4	-15.5	n.d	n.d
ΔFMQ		1.4	n.d	n.d	0.8	0.8	n.d	n.d
Amphibole Hbl-only (Ridolfi, 2021)	± 0.3	-10.7	n.d	-7.9	n.d	n.d	-10.4	-8.5
ΔNNO		1.6	n.d	3.4	n.d	n.d	2.7	3.3
Water Contents (H_2O wt.%)								
Amphibole Hbl-only (Ridolfi, 2021)	± 14	8.5	n.d	6.8	n.d	n.d	7.6	7.7

5.Discussion

Geochronological constraints from El Danubio, Pance and Tatamá plutons, integrated with published data from other Early Miocene plutonic bodies exposed in the Western Cordillera of Colombia (Barbosa-Espitia, 2020; Echeverri et al., 2015; Leal-Mejía et al., 2019; González, 2002), indicate the existence of an Early Miocene mafic to intermediate arc magmatic activity from 23 Ma to 15 Ma. This chapter presents a discussion of the magmatic evolution of the three studied plutons, from their magma source to the final emplacement in the upper plate. Subsequently, we evaluate the relationship between petrogenesis of the Early Miocene magmatism and the Neogene tectonic reorganization that characterized the northwestern part of South America.

5.1 Petrogenesis

The presence of hornblende, titanite, and apatite together with the calc-alkaline, metaluminous and magnesian signatures, the whole-rock negative anomalies of Nb, Zr, Ti, and the high LILE/HFSE ratios, suggest that the Danubio, Pance and Tatamá plutons are I-type granitoids formed in subduction settings (Chappel & White, 1974; Pitcher, 1993; Whatman & Stern, 2015).

Due to their more limited differentiation when compared with more siliceous rocks, mafic plutonic rocks can be useful to reconstruct magma sources (Annen et al., 2015). Therefore, the hornblendite, clinopyroxene-hornblende gabbro, and foliated hornblende gabbro rock types from the Pance pluton are key to understand the genesis of the Early Miocene magmatism in the Western Cordillera of Colombia.

The clinopyroxene-hornblende gabbro exhibits relatively low concentrations of LILEs, low Zr content, and high concentrations of Cr and Ni (Fig. 13), as well as high An88-90 contents in the plagioclase composition (Fig. 17A). These geochemical features suggest that this

rock may be associated with mafic cumulates formed during fractionation processes (Castro et al., 2021; Chappell et al., 2004). Given that cumulate rocks can represent a differentiated portion of the original magma (Chappell et al., 2004), this leads to inherent biases in their geochemical signatures, making them unreliable for accurate interpretation of the magma source. Therefore, we excluded this cummulatic gabbro for the interpretation about the magma source. In contrast, compositions from the foliated hornblende gabbro record the typical geochemical signature of I-type granitoids, i.e. high LILEs and low Nb and Ti values, that can be related to a basaltic and mantle derived magmas in the Pance Pluton formed by wet melting.

Hf isotopic values in zircons from the foliated hornblende gabbro show highly positive εHf mean values of ~ +13.8 that are close to the depleted mantle value (εHf of +16 at 0 Ma; Guo & Korenaga, 2023; Iizuka et al., 2017; Nowell et al, 1998). Moreover, low Th/Nb, Th/La, and La/Yb ratios (Fig. 15B-C) from this rock are similar to the ones from basaltic rocks formed in a mid-oceanic ridge setting (MORB) (Turner & Langmuir, 2022; Plank, 2014, 2005). These geochemical signatures suggest a clear asthenospheric source with minor contribution from more evolved materials, such as subducted sediments or continental crust (Fig. 22A) (Guo & Korenaga, 2023; Iizuka et al., 2017).

The more differentiated tonalites and granodiorites from the Danubio, Pance, and Tatamá plutons, show high Th/Nb and Th/La ratios that are relatively close to those recorded in continental crust (Fig. 15B) (Plank 2005, and references therein). Additionally, the εHf mean values of +12.6 (sample PS06, Pance Pluton), +11.1 (sample BSVC2, El Danubio Pluton), and +13.3 (sample TP02, Tatamá Pluton) in the studied rocks (Fig. 16F) supports the asthenospheric magma source in the three plutons. However, one sample of the Tatamá rocks (TP06) also indicates a clear assimilation of more evolved continental material with a εHf mean value of +7.5 (Fig. 16F, 21A).

In the southernmost section of the Western Cordillera (Fig. 1B), the Piedrancha and El Vergel plutons exhibit whole-rock εNd values ranging from +11.8 to -2.9 (Fig. 21) (Leal-Mejía et al., 2019). These data together with our results indicate that the Lower Miocene plutons were formed by a regional asthenospheric source, which was locally modified by the incorporation of non-radiogenic continental material.

The clear contribution of continental material in the Tatamá pluton can be explained by the assimilation of continental crust in of the upper plate or by the contamination of the mantle source (Nebel et al., 2011; Rudnick and Gao, 2003). However, given that the analyzed Tatamá granodiorites are contemporaneous (Fig. 10) and exhibit similar geochemical characteristics of a magma formed in a subduction setting (Figs. 13 and 14), it is possible that both rocks have a single mantelic source and that localized assimilation of continental crust occurred in the upper plate, which would explain the decrease of the εHf values in one of the analyzed Tatamá samples.

The presence of some Jurassic, Triassic and Proterozoic zircons in the Danubio and Tatamá plutons could also support the hypothesis that older continental crust has been assimilated for these plutons, because them were emplaced in the Western Cordillera´s basement, which is mostly composed of a Cretaceous oceanic crust formed in a plateau and intraoceanic arc settings (Villagómez et al., 2011; Weber et al., 2015; Zapata-Villada et al., 2021). Although Jurassic, Triassic and Proterozoic detrital zircons have been identified in the Cretaceous sedimentary sequence of the Western Cordillera (Botero-García et al., 2023), this sequence conform the uppermost crustal levels where the crustal assimilation is not efficient (Annen et al., 2006, 2015) and where the Lu-Hf system in zircon is closed. Therefore, the analyzed granodiorites and tonalites from the Tatamá, Piedrancha and El Vergel plutons suggest that the lower-middle crust of the Western Cordillera may also include fragments of older continental crust associated with the South American Plate.

The melting of a mafic crust requires relatively high geothermal gradients and high-pressure conditions (Macpherson et al., 2006), which often results in the formation of intermediate rocks with adakite-like geochemical signatures, i.e, high La/Yb >9 and Sr/Y >20 and low Y ≤18 ppm and Yb <2 ppm (Defant and Drummond, 1990). Therefore, the absence of adakite-like signatures and low crustal thicknesses (28.5 to 38.5 km) suggest limited assimilation and melting of the mafic basement in the Western Cordillera during the Early Miocene magmatism that formed the El Danubio, Pance and Tatamá plutons.

Compositions of amphiboles and zircon from the studied plutons show high oxygen fugacity values, related to nickel-nickel oxide (NNO) and hematite-magnetite (HM) oxygen buffers (Fig. 20). These elevated oxygen fugacities can be achieved by the presence of oxidized aqueous fluids derived from the dehydration of the oceanic lithosphere and/or by the

assimilation of oxidized continental crust (Brounce et al., 2015; Evans, 2012; Zhang et al., 2021; Grocke et al., 2016). The contribution of oxidized aqueous fluids from the subducted oceanic lithosphere can increase the oxidation state of the mantle wedge by adding Fe^{3+}, C^{4+}, and S^{6+} (Evans, 2012; Evans et al., 2011; Zhang et al., 2021). We therefore suggested that the oxidized aqueous fluids from the subducted oceanic lithosphere (Fig. 22A) may have controlled the magma oxygen fugacity value in the analyzed rocks as high values are recorded in rocks with varied continental crust assimilation.

The studied rocks exhibit magnesium number values between 36.9 to 46.8, which are in disequilibrium with the mantle (#Mg >60), suggesting that the Danubio, Pance, and Tatamá magmas were differentiated by fractional crystallization (e.g. Baliani et al., 2012). Negative correlations between CaO, MgO, FeOT, TiO2, and P2O5 with SiO2 (Fig. 12) can be related to the early crystallization of clinopyroxene, plagioclase, apatite, titanite, and amphibole, as indicated by either their euhedral forms or the occurrence as inclusions, respectively. The increase in K2O with increasing SiO2 together with usually interstitial occurrence of biotite and the poikilitic textures in K-feldspars, imply that these minerals were late-crystallized phases. Moreover, the decrease of the Th/U ratios with increasing of the Yb/GdN values in zircons (Fig.16E), also indicates progressive magma differentiation due to the crystallization of hornblende and sphene (e.g., Bell & Kirkpatrick, 2021; Barth et al., 2013; Claiborne et al., 2010). This is further supported by the normal zoning plagioclase patterns in the intermediate rocks, which also support the fractional crystallization process.

The fractional crystallization of the magmas that formed El Danubio, Pance and Tatamá Plutons occurred at low-pressure conditions, in equilibrium with plagioclase-pyroxene mineral assemblages as suggested by the Sm/Yb ratios (Fig 15A). This is compatible with the crustal thickness values between ~28 km and ~38 km derived from the geochemical data (Fig. 22A).

Furthermore, field observations and petrographic features including the presence of mafic enclaves (e.g., Weinberg et al., 2021), as well as the presence of plagioclase with corroded cores, and zircons with corroded edges in the intermediate rocks (e.g., Scarrow et al., 2021), suggest the existence of mingling processes and probably mixing processes (e.g. Anderson, 1976; Kemp et al., 2007), which are not possible to resolve with the available database.
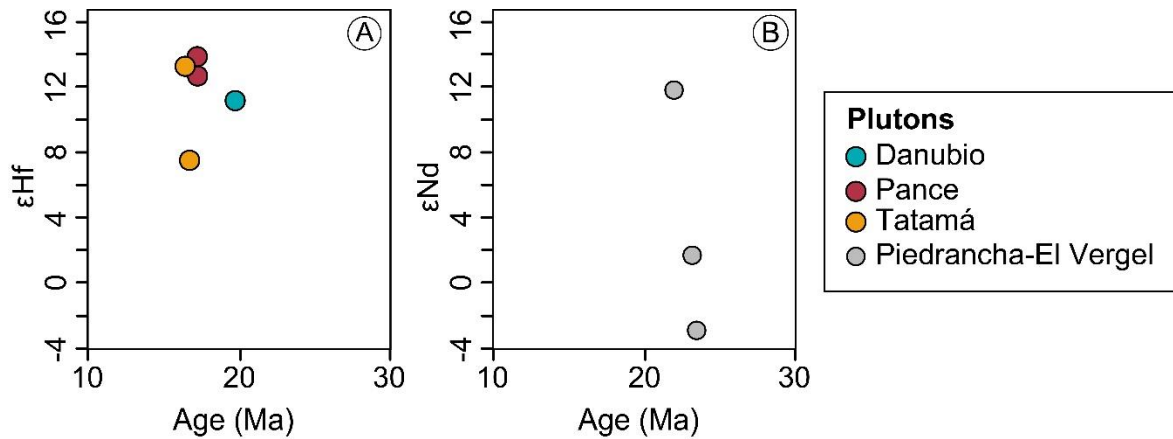
Figure 21. A. Zircon εHf mean values of thel Danubio, Pance and Tatamá plutons (this work), B. Whole-rock εNd values for the Piedrancha and El Vergel plutons (reported by Leal-Mejía et al., 2019).

5.2 Magmatic storage

After their extraction from the mantle, the magmas that formed the Early Miocene plutons migrated through the lower to the upper crust following various stages of crystallization, until reach their fully emplacement in either the volcanic basement or sedimentary cover of the Western Cordillera of Colombia (Nivia, 2001).

Clinopyroxenes from the clinopyroxene-hornblende gabbro of the Pance pluton records the first stage of magmatic crystallization at 1076 ± 36 °C and 8.5 ± 1.4 kbar, which can be interpreted as the near-liquidus thermal conditions. Crustal depths derived from the clinopyroxene pressures and a crustal density of 2.89 g/cm3 (1 kbar = 3.5 km) for the mafic basement of the Western Cordillera (Hincapié-Gómez et al., 2017) yield an average value of 29.8 ± 4.9 km. This depth is similar to the crustal thickness values derived from the (La/Yb)$_N$ (28 km - 34 km), suggesting that these magmas began their crystallization at the base of a normal crust (Fig. 22C).

The analyzed apatite saturation temperature from the granodiorites of the Danubio and Tatamá plutons also represent near-liquidus temperatures ranging from 945°C to 803°C. The estimated amphibole pressures in both plutons indicate crystallization process at

middle to lower crustal levels of ~22 ± 1.7 km in the Danubio pluton, and ~21 to 17 ± 1.7 km in the Tatamá pluton (Fig. 22C). In the Tatamá apophyses, compositions of some amphiboles show pressure conditions between 2 kbar and 3 kbar (Fig. 19), which indicate magma transport reaching the crustal conditions of 7 km - 10 km (Fig. 22C). The obtained crystallization conditions for the studied rocks, suggest that amphiboles were crystallized in the supra-solidus stage, when a liquid fraction was still available in the magmas (Johannes & Holtz, 1996), allowing to continuing magma rise and differentiation until the complete solidification of the plutons at upper crustal levels of the Western Cordillera.

The final emplacement of the Danubio and Tatamá plutons occurred at upper crustal levels within the Cretaceous and Paleogene clastic successions of the Western Cordillera, which is evident with the presence of hornblende-hornfels to albite-epidote hornfels facies in the Cretaceous sedimentary rocks (González, 2002) and the presence of quartz veins and dykes within the host Paleogene sedimentary rocks (Rodríguez & Zapata, 2006).

5.3 Tectonic implications

Paleogeographic reconstructions of the Northern Andes and the Pacific Ocean have suggested that during the Early Miocene, the Farallon Plate began to break to form various spreading ridges, resulting in the formation of the Nazca and Cocos oceanic plates (Lonsdale, 2005; Montes et al., 2019). Since then, the remnants of the Farallon Plate and the new Nazca Plate began its approach and subduction history under the northwestern South American margin (Fig. 22B; Lonsdale, 2005; McGirr et al., 2020).

The Early Miocene reorganization of the oceanic plates resulted in a frontal and fast convergence between the oceanic and continental plates in NW South America (González et al., 2023; Lonsdale, 2015; Somoza & Ghidella, 2005), facilitating the subduction reinitiation and thus the Early Miocene magmatic activity along the Western Cordillera of the Colombian Andes (Fig. 22B). The older magmatic crystallization ages obtained in zircons from the northern segment of the Lower Miocene magmatic arc developed in the South American margin together with those available for the southernmost segment (Echeverri et al., 2015; Leal-Mejía et al., 2019; Fig. 1B), suggest that magmatism restarted between 23 Ma and 21 Ma after a magmatic gap of ~9 Ma - 11 Ma.

The Early Miocene plutons in NW South America margin are characterized by a limited surface expression and the apparent absence of an associated volcanic record (Gómez & Montes, 2020). The Miocene detrital record documented on both sides of the Western Cordillera, in the Cauca River Valley basin and the southwesternmost fore-arc basin (Echeverri et al., 2005; Zapata et al., 2023), shows a low proportion of Lower Miocene zircons (23 Ma to 15 Ma), which could be related to this magmatic event. Normally the ratio of volcanic versus plutonic products volume is highly variable in magmatic arcs, ranging between 1:2 and 1:20 (Ducea et al., 2015; Paterson et al., 2011). Therefore, although the Early Miocene volcanic record may have been eroded, the poor contribution in the Miocene detrital record and the size of the associated plutons suggest limited magmatic productivity. The limited melting of subducted sediments in the mantle wedge, as suggested by the geochemistry of the most primitive rocks, may be related to the early stages of subduction, during which the thermal regime of the subduction zone was likely cold. The cold subduction zone did not facilitate the melting of subducted sediments or high magmatic productivity (Zheng, 2019).

The presence of continental crust in the lower and middle crustal levels of the Western Cordillera (Fig. 22A), as suggested by the isotopic constraints in Tatamá, Piedrancha and El Vergel plutons, may be related to the complex architecture of a collisional orogen (Díez Fernández et al., 2021), in which the suture zone between blocks is not a sharp limit but rather a mix between the continental and the oceanic crust.

The strong mantle-derived signature in the Lower Miocene plutons can be related to an input of that asthenospheric material into the mantle wedge facilitated by a steep to normal subduction angle (e.g. Stern, 2011, 2002). This high subduction angle could be associated with the subduction of the older Farallon Plate (Fig. 22A-B), which had an age > 50 Ma at the time of subduction (Lonsdale, 2005; McGirr et al., 2020). The influence of the younger Nazca Plate in the subduction interface below the northern Andean margin began later, after 8 Ma (McGirr et al., 2020).

The arc front defined by the Lower Miocene plutons in the Western Cordillera is currently located at ~150 km from the trench (Fig. 1A), meanwhile, the younger and broader Upper Miocene and Quaternary magmatic front is at ~225 km from the trench in the Cauca Valley and the Central Cordillera (Fig. 1A; Borrero et al., 2009, 2008; Jaramillo et al., 2019; Toro

Toro et al., 2010; Wagner et al., 2017). We suggest that this inland migration of the arc front can be related to the arrival of the younger and more buoyant Nazca Plate, which due to its thermal stage caused the reductions of the subduction angle (Perrin et al., 2018)
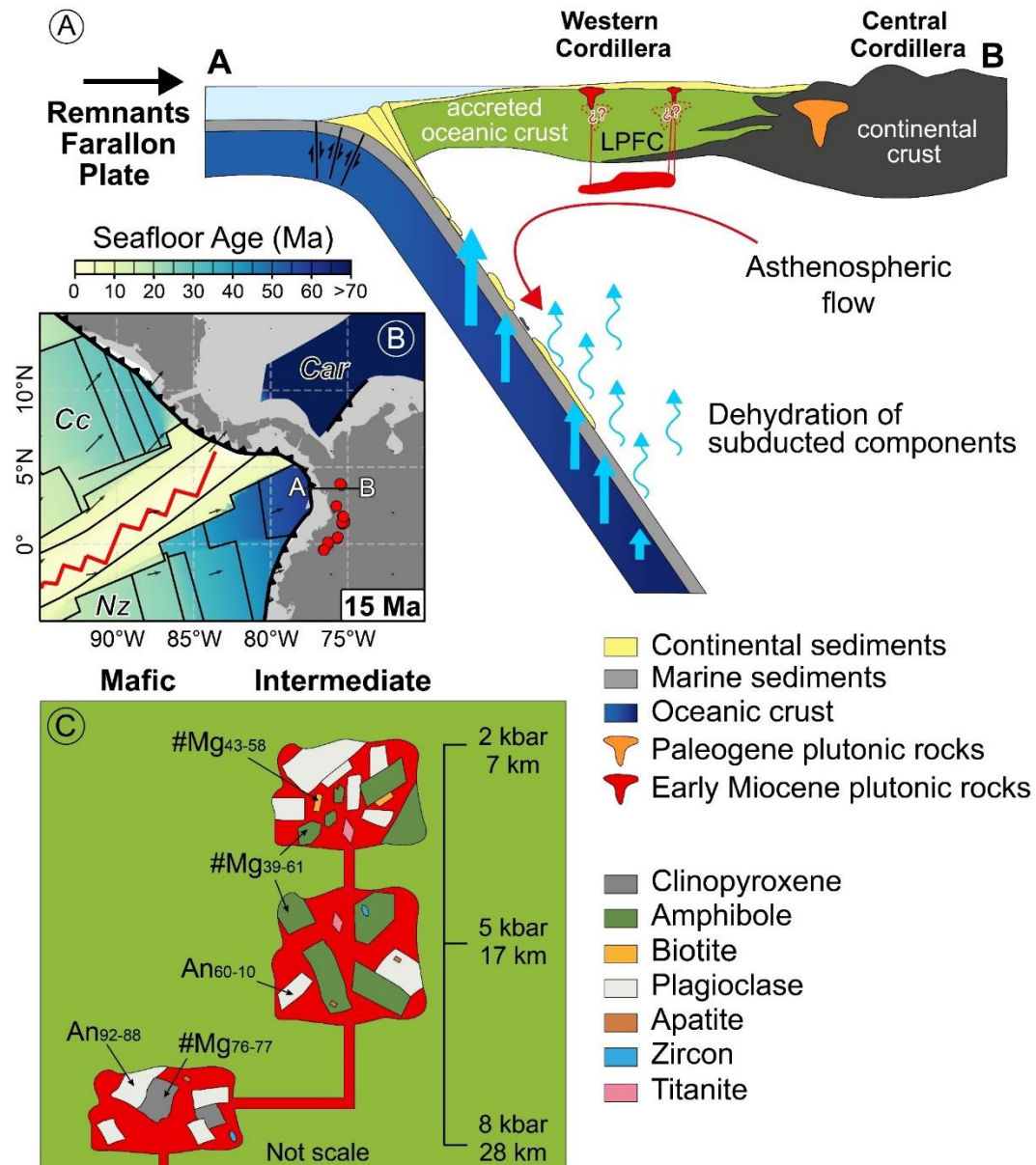
Figure 22. A. Schematic representation of the magma genesis and subduction configuration during the initial stage of Neogene tectonic reorganization. B. The paleogeographic model of the northern Pacific margin at 15 Ma according to the tectonic features, a rotation model, and seafloor ages proposed by Muller et al. (2019). This model

shows the seafloor ages and magmatic events from 15 to 24 Ma in Colombia and was built using the PyGPlates and GPlately Python libraries (Mather et al., 2023). C. Simplified sketch showing the poly-baric crystallization of the mafic and intermediate rocks from the analyzed plutons. Abbreviations: Car: Caribbean Plate; Cc: Cocos Plate; Nz: Nazca Plate; LPCF: Low pressure fractional crystallization; An: Anorthite content; #Mg: magnesium number.

6.Conclusions

The record of the northern segment of the Lower Miocene South American continetal arc is represented by several plutons with ages between 21.9 Ma and 15.6 Ma. The rocks are mostly made up of granodiorites and tonalites, with minor amounts of hornblendites, diorites, and gabbros intruding Cretaceous to Paleogene volcanic and sedimentary rocks of the Western Cordillera of Colombia. This plutonism provides clear evidence of an asthenospheric mantle source that was melted under hydrated and oxidized conditions, which are mainly associated with the dehydration of the subducting oceanic lithosphere. Subsequently, this magma underwent fractional crystallization and mixing processes, as well as probably low continental crust assimilation, until it became compositionally diversified.

Compositional diversification in the Danubio, Pance, and Tatamá plutons was controlled by poly-baric fractional crystallization processes that occurred in equilibrium with low-pressure mineral assemblages within a crustal thickness ranging between 28 km and 38 km.

The petrogenetic history of Lower Miocene plutonism suggests that between 23 Ma and 21 Ma, during the early stages of subduction reorganization along the Colombian margin, the elder Farallon Plate subducted with a normal to steep angle until at least 16.4 Ma, facilitating the influx of asthenospheric material into the mantle wedge. The low magmatic production during the Early Miocene could be associated with a cold subduction zone during the early stages of subduction. The contamination of the magma with continental crust reinforced the complex architecture of a collisional orogen. Continuous subduction in the Miocene brought the newly formed Nazca plate to the margin, causing major changes in the spatial distribution of the frontal arc in the Colombian Andes.

Supplementary Material

Supplementary Table 1. Petrography

Supplementary Table 2. Zircon U-Pb geochronology

Supplementary Table 3. Whole rock major and trace elements

Supplementary Table 4. Zircon chemistry and Hf isotopes

Supplementary Table 5. Mineral chemistry

Supplementary material can be viewed **here.**

References

Alexander, E., & Harrison, M. (2019, December). Do La/Yb and Sr/Y always reflect crustal thickness in magmatic rocks?. In *AGU Fall Meeting Abstracts* (Vol. 2019, pp. V34B-03).

Anderson, A. T. (1976). Magma mixing: petrological process and volcanological tool. *Journal of Volcanology and Geothermal Research*, 1(1), 3–33. https://doi.org/10.1016/0377-0273(76)90016-0

Anderson, J. L., Barth, A. P., Wooden, J. L., & Mazdab, F. (2008). Thermometers and thermobarometers in granitic systems. *Reviews in Mineralogy and Geochemistry*, 69(1), 121–142. https://doi.org/10.2138/rmg.2008.69.4

Annen, C., Blundy, J. D., & Sparks, R. S. J. (2006). The genesis of intermediate and silicic magmas in deep crustal hot zones. *Journal of Petrology*, 47(3), 505–539. https://doi.org/10.1093/petrology/egi084

Annen, Catherine, Blundy, J. D., Leuthold, J., & Sparks, R. S. J. (2015). Construction and evolution of igneous bodies: Towards an integrated perspective of crustal magmatism. *Lithos*, 230, 206–221. https://doi.org/10.1016/j.lithos.2015.05.008

Arculus, R. J. (1994). Aspects of magma genesis in arcs. *Lithos*, 33(1–3), 189–208. https://doi.org/10.1016/0024-4937(94)90060-4

Aspden, J. A., McCOURT, W. J., & Brook, M. (1987). Geometrical control of subduction-related magmatism: the Mesozoic and Cenozoic plutonic history of Western Colombia. *Journal of the Geological Society*, 144(6), 893–905. https://doi.org/10.1144/gsjgs.144.6.0893

Baliani, I., Otamendi, J. E., Tibaldi, A. M., & Cristofolini, E. A. (2012). Geology and Petrology of mafic-ultramafic body from Las Juntas, Valle Fértil, San Juan. Revista de la *Asociación Geológica de Argentina*, 69 (1), 72-87

Barbosa-Espitia, A. A. (2020). The accretion of the Panamá Arc to the northern Andes: Geographic extension, magmatic and exhumation response of the continental margin [Doctoral dissertation, University of Florida]

Barbosa-Espitia, Á. A., Kamenov, G. D., Foster, D. A., Restrepo-Moreno, S. A., & Pardo-Trujillo, A. (2019). Contemporaneous Paleogene arc-magmatism within continental and accreted oceanic arc complexes in the northwestern Andes and Panama. *Lithos*, 348–349(105185), 105185. https://doi.org/10.1016/j.lithos.2019.105185

Barckhausen, U., Ranero, C. R., Cande, S. C., Engels, M., & Weinrebe, W. (2008). Birth of an intraoceanic spreading center. *Geology*, 36(10), 767. https://doi.org/10.1130/g25056a.1

Barth, A. P., Wooden, J. L., Jacobson, C. E., & Economos, R. C. (2013). Detrital zircon as a proxy for tracking the magmatic arc system: The California arc example. *Geology*, 41(2), 223–226. https://doi.org/10.1130/g33619.1

Bayona, G., Bustamante, C., Nova, G. & Salazar–Franco, A.M. (2020). Jurassic evolution of the northwestern corner of Gondwana: Present knowledge and future challenges in studying Colombian Jurassic rocks. In: Gómez, J. & Pinilla–Pachon, A.O. (editors), *The Geology of Colombia, Volume 2 Mesozoic*. Servicio Geológico Colombiano, Publicaciones Geológicas Especiales 36, 171–207. https://doi.org/10.32685/pub.esp.36.2019.05

Bayona, G., Cardona, A., Jaramillo, C., Mora, A., Montes, C., Valencia, V., Ayala, C., Montenegro, O., & Ibañez-Mejia, M. (2012). Early Paleogene magmatism in the northern Andes: Insights on the effects of Oceanic Plateau–continent convergence. *Earth and Planetary Science Letters*, 331–332, 97–111. https://doi.org/10.1016/j.epsl.2012.03.015

Bell, E. A., & Kirkpatrick, H. M. (2021). Effects of crustal assimilation and magma mixing on zircon trace element relationships across the Peninsular Ranges Batholith. Chemical *Geology*, 586(120616), 120616. https://doi.org/10.1016/j.chemgeo.2021.120616

Bernet, M & Garver, J., (2005). Fission-track analysis of detrital zircon. *Reviews in Mineralogy and Geochemistry,* 58(1), 205–237. https://doi.org/10.2138/rmg.2005.58.8

Bernet, M. (2009). A field-based estimate of the zircon fission-track closure temperature. Chemical *Geology*, 259(3–4), 181–189. https://doi.org/10.1016/j.chemgeo.2008.10.043

Bissig, T., Leal-Mejía, H., Stevens, R. B., & Hart, C. J. R. (2017). High Sr/Y magma petrogenesis and the link to porphyry mineralization as revealed by garnet-bearing I-type granodiorite porphyries of the middle Cauca Au-cu belt, Colombia. *Economic Geology and the Bulletin of the Society of Economic Geologists*, 112(3), 551–568. https://doi.org/10.2113/econgeo.112.3.551

Borrero, C., Toro, L. M., Alvarán, M., & Castillo, H. (2009). Geochemistry and tectonic controls of the effusive activity related with the ancestral Nevado del Ruiz volcano, Colombia. *Geofisica Internacional*, 48(1), 149–169.

Borrero, C., Rosero, J. S., Valencia, J. D., & Pardo, A. (2008). La secuencia volcaniclástica de Aranzazu: Registro del impacto del volcanismo en un sistema fluvial Neógeno en la parte media de la Cordillera Central, Colombia. *Boletín de Geología*, 30, 61-77.

Borrero, Carlos, & Toro Toro, L. M. (2016). Vulcanismo de afinidad adaquítica en el Miembro Inferior de la Formación Combia (Mioceno Tardío) al sur de la subcuenca de Amagá, noroccidente de Colombia. *Boletín de Geología*, 38(1), 87–100. https://doi.org/10.18273/revbol.v38n1-2016005

Botero-Garcia, M., Vinasco, C. J., Restrepo-Moreno, S. A., Foster, D. A., & Kamenov, G. D. (2023). Caribbean–South America interactions since the Late Cretaceous: Insights from zircon U–Pb and Lu–Hf isotopic data in sedimentary sequences of the northwestern Andes. *Journal of South American Earth Sciences*, 123(104231), 104231. https://doi.org/10.1016/j.jsames.2023.104231

Bourgois, J., Azema, J., Tournon, J. E. A. N., Bellon, H., Calle, B., Parra, E., ... & Origlia, I. (1982). Ages et structures des complexes basiques et ultrabasiques de la facade pacifique entre 3 degrees N et 12 degrees N (Colombie, Panama et Costa Rica). *Bulletin de la Société géologique de France*, 7(3), 545-554.

Bouvier, A., Vervoort, J. D., & Patchett, P. J. (2008). The Lu–Hf and Sm–Nd isotopic composition of CHUR: Constraints from unequilibrated chondrites and implications for the bulk composition of terrestrial planets. *Earth and Planetary Science Letters*, 273(1–2), 48–57. https://doi.org/10.1016/j.epsl.2008.06.010

Brandon, M. T., Roden-Tice, M. K., & Garver, J. I. (1998). Late Cenozoic exhumation of the Cascadia accretionary wedge in the Olympic Mountains, northwest Washington State. *Geological Society of America Bulletin*, 110(8), 985–1009. https://doi.org/10.1130/0016- 7606(1998)110<0985:lceotc>2.3.co;2

Brenan, J. M., Shaw, H. F., Ryerson, F. J., & Phinney, D. L. (1995). Mineral-aqueous fluid partitioning of trace elements at 900°C and 2.0 GPa: Constraints on the trace

element chemistry of mantle and deep crustal fluids. *Geochimica et Cosmochimica Acta*, 59(16), 3331–3350. https://doi.org/10.1016/0016-7037(95)00215-l

Brounce, M., Kelley, K. A., Cottrell, E., & Reagan, M. K. (2015). Temporal evolution of mantle wedge oxygen fugacity during subduction initiation. *Geology*, 43(9), 775–778. https://doi.org/10.1130/g36742.1

Brügmann, G. E., Reischmann, T., Naldrett, A. J., and Sutcliffe, R. H. (1997). Roots of an Archean volcanic arc complex: the Lac des Iles area in Ontario, Canada. Precambrian Res. 81, 223–239. doi:10.1016/S0301-9268(96)00036-8

Buchs, D. M., Baumgartner, P. O., Baumgartner-Mora, C., Flores, K., & Bandini, A. N. (2011). Upper Cretaceous to Miocene tectonostratigraphy of the Azuero area (Panama) and the discontinuous accretion and subduction erosion along the Middle American margin. *Tectonophysics*, 512(1–4), 31–46. https://doi.org/10.1016/j.tecto.2011.09.010

Buchs, D. M., Coombs, H., Irving, D., Wang, J., Koppers, A., Miranda, R., Coronado, M., Tapia, A., & Pitchford, S. (2019). Volcanic shutdown of the Panama Canal area following breakup of the Farallon plate. *Lithos,* 334–335, 190–204. https://doi.org/10.1016/j.lithos.2019.02.016

Bustamante, C. & Bustamante, A. (2019). Two Cretaceous subduction events in the Central Cordillera: Insights from the high P–low T metamorphism. In: Gómez, J. & Pinilla–Pachon, A.O. (editors), The Geology of Colombia, Volume 2 Mesozoic. Servicio Geológico Colombiano, *Publicaciones Geológicas Especiales* 36, 485–498. https://doi.org/10.32685/pub.esp.36.2019.14

Bustamante, C., Cardona, A., Archanjo, C. J., Bayona, G., Lara, M., & Valencia, V. (2017). Geochemistry and isotopic signatures of Paleogene plutonic and detrital rocks of the Northern Andes of Colombia: A record of post-collisional arc magmatism. *Lithos*, 277, 199–209. https://doi.org/10.1016/j.lithos.2016.11.025

Bustos Rodríguez, H., Oyola, L. D., Rojas, Y., Alcázar, G. A. P., Balogh, A. G., & Cabri, L. J. (2011). Quantification of refractory gold in grains of pyrite and arsenopyrite from the" El Diamante" gold mine in Nariño-Colombia. Tumbaga, 1(6), 153-164

Bustos Rodriguez, H., Oyola Lozano, D., Rojas Martínez, Y. A., Pérez Alcázar, G. A., Flege, S., Balogh, A. G., Cabri, L. J., & Tubrett, M. (2008). Mineralogical analysis of auriferous ores from the El Diamante mine, Colombia. Hyperfine Interactions, 175(1–3). https://doi.org/10.1007/s10751-008-9603-2

Cao, W., Kaus, B. J. P., & Paterson, S. (2016). Intrusion of granitic magma into the continental crust facilitated by magma pulsing and dike-diapir interactions: Numerical simulations. *Tectonics*, 35(6), 1575–1594. https://doi.org/10.1002/2015tc004076

Cardona, A., León, S., Jaramillo, J.S., Valencia, V., Zapata, S., Pardo–Trujillo, A., Schmitt, A.K., Mejía, D. & Arenas, J.C. (2020). Cretaceous record from a Mariana– to an Andean–type margin in the Central Cordillera of the Colombian Andes. In: Gómez, J. & Pinilla–Pachon, A.O. (editors), *The Geology of Colombia, Volume 2 Mesozoic*. Servicio Geológico Colombiano, Publicaciones Geológicas Especiales 36, 335–373. https://doi.org/10.32685/pub.esp.36.2019.10

Cardona, A., León, S., Jaramillo, J. S., Montes, C., Valencia, V., Vanegas, J., Bustamante, C., & Echeverri, S. (2018). The Paleogene arcs of the northern Andes of Colombia and Panama: Insights on plate kinematic implications from new and existing geochemical, geochronological and isotopic data. *Tectonophysics*, 749, 88–103. https://doi.org/10.1016/j.tecto.2018.10.032

Castro, Antonio. (2014). The off-crust origin of granite batholiths. *Geoscience Frontiers*, 5(1), 63–75. https://doi.org/10.1016/j.gsf.2013.06.006

Castro, A., Gerya, T., Garcia-Casco, A., Fernandez, C., Diaz-Alvarado, J., Moreno-Ventas, I., & Low, I. (2010). Melting relations of MORB-sediment melanges in underplated mantle wedge plumes; Implications for the origin of cordilleran-type batholiths. *Journal of Petrology*, 51(6), 1267–1295. https://doi.org/10.1093/petrology/egq019

Castro, A., Rodriguez, C., Fernández, C., Aragón, E., Pereira, M. F., & Molina, J. F. (2021). Secular variations of magma source compositions in the North Patagonian batholith from the Jurassic to Tertiary: Was mélange melting involved? *Geosphere,* 17(3), 766–785. https://doi.org/10.1130/ges02338.1

Chang, Z., Vervoort, J. D., McClelland, W. C., & Knaack, C. (2006). U-Pb dating of zircon by LA-ICP-MS. *Geochemistry, Geophysics, Geosystems*: *G(3)*, 7(5). https://doi.org/10.1029/2005gc001100

Chappell, Bruce W., & Wyborn, D. (2004). Cumulate and cumulative granites and associated rocks. *Resource Geology*, 54(3), 227–240. https://doi.org/10.1111/j.1751-3928.2004.tb00204.x

Chauvel, C., Marini, J. C., Plank, T., & Ludden, J. N. (2009). Hf-Nd input flux in the Izu-Mariana subduction zone and recycling of subducted material in the mantle. *Geochemistry, Geophysics, Geosystems*, 10(1).

Chayes, F. (1956). *Petrographic modal analysis.* John Wiley and Sons, New York.

Claiborne, L. L., Miller, C. F., & Wooden, J. L. (2010). Trace element composition of igneous zircon: a thermal and compositional record of the accumulation and evolution of a large silicic batholith, Spirit Mountain, Nevada. *Contributions to Mineralogy and Petrology*, 160(4), 511–531. https://doi.org/10.1007/s00410-010-0491-5

Class, C., Miller, D. M., Goldstein, S. L., & Langmuir, C. H. (2000). Distinguishing melt and fluid subduction components in Umnak Volcanics, Aleutian Arc. *Geochemistry, Geophysics, Geosystems: G(3),* 1(6). https://doi.org/10.1029/1999gc000010

Cochrane, R., Spikings, R., Gerdes, A., Ulianov, A., Mora, A., Villagómez, D., Putlitz, B., & Chiaradia, M. (2014). Permo-Triassic anatexis, continental rifting and the disassembly of western Pangaea. *Lithos,* 190–191, 383–402. https://doi.org/10.1016/j.lithos.2013.12.020

Copley, A., Weller, O., & Bain, H. (2023). Diapirs of crystal-rich slurry explain granite emplacement temperature and duration. *Scientific Reports*, 13(1), 1–11. https://doi.org/10.1038/s41598-023-40805-2

Corfu, F. (2003). Atlas of zircon textures. *Reviews in Mineralogy and Geochemistry*, 53(1), 469–500. https://doi.org/10.2113/0530469

Deer, W. A., Howie, R. A., & Zussman, J. (2013). An introduction to the Rock-forming minerals. *Mineralogical Society of Great Britain and Ireland*.

Defant, M. J., & Drummond, M. S. (1990). Derivation of some modern arc magmas by melting of young subducted lithosphere. *Nature*, 347(6294), 662–665. https://doi.org/10.1038/347662a0

Dickin, A. P. (2018). *Radiogenic isotope geology*. Cambridge university press

Ducea, M. N., Saleeby, J. B., & Bergantz, G. (2015). The architecture, chemistry, and evolution of continental magmatic arcs. *Annual Review of Earth and Planetary Sciences*, 43(1), 299–331. https://doi.org/10.1146/annurev-earth-060614-105049

Duque-Caro, H. (1990). The choco block in the northwestern corner of South America: Structural, tectonostratigraphic, and paleogeographic implications. Journal of South *American Earth Sciences*, 3(1), 71–84. https://doi.org/10.1016/0895-9811(90)90019-w

Echeverri, S., Cardona, A., Pardo, A., Monsalve, G., Valencia, V. A., Borrero, C., ... & López, S. (2015). Regional provenance from southwestern Colombia fore-arc and

intra-arc basins: implications for Middle to Late Miocene orogeny in the Northern Andes. *Terra Nova*, 27(5), 356-363.

Elliott, T., Plank, T., Zindler, A., White, W., & Bourdon, B. (1997). Element transport from slab to volcanic front at the Mariana arc. *Journal of Geophysical Research*, 102(B7), 14991–15019. https://doi.org/10.1029/97jb00788

Erdmann, S., Martel, C., Pichavant, M., & Kushnir, A. (2014). Amphibole as an archivist of magmatic crystallization conditions: problems, potential, and implications for inferring magma storage prior to the paroxysmal 2010 eruption of Mount Merapi, Indonesia. *Contributions to Mineralogy and Petrology*, 167(6). https://doi.org/10.1007/s00410-014-1016-4

Evans, K. A., & Frost, B. R. (2021). Deserpentinization in subduction zones as a source of oxidation in arcs: A reality check. *Journal of Petrology*, 62(3). https://doi.org/10.1093/petrology/egab016

Evans, K. A. (2012). The redox budget of subduction zones. *Earth-Science Reviews*, 113(1–2), 11–32. https://doi.org/10.1016/j.earscirev.2012.03.003

Evans, K.-A., & Tomkins, A.-G. (2011). The relationship between subduction zone redox budget and arc magma fertility. *Earth and Planetary Science Letters*, 308(3–4), 401–409. https://doi.org/10.1016/j.epsl.2011.06.009

Farina, F., Stevens, G., Gerdes, A., & Frei, D. (2014). Small-scale Hf isotopic variability in the Peninsula pluton (South Africa): the processes that control inheritance of source 176Hf/177Hf diversity in S-type granites. *Contributions to Mineralogy and Petrology*, 168(4). https://doi.org/10.1007/s00410-014-1065-8

Farris, D. W., Jaramillo, C., Bayona, G., Restrepo-Moreno, S. A., Montes, C., Cardona, A., Mora, A., Speakman, R. J., Glascock, M. D., & Valencia, V. (2011). Fracturing of the Panamanian Isthmus during initial collision with South America. *Geology*, 39(11), 1007–1010. https://doi.org/10.1130/g32237.1

Ferry, J. M., & Watson, E. B. (2007). New thermodynamic models and revised calibrations for the Ti-in-zircon and Zr-in-rutile thermometers. *Contributions to Mineralogy and Petrology,* 154(4), 429–437. https://doi.org/10.1007/s00410-007-0201-0

Fisher, C. M., Vervoort, J. D., & DuFrane, S. A. (2014). Accurate Hf isotope determinations of complex zircons using the "laser ablation split stream" method. *Geochemistry, Geophysics, Geosystems: G(3),* 15(1), 121–139. https://doi.org/10.1002/2013gc004962

Gehrels, G. (2011). *Detrital zircon U-Pb geochronology: Current methods and new opportunities.* In Tectonics of Sedimentary Basins (pp. 45–62). Wiley. https://doi.org/10.1002/9781444347166.ch2

Gehrels, G. E., Valencia, V. A., & Ruiz, J. (2008). Enhanced precision, accuracy, efficiency, and spatial resolution of U-Pb ages by laser ablation–multicollector–inductively coupled plasma–mass spectrometry. *Geochemistry, Geophysics, Geosystems: G(3),* 9(3), 1–13. https://doi.org/10.1029/2007gc001805

Geldmacher, J., Hanan, B. B., Blichert-Toft, J., Harpp, K., Hoernle, K., Hauff, F., Werner, R., & Kerr, A. C. (2003). Hafnium isotopic variations in volcanic rocks from the Caribbean Large Igneous Province and Galápagos hot spot tracks. *Geochemistry, Geophysics, Geosystems: G(3)*, 4(7). https://doi.org/10.1029/2002gc000477

George, S. W. M., Horton, B. K., Vallejo, C., Jackson, L. J., & Gutierrez, E. G. (2021). Did accretion of the Caribbean oceanic plateau drive rapid crustal thickening in the northern Andes? *Geology*, 49 (8), 936-940. https://doi.org/10.1130/g48509.1

Gill, R. (2022). *Igneous rocks and processes: a practical guide.* John Wiley & Sons.

Gill, J. B. (2012). *Orogenic andesites and plate tectonics.* Springer Science & Business Media.

Gómez, J. & Montes, N.E. (2020). Mapa Geológico de Colombia en Relieve 2020. Escala 1:1 000 000. Servicio Geológico Colombiano. Bogotá

González, R., Oncken, O., Faccenna, C., Le Breton, E., Bezada, M., & Mora, A. (2023). Kinematics and convergent tectonics of the northwestern south American plate during the Cenozoic. *Geochemistry, Geophysics, Geosystems: G(3)*, 24(7), 1–32. https://doi.org/10.1029/2022gc010827

González, H. (2002). Catálogo de las unidades litoestratigráficas de Colombia, Tonalita de Tatamá (N1tt), Cordillera Occidental. *Ingeominas,* 1-15.

Grocke, S. B., Cottrell, E., de Silva, S., & Kelley, K. A. (2016). The role of crustal and eruptive processes versus source variations in controlling the oxidation state of iron in Central Andean magmas. *Earth and Planetary Science Letters*, 440, 92–104. https://doi.org/10.1016/j.epsl.2016.01.026

Grove, T., Parman, S., Bowring, S., Price, R., and Baker, M., 2002, The role of an H2O-rich fluid component in the generation of primitive basaltic andesites and andesites from the Mt. Shasta region, N California: *Contributions to Mineralogy and Petrology*, 142, (4), p. 375–396, https://doi.org/10.1007/s004100100299.

Guo, M., & Korenaga, J. (2023). The combined Hf and Nd isotope evolution of the depleted mantle requires Hadean continental formation. *Science Advances*, 9(12). https://doi.org/10.1126/sciadv.ade2711

Hacker, B. R. (2008). H2O subduction beyond arcs. *Geochemistry, Geophysics, Geosystems: G(3),* 9(3). https://doi.org/10.1029/2007gc001707

Hao, L.-L., Wang, Q., Kerr, A. C., Huang, F., Xiao, M., Ma, X.-L., Zhang, W.-F., Wang, W.-Y., & Liu, M.-R. (2024). Andesitic arc magmas derived from two contrasting mélange origins: Evidence from central Tibetan dioritic porphyries. *Chemical Geology*, 121920, 121920. https://doi.org/10.1016/j.chemgeo.2023.121920

Harrison, T. M., & Watson, E. B. (1984). The behavior of apatite during crustal anatexis: Equilibrium and kinetic considerations. *Geochimica et Cosmochimica Acta*, 48(7), 1467–1477. https://doi.org/10.1016/0016-7037(84)90403-4

Hawthorne, F. C., Oberti, R., Harlow, G. E., Maresch, W. V., Martin, R. F., Schumacher, J. C., & Welch, M. D. (2012). Nomenclature of the amphibole supergroup. The *American Mineralogist*, 97(11–12), 2031–2048. https://doi.org/10.2138/am.2012.4276

Hayden, L. A., & Watson, E. B. (2007). Rutile saturation in hydrous siliceous melts and its bearing on Ti-thermometry of quartz and zircon. *Earth and Planetary Science Letters,* 258(3–4), 561–568. https://doi.org/10.1016/j.epsl.2007.04.020

Hildreth, W., & Moorbath, S. (1988). Crustal contributions to arc magmatism in the Andes of Central Chile. *Contributions to mineralogy and petrology,* 98, 455-489.

Hincapié-Gómez, S., Cardona, A., Jiménez, G., Monsalve, G., Ramírez-Hoyos, L., & Bayona, G. (2018). Paleomagnetic and gravimetrical reconnaissance of Cretaceous volcanic rocks from the Western Colombian Andes: paleogeographic connections with the Caribbean Plate. *Studia Geophysica et Geodaetica*, 62(3), 485–511. https://doi.org/10.1007/s11200-016-0678-y

Holland, T., & Blundy, J. (1994). Non-ideal interactions in calcic amphiboles and their bearing on amphibole-plagioclase thermometry. *Contributions to Mineralogy and Petrology*, 116(4), 433–447. https://doi.org/10.1007/bf00310910

Hoskin, P. W. O. (2003). The composition of zircon and igneous and metamorphic petrogenesis. *Reviews in Mineralogy and Geochemistry*, 53(1), 27–62. https://doi.org/10.2113/0530027

Humphreys, M. C. S., Brooker, R. A., Fraser, D. G., Burgisser, A., Mangan, M. T., & McCammon, C. (2015). Coupled interactions between volatile activity and Fe oxidation state during arc crustal processes. *Journal of Petrology*, 56(4), 795–814. https://doi.org/10.1093/petrology/egv017

Iizuka, T., Yamaguchi, T., Itano, K., Hibiya, Y., & Suzuki, K. (2017). What Hf isotopes in zircon tell us about crust–mantle evolution. *Lithos*, 274–275, 304–327. https://doi.org/10.1016/j.lithos.2017.01.006

Ishihara, S. (1977). The magnetite-series and ilmenite-series granitic rocks. *Mining geology*, 27(145), 293-305.

Jaramillo, J. S., Cardona, A., Monsalve, G., Valencia, V., & León, S. (2019). Petrogenesis of the late Miocene Combia volcanic complex, northwestern Colombian Andes: Tectonic implication of short term and compositionally heterogeneous arc magmatism. *Lithos*, 330–331, 194–210. https://doi.org/10.1016/j.lithos.2019.02.017

Jaramillo, Juan S., Zapata, S., Carvalho, M., Cardona, A., Jaramillo, C., Crowley, J. L., Bayona, G., & Caballero-Rodriguez, D. (2022). Diverse magmatic evolutionary trends of the Northern Andes unraveled by Paleocene to early Eocene detrital zircon geochemistry. *Geochemistry, Geophysics, Geosystems*, 23(9). https://doi.org/10.1029/2021gc010113

Janousek, V., Farrow, C., Erban, V., & Moyen, J. F. (2022). *Geochemical Data Toolkit for Windows*. Available on http://www. gla. ac. uk/gcdkit, 188.

Johannes, W., & Holtz, F. (1996). *Petrogenesis and experimental petrology of granitic rocks*. Springer Berlin Heidelberg.

Kay, S. M., Mpodozis, C., Ramos, V. A., & Munizaga, F. (1991). Magma source variations for mid–late Tertiary magmatic rocks associated with a shallowing subduction zone and a thickening crust in the central Andes (28 to 33°S). In Andean Magmatism and Its Tectonic Setting (pp. 113–138). *Geological Society of America*. https://doi.org/10.1130/spe265-p113

Kelemen, P. B., Rilling, J. L., Parmentier, E. M., Mehl, L., & Hacker, B. R. (2003). Thermal structure due to solid-state flow in the mantle wedge beneath arcs. In Inside the Subduction Factory. *American Geophysical Union*. 293–311

Kemp, A. I. S., Hawkesworth, C. J., Foster, G. L., Paterson, B. A., Woodhead, J. D., Hergt, J. M., Gray, C. M., & Whitehouse, M. J. (2007). Magmatic and crustal differentiation history of granitic rocks from Hf-O isotopes in zircon. *Science* (New York, N.Y.), 315(5814), 980–983. https://doi.org/10.1126/science.1136154

Kerr, A. C., Marriner, G. F., Tarney, J., Nivia, A., Saunders, A. D., Thirlwall, M. F., & Sinton, C. W. (1997). Cretaceous basaltic terranes in Western Colombia: Elemental, chronological and Sr-Nd isotopic constraints on petrogenesis. *Journal of Petrology*, 38(6), 677–702. https:// doi.org/10.1093/petroj/38.6.677

Kessel, R., Schmidt, M. W., Ulmer, P., & Pettke, T. (2005). Trace element signature of subduction-zone fluids, melts and supercritical liquids at 120–180 km depth. *Nature,* 437(7059), 724–727. https://doi.org/10.1038/nature03971

Kirkland, C. L., Smithies, R. H., Taylor, R. J. M., Evans, N., & McDonald, B. (2015). Zircon Th/U ratios in magmatic environs. *Lithos*, 212–215, 397–414. https://doi.org/10.1016/j.lithos.2014.11.021

Klein, E. M., & Langmuir, C. H. (1987). Global correlations of ocean ridge basalt chemistry with axial depth and crustal thickness. *Journal of Geophysical Research*, 92(B8), 8089–8115. https://doi.org/10.1029/jb092ib08p08089

Langmuir, C. H., Klein, E. M., & Plank, T. (1992). Petrological systematics of mid-ocean ridge basalts: constraints on melt generation beneath ocean ridges. Mantle flow and melt generation at mid-ocean ridges. 71, 183-280.

Leal-Mejía, H., Shaw, R. P., & Melgarejo i Draper, J. C. (2019). Spatial-temporal migration of granitoid magmatism and the Phanerozoic tectono-magmatic evolution of the Colombian Andes. In Geology and Tectonics of Northwestern South America (pp. 253–410). *Springer International Publishing*. https://doi.org/10.1007/978-3-319-76132-9_5

Le Maitre, R. W., Streckeisen, A., Zanettin, B., Le Bas, M. J., Bonin, B., & Bateman, P. (Eds.). (2005). *Igneous rocks: a classification and glossary of terms: recommendations of the International Union of Geological Sciences Subcommission on the Systematics of Igneous Rocks*. Cambridge University Press.

León, S., Cardona, A., Parra, M., Sobel, E. R., Jaramillo, J. S., Glodny, J., Valencia, V. A., Chew, D., Montes, C., Posada, G., Monsalve, G., & Pardo-Trujillo, A. (2018). Transition from collisional to subduction-related regimes: An example from Neogene panama-Nazca-South America interactions. *Tectonics*, 37(1), 119–139. https://doi.org/10.1002/2017tc004785

Liao, Y., Wei, C., & Rehman, H. U. (2021). Titanium in calcium amphibole: Behavior and thermometry. *American Mineralogist*, 106(2), 180–191. https://doi.org/10.2138/am-2020-7409

Litvak, V. D., Fernández Paz, L., Iannelli, S., Poma, S., & Folguera, A. (2019). *Cenozoic arc-related magmatism in the southern Central and North Patagonian Andes*. In Andean Tectonics (pp. 573–607). Elsevier.

Locock, A. J. (2014). An Excel spreadsheet to classify chemical analyses of amphiboles following the IMA 2012 recommendations. *Computers & Geosciences*, 62, 1–11. https://doi.org/10.1016/j.cageo.2013.09.011

Lonsdale, P. (2005). Creation of the Cocos and Nazca plates by fission of the Farallon plate. *Tectonophysics*, 404(3–4), 237–264. https://doi.org/10.1016/j.tecto.2005.05.011

Loucks, R. R., Fiorentini, M. L., & Henríquez, G. J. (2020). New magmatic oxybarometer using trace elements in zircon. *Journal of Petrology*, 61(3), 1–29. https://doi.org/10.1093/petrology/egaa034

Macpherson, C. G., Dreher, S. T., & Thirlwall, M. F. (2006). Adakites without slab melting: High pressure differentiation of island arc magma, Mindanao, the Philippines. *Earth and Planetary Science Letters*, 243(3–4), 581–593. https://doi.org/10.1016/j.epsl.2005.12.034

Manduca, C. A., Silver, L. T., & Taylor, H. P. (1992). 87Sr/86Sr and 18O/16O isotopic systematics and geochemistry of granitoid plutons across a steeply-dipping boundary between contrasting lithospheric blocks in western Idaho. *Contributions to Mineralogy and Petrology*, 109(3), 355–372. https://doi.org/10.1007/bf00283324

Manning, C. (2004). The chemistry of subduction-zone fluids. *Earth and Planetary Science Letters,* 223(1–2), 1–16. https://doi.org/10.1016/j.epsl.2004.04.030

Manning, C. E. (1996). Effect of sediments on aqueous silica transport in subduction zones. *Washington DC American Geophysical Union Geophysical Monograph Series*, 96, 277-284.

Mather, B.R., Müller, R.D., Zahirovic, S., Cannon, J., Chin, M., Ilano, L. et al. (2024) Deep time spatio-temporal data analysis using pyGPlates with PlateTectonicTools and GPlately. *Geoscience Data Journal*, 11, 3–10. Available from: https://doi.org/10.1002/gdj3.185

McCourt, W., Muñoz, U., Villegas, V., (1990). Regional Geology and Gold Potential of the Guapi–Napi Drainage Basin and Upper Timbiqui River. British Geological Survey, Overseas Geology Series. Technical Report WC/90/34Cauca Department, SW Colombia.

McDonough, W. F., & Sun, S.-S. (1995). The composition of the earth. *Chemical Geology*, 120(3–4), 223–253. https://doi.org/10.1016/0009-2541(94)00140-4

McGirr, R., Seton, M., & Williams, S. (2021). Kinematic and geodynamic evolution of the Isthmus of Panama region: Implications for Central American Seaway closure. *Geological Society of America Bulletin,* 133(3–4), 867–884. https://doi.org/10.1130/b35595.1

Meschede, M., & Barckhausen, U. (2001). The relationship of the Cocos and Carnegie ridges: age constraints from paleogeographic reconstructions. *International Journal of Earth Sciences*, 90, 386-392.

Middlemost, E. A. K. (1994). Naming materials in the magma/igneous rock system*. Earth-Science Reviews, 3*7(3–4), 215–224. https://doi.org/10.1016/0012-8252(94)90029-9

Miller, J. S., Matzel, J. E. P., Miller, C. F., Burgess, S. D., & Miller, R. B. (2007). Zircon growth and recycling during the assembly of large, composite arc plutons. *Journal of Volcanology and Geothermal Research,* 167(1–4), 282–299. https://doi.org/10.1016/j.jvolgeores.2007.04.019

Molano, J. C., & Shimazaki, H. (2003). Mineralogía, geoquímica y algunos aspectos genéticos de la mina El Diamante- Nariño (Colombia). *Revista Boletín de Geología*, 25(40), 105–116. https://revistas.uis.edu.co/index.php/revistaboletindegeologia/article/view/3958

Molina, J. F., Moreno, J. A., Castro, A., Rodríguez, C., & Fershtater, G. B. (2015). Calcic amphibole thermobarometry in metamorphic and igneous rocks: New calibrations based on plagioclase/amphibole Al-Si partitioning and amphibole/liquid Mg partitioning. *Lithos,* 232, 286–305. https://doi.org/10.1016/j.lithos.2015.06.027

Montes, C., Cardona, A., Jaramillo, C., Pardo, A., Silva, J. C., Valencia, V., Ayala, C., Pérez-Angel, L. C., Rodriguez-Parra, L. A., Ramirez, V., & Niño, H. (2015). Middle Miocene closure of the Central American Seaway. *Science* (New York, N.Y.), 348(6231), 226–229. https://doi.org/10.1126/science.aaa2815

Montes, C., Rodriguez-Corcho, A. F., Bayona, G., Hoyos, N., Zapata, S., & Cardona, A. (2019). Continental margin response to multiple arc-continent collisions: The northern Andes-Caribbean margin. *Earth-Science Reviews*, 198(102903), 102903. https://doi.org/10.1016/j.earscirev.2019.102903

Mora-Páez, H., Kellogg, J. N., Freymueller, J. T., Mencin, D., Fernandes, R. M. S., Diederix, H., LaFemina, P., Cardona-Piedrahita, L., Lizarazo, S., Peláez-Gaviria, J.-R., Díaz-

Mila, F., Bohórquez-Orozco, O., Giraldo-Londoño, L., & Corchuelo-Cuervo, Y. (2019). Crustal deformation in the northern Andes – A new GPS velocity field. *Journal of South American Earth Sciences*, 89, 76–91. https://doi.org/10.1016/j.jsames.2018.11.002

Moyen, J.-F., Janoušek, V., Laurent, O., Bachmann, O., Jacob, J.-B., Farina, F., Fiannacca, P., & Villaros, A. (2021). Crustal melting vs. fractionation of basaltic magmas: Part 1, granites and paradigms. *Lithos*, 402–403(106291), 106291. https://doi.org/10.1016/j.lithos.2021.106291

Müller, R. D., Zahirovic, S., Williams, S. E., Cannon, J., Seton, M., Bower, D. J., et al. (2019). A global plate model including lithospheric deformation along major rifts and orogens since the Triassic. *Tectonics*, 38(6), 1884–1907. https://doi.org/10.1029/2018tc005462

Müntener, O., Ewing, T., Baumgartner, L. P., Manzini, M., Roux, T., Pellaud, P., & Allemann, L. (2018). Source and fractionation controls on subduction-related plutons and dike swarms in southern Patagonia (Torres del Paine area) and the low Nb/Ta of upper crustal igneous rocks. *Contributions to Mineralogy and Petrology*, 173(5). https://doi.org/10.1007/s00410-018-1467-0

Mutch, E. J. F., Blundy, J. D., Tattitch, B. C., Cooper, F. J., & Brooker, R. A. (2016). An experimental study of amphibole stability in low-pressure granitic magmas and a revised Al-in-hornblende geobarometer. *Contributions to Mineralogy and Petrology*, 171(85), 1–27. https://doi.org/10.1007/s00410-016-1298-9

Nachit, H., Ibhi, A., Abia, E. H., & Ben Ohoud, M. (2005). Discrimination between primary magmatic biotites, reequilibrated biotites and neoformed biotites. Comptes Rendus: *Geoscience*, 337(16), 1415–1420. https://doi.org/10.1016/j.crte.2005.09.002

Navarrete, C., Gianni, G., Tassara, S., Zaffarana, C., Likerman, J., Márquez, M., Wostbrock, J., Planavsky, N., Tardani, D., & Perez Frasette, M. (2024). Massive Jurassic slab break-off revealed by a multidisciplinary reappraisal of the Chon Aike silicic large igneous province. *Earth-Science Reviews*, 249(104651), 104651. https://doi.org/10.1016/j.earscirev.2023.104651

Nebel, O., Vroon, P. Z., van Westrenen, W., Iizuka, T., & Davies, G. R. (2011). The effect of sediment recycling in subduction zones on the Hf isotope character of new arc crust, Banda arc, Indonesia. *Earth and Planetary Science Letters*, 303(3–4), 240–250. https://doi.org/10.1016/j.epsl.2010.12.053

Nivia, A. (2001). Mapa geológico del departamento del Valle del Cauca, Memoria explicativa. *Ingeominas,* 1-148.

Nielsen, S. G., & Marschall, H. R. (2017). Geochemical evidence for mélange melting in global arcs. *Science Advances*, 3(4). https://doi.org/10.1126/sciadv.1602402

Noda, A. (2016). Forearc basins: Types, geometries, and relationships to subduction zone dynamics. *Geological Society of America Bulletin*, 128(5–6), 879–895. https://doi.org/10.1130/b31345.1

Nowell, G. M., Kempton, P. D., Noble, S. R., Fitton, J. G., Saunders, A. D., Mahoney, J. J., & Taylor, R. N. (1998). High precision Hf isotope measurements of MORB and OIB by thermal ionisation mass spectrometry: insights into the depleted mantle. *Chemical Geology*, 149(3–4), 211–233. https://doi.org/10.1016/s0009-2541(98)00036-9

Olierook, H. K. H., Kirkland, C. L., Szilas, K., Hollis, J. A., Gardiner, N. J., Steenfelt, A., Jiang, Q., Yakymchuk, C., Evans, N. J., & McDonald, B. J. (2020). Differentiating between inherited and autocrystic zircon in granitoids. *Journal of Petrology*, 61(8), 1–26. https://doi.org/10.1093/petrology/egaa081

Pardo-Casas, F., & Molnar, P. (1987). Relative motion of the Nazca (Farallon) and South American Plates since Late Cretaceous time. *Tectonics*, 6(3), 233–248. https://doi.org/10.1029/tc006i003p00233

Passchier, C. W., & Trouw, R. A. (2005). *Microtectonics.* Springer Science & Business Media.

Paterson, S. R., Okaya, D., Memeti, V., Economos, R., & Miller, R. B. (2011). Magma addition and flux calculations of incrementally constructed magma chambers in continental margin arcs: Combined field, geochronologic, and thermal modeling studies. *Geosphere*, 7(6), 1439–1468. https://doi.org/10.1130/ges00696.1

Peacock, S. M., & Wang, K. (1999). Seismic consequences of warm versus cool subduction metamorphism: Examples from southwest and northeast Japan. *Science* (New York, N.Y.), 286(5441), 937–939. https://doi.org/10.1126/science.286.5441.937

Peacock, S. M. (2003). Thermal structure and metamorphic evolution of subducting slabs. *Geophysical Monograph-American Geophysical Union*, 138, 7-22.

Pearce, J. A., Stern, R. J., Bloomer, S. H., & Fryer, P. (2005). Geochemical mapping of the Mariana arc-basin system: Implications for the nature and distribution of subduction components. *Geochemistry, geophysics, geosystems*, 6(7).

Pearce, J. A., Harris, N. B. W., & Tindle, A. G. (1984). Trace element discrimination diagrams for the tectonic interpretation of granitic rocks. *Journal of Petrology*, 25(4), 956–983. https://doi.org/10.1093/petrology/25.4.956

Peccerillo, A., & Taylor, S. R. (1976). Geochemistry of eocene calc-alkaline volcanic rocks from the Kastamonu area, Northern Turkey. *Contributions to Mineralogy and Petrology*, 58(1), 63–81. https://doi.org/10.1007/bf00384745

Pitcher, W. S. (1997). *The nature and origin of granite*. Springer Science & Business Media.

Plank, T. (2014). The chemical composition of subducting sediments. In *Treatise on Geochemistry*. Elseiver, 607–629

Plank, Terry, & Langmuir, C. H. (1988). An evaluation of the global variations in the major element chemistry of arc basalts. *Earth and Planetary Science Letters*, 90(4), 349–370. https://doi.org/10.1016/0012-821x(88)90135-5

Profeta, L., Ducea, M. N., Chapman, J. B., Paterson, S. R., Gonzales, S. M. H., Kirsch, M., Petrescu, L., & DeCelles, P. G. (2015). Quantifying crustal thickness over time in magmatic arcs. *Scientific Reports*, 5(1), 1–7. https://doi.org/10.1038/srep17786

Putirka, K. (2016). Amphibole thermometers and barometers for igneous systems and some implications for eruption mechanisms of felsic magmas at arc volcanoes. *The American Mineralogist*, 101(4), 841–858. https://doi.org/10.2138/am-2016-5506

Putirka, K., Johnson, M., Kinzler, R., Longhi, J., & Walker, D. (1996). Thermobarometry of mafic igneous rocks based on clinopyroxene-liquid equilibria, 0-30 kbar. *Contributions to Mineralogy and Petrology*, 123(1), 92–108. https://doi.org/10.1007/s004100050145

Ranero, C. R., Phipps Morgan, J., McIntosh, K., & Reichert, C. (2003). Bending-related faulting and mantle serpentinization at the Middle America trench. *Nature*, 425(6956), 367–373. https://doi.org/10.1038/nature01961

Reiners, P. W., Carlson, R. W., Renne, P. R., Cooper, K. M., Granger, D. E., McLean, N. M., & Schoene, B. (2018). *Geochronology and thermochronology*. John Wiley & Sons.

Restrepo, M., Bustamante, C., Cardona, A., Beltrán-Triviño, A., Bustamante, A., Chavarría, L., & Valencia, V. A. (2021). Tectonic implications of the jurassic magmatism and the metamorphic record at the southern Colombian Andes. *Journal of South American Earth Sciences*, 111, 103439. https://doi.org/10.1016/j.jsames.2021.103439

Ridolfi, F. (2021). Amp-TB2: An updated model for calcic amphibole thermobarometry. Minerals (Basel, Switzerland), 11(3), 324. https://doi.org/10.3390/min11030324

Ridolfi, F., Renzulli, A., & Puerini, M. (2010). Stability and chemical equilibrium of amphibole in calc-alkaline magmas: an overview, new thermobarometric formulations and application to subduction-related volcanoes. *Contributions to Mineralogy and Petrology*, 160(1), 45–66. https://doi.org/10.1007/s00410-009-0465-7

Rodríguez, G., & Zapata, G. (2006). Los conglomerados de tatamá, una nueva unidad paleógena de la zona central de la cordillera occidental de colombia. *Boletín de Ciencias de la Tierra*, (19), 43-55.

Rodríguez, G., Correa–Martínez, A.M., Zapata–Villada, J.P. & Obando–Erazo, G. (2019). Fragments of a Permian arc on the western margin of the Neoproterozoic basement of Colombia. In: Gómez, J. & Mateus–Zabala, D. (editors), The Geology of Colombia, Volume 1 Proterozoic – Paleozoic. Servicio Geológico Colombiano, *Publicaciones Geológicas Especiales*. 205–239. https://doi.org/10.32685/pub.esp.35.2019.10

Rudnick, R. L., & Gao, S. (2003). Composition of the continental crust. In *Treatise on Geochemistry*. Elsevier, 1-64

Ruprecht, P., Bergantz, G. W., Cooper, K. M., & Hildreth, W. (2012). The crustal magma storage system of Volcán Quizapu, Chile, and the effects of magma mixing on magma diversity. *Journal of Petrology*, 53(4), 801-840.

Rollinson, H., & Pease, V. (2021). *Using Geochemical Data: To understand geological processes*. Cambridge University Press.

Scarrow, J. H., Schmitt, A. K., Barclay, J., Horstwood, M. S. A., Bloore, A. J., & Christopher, T. E. (2021). Zircon as a tracer of plumbing processes in an active magmatic system: insights from mingled magmas of the 2010 dome collapse, Montserrat, Lesser Antilles Arc, Caribbean. *Journal of Volcanology and Geothermal Research*, 420(107390), 107390. https://doi.org/10.1016/j.jvolgeores.2021.107390

Schaltegger, U., Schmitt, A. K., & Horstwood, M. S. A. (2015). U–Th–Pb zircon geochronology by ID-TIMS, SIMS, and laser ablation ICP-MS: Recipes, interpretations, and opportunities. *Chemical Geology*, 402, 89–110. https://doi.org/10.1016/j.chemgeo.2015.02.028

Schiller, D., & Finger, F. (2019). Application of Ti-in-zircon thermometry to granite studies: problems and possible solutions. *Contributions to Mineralogy and Petrology*, 174(6), 1–16. https://doi.org/10.1007/s00410-019-1585-3

Schoene, B., Crowley, J. L., Condon, D. J., Schmitz, M. D., & Bowring, S. A. (2006). Reassessing the uranium decay constants for geochronology using ID-TIMS U–Pb data. *Geochimica et Cosmochimica Acta*, 70(2), 426–445. https://doi.org/10.1016/j.gca.2005.09.007

Sisson, T. W., & Grove, T. L. (1993). Experimental investigations of the role of H2O in calc-alkaline differentiation and subduction zone magmatism. *Contributions to Mineralogy and Petrology*, 113(2), 143–166. https://doi.org/10.1007/bf00283225

Shand, S.J. (1943) *Eruptive Rocks*. 2nd Edition, John Wiley, New York.

Sisson, T. W., Ratajeski, K., Hankins, W. B., & Glazner, A. F. (2005). Voluminous granitic magmas from common basaltic sources. *Contributions to Mineralogy and Petrology*, 148(6), 635–661. https://doi.org/10.1007/s00410-004-0632-9

Sláma, J., Košler, J., Condon, D. J., Crowley, J. L., Gerdes, A., Hanchar, J. M., Horstwood, M. S. A., Morris, G. A., Nasdala, L., Norberg, N., Schaltegger, U., Schoene, B., Tubrett, M. N., & Whitehouse, M. J. (2008). Plešovice zircon — A new natural reference material for U–Pb and Hf isotopic microanalysis. *Chemical Geology*, 249(1–2), 1–35. https://doi.org/10.1016/j.chemgeo.2007.11.005

Somoza, R., & Ghidella, M. E. (2005). Convergencia en el margen occidental de América del Sur durante el Cenozoico: subducción de las placas de Nazca, Farallón y Aluk. *Revista de la Asociación Geológica Argentina*, 60(4), 797-809.

Spikings, R., Cochrane, R., Villagomez, D., Van der Lelij, R., Vallejo, C., Winkler, W., & Beate, B. (2015). The geological history of northwestern South America: from Pangaea to the early collision of the Caribbean Large Igneous Province (290–75Ma). *Gondwana Research: International Geoscience Journal*, 27(1), 95–139. https://doi.org/10.1016/j.gr.2014.06.004

Stern, C. R. (2020). The role of subduction erosion in the generation of Andean and other convergent plate boundary arc magmas, the continental crust and mantle. *Gondwana Research: International Geoscience Journal*, 88, 220–249. https://doi.org/10.1016/j.gr.2020.08.006

Stern, C. R. (2011). Subduction erosion: Rates, mechanisms, and its role in arc magmatism and the evolution of the continental crust and mantle. *Gondwana Research: International Geoscience Journal*, 20(2–3), 284–308. https://doi.org/10.1016/j.gr.2011.03.006

Stern, R. J. (2002). Subduction zones. *Reviews of Geophysics* (Washington, D.C.: 1985), 40(4). https://doi.org/10.1029/2001rg000108

Streckeisen, A. (1974). Classification and nomenclature of plutonic rocks recommendations of the IUGS subcommission on the systematics of Igneous Rocks. *Geologische Rundschau: Zeitschrift Für Allgemeine Geologie*, 63(2), 773–786. https://doi.org/10.1007/bf01820841

Sun, P., Wang, Q., Hao, L.-L., Dan, W., Ou, Q., Jiang, Z.-Q., & Tang, G.-J. (2021). A mélange contribution to arc magmas recorded by Nd–Hf isotopic decoupling: An example from the southern Qiangtang Block, central Tibet. *Journal of Asian Earth Sciences*, 221(104931), 104931. https://doi.org/10.1016/j.jseaes.2021.104931

Tang, M., Ji, W.-Q., Chu, X., Wu, A., & Chen, C. (2020). Reconstructing crustal thickness evolution from europium anomalies in detrital zircons. *Geology,* 49(1), 76–80. https://doi.org/10.1130/g47745.1

Tischendorf, G., Rieder, M., Förster, H.-J., Gottesmann, B., & Guidotti, C. V. (2004). A new graphical presentation and subdivision of potassium micas. *Mineralogical Magazine*, 68(4), 649–667. https://doi.org/10.1180/0026461046840210

Tistl, M., Burgath, K. P., Höhndorf, A., Kreuzer, H., Muñoz, R., & Salinas, R. (1994). Origin and emplacement of Tertiary ultramafic complexes in northwest Colombia: Evidence from geochemistry and K-Ar, Sm-Nd and Rb-Sr isotopes. *Earth and Planetary Science Letters*, 126(1–3), 41–59. https://doi.org/10.1016/0012-821x(94)90241-0

Toro Toro, L. M., Borrero-Peña, C. A., & Ayala Carmona, L. F. (2010). Petrografía y geoquímica de las rocas ancestrales del volcán Nevado del Ruiz. *Boletín de Geología*, 32(1), 95-105.

Trenkamp, R., Kellogg, J. N., Freymueller, J. T., & Mora, H. P. (2002). Wide plate margin deformation, southern Central America and northwestern South America, CASA GPS observations. *Journal of South American Earth Sciences*, 15(2), 157–171. https://doi.org/10.1016/s0895-9811(02)00018-4

Turekian, K. K., & Holland, H. D. (2013). *Treatise on geochemistry*. Newnes.

Turner, S. J., & Langmuir, C. H. (2022). Sediment and ocean crust both melt at subduction zones. *Earth and Planetary Science Letters*, 584(117424), 117424. https://doi.org/10.1016/j.epsl.2022.117424

Ulmer, P., & Trommsdorff, V. (1995). Serpentine stability to mantle depths and subduction-related magmatism. *Science* (New York), 268(5212), 858–861. https://doi.org/10.1126/science.268.5212.858

Verdugo, G. & Aspdend, J. A. (1984). Reseña explicativa del mapa geológico preliminar, Plancha 299, Jamundí - Escala 1:100.000. *Ingeominas,* 1-20.

Vermeesch, P. (2018). IsoplotR: A free and open toolbox for geochronology. *Geoscience Frontiers*, 9 (5), 1479–1493. https://doi.org/10.1016/j.gsf.2018.04.001

Vernon, R. H. (2018). *A practical guide to rock microstructure*. Cambridge university press.

Vervoort, J. D., Plank, T., & Prytulak, J. (2011). The Hf–Nd isotopic composition of marine sediments. *Geochimica et Cosmochimica Acta*, 75(20), 5903–5926. https://doi.org/10.1016/j.gca.2011.07.046

Villagómez, D., & Spikings, R. (2013). Thermochronology and tectonics of the Central and Western Cordilleras of Colombia: Early Cretaceous–Tertiary evolution of the Northern Andes. *Lithos,* (160–161), 228–249. https://doi.org/10.1016/j.lithos.2012.12.008

Vinasco, C. J., Cordani, U. G., González, H., Weber, M., & Pelaez, C. (2006). Geochronological, isotopic, and geochemical data from Permo-Triassic granitic gneisses and granitoids of the Colombian Central Andes. *Journal of South American Earth Sciences*, 21(4), 355–371. https://doi.org/10.1016/j.jsames.2006.07.007

Wagner, L. S., Jaramillo, J. S., Ramírez-Hoyos, L. F., Monsalve, G., Cardona, A., & Becker, T. W. (2017). Transient slab flattening beneath Colombia. *Geophysical Research Letters*, 44(13), 6616–6623. https://doi.org/10.1002/2017gl073981

Wang, X., Hou, T., Wang, M., Zhang, C., Zhang, Z., Pan, R., Marxer, F., & Zhang, H. (2021a). A new clinopyroxene thermobarometer for mafic to intermediate magmatic systems. *European Journal of Mineralogy*, 33(5), 621–637. https://doi.org/10.5194/ejm-33-621-2021

Wang, Z., Zheng, X., Meng, G., Tang, H., & Fang, T. (2021b). Petrology, geochemical characteristics, tectonic setting, and implications for chromite and PGE mineralization of the Hongshishan Alaskan-type complex in the Beishan orogenic collage, north west China. *Frontiers in earth science*, 9. https://doi.org/10.3389/feart.2021.663760

Wegner, W., Worner, G., Harmon, R. S., & Jicha, B. R. (2011). Magmatic history and evolution of the Central American Land Bridge in Panama since Cretaceous times. *Geological Society of America Bulletin*, 123(3–4), 703–724. https://doi.org/10.1130/b30109.1

Weber, M., Gómez-Tapias, J., Cardona, A., Duarte, E., Pardo-Trujillo, A., & Valencia, V. A. (2015). Geochemistry of the Santa Fé Batholith and Buriticá Tonalite in NW Colombia – Evidence of subduction initiation beneath the Colombian Caribbean Plateau. *Journal of South American Earth Sciences*, 62, 257–274. https://doi.org/10.1016/j.jsames.2015.04.002

Weinberg, R. F., Vernon, R. H., & Schmeling, H. (2021). Processes in mushes and their role in the differentiation of granitic rocks. *Earth-Science Reviews*, 220(103665), 103665. https://doi.org/10.1016/j.earscirev.2021.103665

Whalen, J. B., & Hildebrand, R. S. (2019). Trace element discrimination of arc, slab failure, and A-type granitic rocks. *Lithos*, 348–349(105179), 1-19. https://doi.org/10.1016/j.lithos.2019.105179

Whattam, S. A., & Stern, R. J. (2016). Arc magmatic evolution and the construction of continental crust at the Central American Volcanic Arc system. *International Geology Review,* 58(6), 653–686. https://doi.org/10.1080/00206814.2015.1103668

White, W. M., & Klein, E. M. (2014). Composition of the oceanic crust. In *Treatise on Geochemistry* (pp. 457–496). Elsevier

Whitney, D. L., & Evans, B. W. (2010). Abbreviations for names of rock-forming minerals. *The American Mineralogist*, 95(1), 185–187. https://doi.org/10.2138/am.2010.3371

Wieser, P. E., Kent, A. J. R., Till, C. B., Donovan, J., Neave, D. A., Blatter, D. L., & Krawczynski, M. J. (2023). Barometers behaving badly I: Assessing the influence of analytical and experimental uncertainty on clinopyroxene thermobarometry calculations at crustal conditions. *Journal of Petrology*, 64(2). https://doi.org/10.1093/petrology/egac126

Williams, I.S., 1998. U-Th-Pb geocronology by ion microprobe. In: McKibben, M.A., Shanks III, W.C., Ridley, W.I. (Eds.), Applications of Microanalytical Techniques to Understanding Mineralizing Processes. *Reviews in Economic Geology.* (7), 1–3

Yakymchuk, C., Holder, R. M., Kendrick, J., & Moyen, J.-F. (2023). Europium anomalies in zircon: A signal of crustal depth? *Earth and Planetary Science Letters*, 622(118405), 1–11. https://doi.org/10.1016/j.epsl.2023.118405

Zapata, S., Cardona, A., Jaramillo, J. S., Patiño, A., Valencia, V., León, S., Mejía, D., Pardo-Trujillo, A., & Castañeda, J. P. (2019). Cretaceous extensional and compressional tectonics in the Northwestern Andes, prior to the collision with the Caribbean oceanic plateau. *Gondwana Research: International Geoscience Journal*, 66, 207–226. https://doi.org/10.1016/j.gr.2018.10.008

Zapata, G. (2001). Geología y geoquímica de la plancha 204 Pueblo Rico, Memoria explicativa*. Ingeominas*, 1-68.

Zhang, Y., Gazel, E., Gaetani, G. A., & Klein, F. (2021). Serpentinite-derived slab fluids control the oxidation state of the subarc mantle. *Science Advances*, 7(48). https://doi.org/10.1126/sciadv.abj2515

Zheng, Y.-F. (2019). Subduction zone geochemistry. *Geoscience Frontiers,* 10(4), 1223–1254. https://doi.org/10.1016/j.gsf.2019.02.003

Zheng, Y.-F., Xia, Q.-X., Chen, R.-X., & Gao, X.-Y. (2011). Partial melting, fluid supercriticality and element mobility in ultrahigh-pressure metamorphic rocks during continental collision. *Earth-Science Reviews*, 107(3–4), 342–374. https://doi.org/10.1016/j.earscirev.2011.04.004